ORTA DOĞU TEKNİK ÜNİVERSİTESİ
FEN BİLİMLERİ ENSTİTÜSÜ MÜDÜRLÜĞÜ

TEZ ŞABLONU ONAY FORMU
THESIS TEMPLATE CONFIRMATION FORM

1. Şablonda verilen yerleşim ve boşluklar değiştirilmemelidir.
2. **Jüri tarihi** Başlık Sayfası, İmza Sayfası, Abstract ve Öz'de ilgili yerlere yazılmalıdır.
3. İmza sayfasında jüri üyelerinin unvanları doğru olarak yazılmalıdır. Tüm imzalar **mavi pilot kalemle** atılmalıdır.
4. **Disiplinlerarası** programlarda görevlendirilen öğretim üyeleri için jüri üyeleri kısmında tam zamanlı olarak çalıştıkları anabilim dalı başkanlığının ismi yazılmalıdır. Örneğin: bir öğretim üyesi Biyoteknoloji programında görev yapıyor ve biyoloji bölümünde tam zamanlı çalışıyorsa, İmza sayfasına biyoloji bölümü yazılmalıdır. İstisnai olarak, disiplinler arası program başkanı ve tez danışmanı için disiplinlerarası program adı yazılmalıdır.
5. Tezin **son sayfasının sayfa** numarası Abstract ve Öz'de ilgili yerlere yazılmalıdır.
6. Bütün chapterlar, referanslar, ekler ve CV sağ sayfada başlamalıdır. Bunun için **kesmeler** kullanılmıştır. **Kesmelerin kayması** fazladan boş sayfaların oluşmasına sebep olabilir. Bu gibi durumlarda paragraf (¶) işaretine tıklayarak kesmeleri görünür hale getirin ve yerlerini **kontrol edin**.
7. Figürler ve tablolar kenar boşluklarına taşmamalıdır.
8. Şablonda yorum olarak eklenen uyarılar dikkatle okunmalı ve uygulanmalıdır.
9. Tez yazdırılmadan önce PDF olarak kaydedilmelidir. Şablonda yorum olarak eklenen uyarılar PDF dokümanında yer almamalıdır.
10. **Bu form aracılığıyla oluşturulan PDF dosyası arkalı-önlü baskı alınarak tek bir spiralli cilt haline getirilmelidir.**
11. Spiralli hale getirilen tez taslağınızdaki ilgili alanları imzalandıktan sonra, Tez Juri Atama Formu ile birlikte bölüm sekreterliğine teslim edilmelidir.
12. Tez taslaklarının kontrol işlemleri tamamlandığında, bu durum öğrencilere METU uzantılı öğrenci e-posta adresleri aracılığıyla duyurulacaktır.
13. Tez yazım süreci ile ilgili herhangi bir sıkıntı yaşarsanız, **Sıkça Sorulan Sorular (SSS)** sayfamızı ziyaret ederek yaşadığınız sıkıntıyla ilgili bir çözüm bulabilirsiniz.

1. Do not change the spacing and placement in the template.
2. Write **defense date** to the related places given on Title page, Approval page, Abstract and Öz.
3. Write the titles of the examining committee members correctly on Approval Page. **Blue ink** must be used for all signatures.
4. For faculty members working in **interdisciplinary programs**, the name of the department that they work full-time should be written on the Approval page. For example, if a faculty member staffs in the biotechnology program and works full-time in the biology department, the department of biology should be written on the approval page. Exceptionally, for the interdisciplinary program chair and your thesis supervisor, the interdisciplinary program name should be written.
5. Write **the page number of the last page** in the related places given on Abstract and Öz pages.
6. All chapters, references, appendices and CV must be started on the right page. **Section Breaks** were used for this. **Change in the placement** of section breaks can result in extra blank pages. In such cases, make the section breaks visible by clicking paragraph (¶) mark and **check their position.**
7. All figures and tables must be given inside the page. Nothing must appear in the margins.
8. All the warnings given on the comments section through the thesis template must be read and applied.
9. Save your thesis as pdf and Disable all the comments before taking the printout.
10. **Print two-sided the PDF file that you have created through this form and make a single spiral bound.**
11. Once you have signed the relevant fields in your thesis draft that you spiraled, submit it to the department secretary together with your Thesis Jury Assignment Form.
12. This will be announced to the students via their METU students e-mail addresses when the control of the thesis drafts has been completed.
13. If you have any problems with the thesis writing process, you may visit our **Frequently Asked Questions (FAQ)** page and find a solution to your problem.

☒ **Yukarıda bulunan tüm maddeleri okudum, anladım ve kabul ediyorum. / I have read, understand and accept all of the items above.**

Name : **Ali**
Surname : **Bagheri Behboud**
E-Mail : **ali.behboud@metu.edu.tr**
Date :
Signature : _____

DEVELOPMENT OF NANOSTRUCTURED METALLIC GLASSES WITH HIGH TOUGHNESS

A THESIS SUBMITTED TO
THE GRADUATE SCHOOL OF NATURAL AND APPLIED SCIENCES
OF
MIDDLE EAST TECHNICAL UNIVERSITY

BY

ALI BAGHERI BEHBOUD

IN PARTIAL FULFILLMENT OF THE REQUIREMENTS
FOR
THE DEGREE OF MASTER OF SCIENCE
IN
MECHANICAL ENGINEERING

AUGUST 2021

Approval of the thesis:

DEVELOPMENT OF NANOSTRUCTURED METALLIC GLASSES WITH HIGH TOUGHNESS

submitted by **ALI BAGHERI BEHBOUD** in partial fulfillment of the requirements for the degree of **Master of Science** i**n Mechanical Engineering, Middle East Technical University** by,

Prof. Dr. Halil Kalıpçılar
Dean, Graduate School of **Natural and Applied Sciences** _____

Prof. Dr. M. A. Sahir Arıkan
Head of the Department, **Mechanical Engineering, METU** _____

Assoc. Prof. Dr. Sezer Özerinç
Supervisor, **Mechanical Engineering, METU** _____

Examining Committee Members:

Prof. Dr. Yunus Eren Kalay
Metallurgical and Materials Eng., METU _____

Assoc. Prof. Dr. Sezer Özerinç
Mechanical Eng., METU _____

Assoc. Prof. Dr. Ender Yıldırım
Mechanical Eng., METU _____

Asst. Prof. Dr. Eda Aydoğan
Metallurgical and Materials Eng., METU _____

Prof. Dr. Oğuzhan Yılmaz
Mechanical Eng., Gazi University _____

Date: 19.08.2021

I hereby declare that all information in this document has been obtained and presented in accordance with academic rules and ethical conduct. I also declare that, as required by these rules and conduct, I have fully cited and referenced all material and results that are not original to this work.

Name Last name: Ali Bagheri Behboud

Signature:

ABSTRACT

DEVELOPMENT OF NANOSTRUCTURED METALLIC GLASSES WITH HIGH TOUGHNESS

Bagheri Behboud, Ali
Master of Science, Mechanical Engineering
Supervisor: Assoc. Prof. Dr. Sezer Özerinç

August 2021, 102 pages

Metallic glasses are metallic alloys with disordered atomic structures and desirable mechanical properties such as high hardness, high elastic limits, and wear resistance. These properties make metallic glasses promising materials for wear-resistant, corrosion-resistant, and biocompatible coating applications. On the other hand, metallic glasses are brittle, which is a major disadvantage for their use in practice. This thesis study aimed to tackle this problem through the development of nanostructured metallic glasses with high toughness and ductility. In the first part, the thesis considered synthesizing a binary thin film metallic glass over a wide compositional range. Two binary systems, namely, ZrTa and CuTa were investigated. Physical vapor deposition method was the approach for producing the thin films samples, and a combinatorial sputtering technique was employed during the deposition process. This way, 25 monolithic samples (13 ZrTa and 12 CuTa samples) were produced in only two sputtering sessions. The microstructures of the alloy systems were then investigated, demonstrating a wide compositional range of amorphous structures in both systems. Combining these with micromechanical testing provided the underlying structure-property relationships. The next step was the exploration of a novel approach for overcoming the brittle nature of metallic glasses through engineered heterogeneities in the form of compositional

modulations. A recently developed indentation-based energy method was used to determine the fracture toughness of nanolayered ZrTa samples, and the results demonstrated that the nanolayered metallic glass composites combine high hardness with ductility, rendering this approach promising for the development of commercial coatings for engineering applications.

The same route was also explored CuTa system. In this case, a more sophisticated technique was used to measure the ductility through direct tensile testing. The results showed that the nanolayered metallic glass and MG-crystalline composites combine high hardness, elastic modulus, and ductility, demonstrating their great potential to develop high performance composite coatings.

Keywords: metallic glasses, thin films, fracture toughness, mechanical properties, nanostructured materials

ÖZ

YÜKSEK TOKLUĞA SAHİP NANOYAPILI METALİK CAM ALAŞIMLARIN GELİŞTİRİLMESİ

Bagheri Behboud, Ali
Yüksek Lisans, Makina Mühendisliği
Tez Yöneticisi: Assoc. Prof. Dr. Sezer Özerinç

Ağustos 2021, 102 sayfa

Metalik camlar, düzensiz atomik yapılara ve yüksek sertlik, mukavemet ve aşınma direnci gibi üstün mekanik özelliklere sahip metalik alaşımlardır. Bu özellikler metalik camları aşınma önleyici, korozyona dayanıklı ve biyouyumlu kaplama uygulamaları için umut verici kılmaktadır. Öte yandan, metalik camlar kırılgandır ve bu da uygulamalar için büyük bir dezavantaj oluşturmaktadır. Bu tez çalışması, yüksek tokluk ve sünekliğe sahip nanoyapılı metalik camların geliştirilmesi yoluyla bu problemin üstesinden gelmeyi amaçlamaktadır. Tezin ilk bölümü, geniş bir kompozisyon aralığında ikili sistemlerde ince film metalik camların sentezlenmesini ele almaktadır. Bu kapsamda ZrTa ve CuTa ikili sistemleri incelenmiştir. Numuneleri üretmek için fiziksel buhar biriktirme yöntemi kullanılmış ve kombinatoryal saçtırma yaklaşımı benimsenmiştir. Bu sayede, sadece iki saçtırma seansında 25 monolitik numune (13 ZrTa ve 12 CuTa numunesi) üretilmiştir. Ardında tüm numunelerin içyapısı incelenmiş ve her iki sistemde de geniş bir kompozisyon aralığı için amorf yapı gözlenmiştir. Gerçekleştirilen mikromekanik ölçümler sayesinde ilgili yapı-özellik ilişkileri kurulmuştur.

Bir sonraki adım olarak, kompozisyon modülasyonları aracılığıyla nanoheterojenliklere sahip nanokatmanlı metalik camlar üretilmiştir. Bu kapsamdaki ZrTa numunelerinin kırılma tokluğunu ölçmek için yakın zamanda geliştirilen

nanosertlik temelli bir enerji yöntemi kullanılmıştır. Sonuçlar, söz konusu nanokatmanlı metalik cam kompozitlerin yüksek sertlik ve yüksek sünekliği beraber sunduğunu göstermiş ve bu yaklaşımın mühendislik uygulamaları için ticari kaplamaların geliştirilmesine yönelik potansiyel taşıdığını ortaya koymuştur. ZrTa çalışmasında olduğu gibi, CuTa çalışmasında da kompozisyona bağlı modülasyonlar şeklinde tasarlanmış heterojen bir yapı incelenmiştir. Bu kez kaplamalara doğrudan çekme testi uygulanmış ve nanokatmanlı metalik cam ve metalik cam-kristal kompozitlerin yüksek sertlik, elastikiyet modülü ve sünekliği bir araya getirdiği ortaya konmuştur. Elde edilen sonuçlar, nanokatmanlı metalik cam kaplamaların mühendislik uygulamaları için büyük gelecek vaat ettiğini göstermektedir.

Anahtar Kelimeler: metalik camlar, ince filmler, kırılma tokluğu, mekanik özellikler, nanoyapılı malzemeler

Dedicated to My Mother, My Father, My Brothers and My Girlfriend

ACKNOWLEDGMENTS

Firstly, I would like to express my gratitude to my supervisor, Assoc. Prof. Dr. Sezer Özerinç for his patient guidance, enthusiastic encouragement and useful critiques of this research work. It has been an honor to be his student.

I am grateful to Servet Şehirli for sharing his experiences, thoughts, and dedication. I would like to thank Amir Fadaei, Burçin Kaygusuz, Mehmet Kepenekçi, Roozbeh Neshani and Mohammad Abboud firstly for their friendship and secondly for their helpful discussions on the experiments and data analyses.

I would like to thank Dr. Amir Motallebzadeh for helping me do some of the experiments. I am also grateful to METU Central Laboratory and Bilkent UNAM staff for their technical help.

Finally, I would like to thank my family and my girlfriend. I am grateful to them for providing me the confidence needed for becoming successful and for motivating me on the challenging paths every time I struggled.

This thesis work has been supported by TÜBİTAK 1002 Project #218M219 and ODTÜ BAP Projects # GAP-302-2020-10221 and BAP-08-11-2016-072.

TABLE OF CONTENTS

LIST OF TABLES

LIST OF FIGURES

LIST OF ABBREVIATIONS

BCC	body centered cubic
C	crystalline
DC	Direct Current
EDS	energy-dispersive x-ray spectroscopy
FCC	face centered cubic
FIB	focused ion beam
FWHM	full width half maximum
HCP	hexagonally close packed
MG	metallic glasses
PVD	physical vapor deposition
RF	Radio Frequency
SEM	scanning electron microscopy
STZ	shear transformation zones
TEM	transmission electron microscopy
XRD	X-ray diffraction

LIST OF SYMBOLS

H	hardness
P	load
P_{max}	Peak indentation load
S	stiffness of the initial part of the unloading
h_f	final depth after unloading
hmax	maximum hardness
h_c	contact depth
A_p	projected area
ϵ	Sneddon's equation constant
θ	angle of incidence
n	diffraction order
hkl	crystalline plane
d	interatomic distance
λ	wavelength of the incident x-ray beam
K	dimensionless value representing the shape factor
B	full width of the associated diffraction peak at half maximum
L	crystallite size
E	elastic modulus

CHAPTER 1

INTRODUCTION

1.1 Overview

Metallic glasses (MGs) are alloys that exhibit an amorphous atomic structure. MGs' unique atomic configuration free of crystalline order and grain boundaries provide a wide range of desirable properties, including high hardness, large elastic limits, wear resistance, corrosion resistance, and biocompatibility [1–4].

Concentrated alloys of a wide range of metallic element combinations can exhibit an amorphous structure [5]. Therefore, there exists a huge design space for the development of amorphous alloys tuned for high strength, wear resistance, and high toughness.

Thin film metallic glasses (TFMGs) are a special class of MGs usually obtained by physical vapor deposition [6]. The ultra-high cooling rates offered by this approach further extend the range of glass-forming compositions and make TFMGs a promising class of materials for wear-resistant, corrosion-resistant, and biocompatible coatings [7]. TFMGs also offer advantages for the MEMS industry due to their defect-free nature, isotropic properties, high elastic limits, and processability at the nanoscale [8].

A fundamental approach to the exploration of the MG design space has been the investigation of binary metallic glasses. While binary systems are difficult to amorphized using conventional rapid cooling schemes, magnetron sputtering-based physical vapor deposition eliminates this limitation and allows a simpler and systematic exploration of the design space of binary alloys.

In this thesis, we explore the structure-property relationships of the Zr-Ta and Cu-Ta systems in detail. The methodology and the design of experiments have been formulated to cover some key aspects of the current understanding of the mechanical behavior of metallic glasses, as summarized below.

One of the major drawbacks of MGs is their brittle nature. Considered to be a primarily intrinsic feature of MGs, the brittleness is mainly due to the shear transformation zones [9] causing shear banding behavior. Earlier efforts towards addressing this problem have focused on the development of amorphous-crystalline composites [10]. In this approach, the distribution of a crystalline phase forces the amorphous matrix to accommodate further plasticity through the generation of additional shear bands. The compositional range investigated in this thesis for ZrTa and CuTa includes microstructures with such amorphous-crystalline domains, whose effect on ductility will be explored through tensile test and nanoindentation-based toughness measurements. Moreover, we developed amorphous-crystalline nanolayerd CuTa composites to investigate the impact of introducing the semi-crystalline phase on ductility enhancement of them based on tensile test-based toughness measurements and quantifying the ductility of the samples.

While the development of amorphous-crystalline composites has been proven successful, these semi-crystalline structures tend to at least partially sacrifice some unique advantages of fully amorphous alloys such as excellent formability, corrosion resistance, and ultra-high hardness [11,12]. Furthermore, the microstructure in these composites is vulnerable to significant structural changes upon alloying or deformation, making their use in applications challenging. Therefore, there have been continuing efforts to achieve ductility in metallic glasses while maintaining a fully amorphous structure. Recent advances in this route were made possible through the development of metallic glasses with nanoscale heterogeneities [13,14]. These heterogeneities, based on nanoscale phase separations and thermodynamically driven modulations in the medium-range order, result in perturbations in the local mechanical properties and act as strong barriers to catastrophic propagation of shear bands. Most studies in this field so far have focused on nanoheterogeneities naturally

occurring in metallic glass systems based on the thermodynamic landscape that favors phase separation. However, there has been no study to date to our knowledge that attempted at directly engineering the amplitude and periodicity of such modulations in a controlled fashion. As part of this study, we investigate this novel route of producing layered ZrTa and CuTa thin film metallic glasses with precisely controlled properties modulations.

Magnetron sputtering has been the primary method for the production of metallic glasses in thin film form, due to the accurate control of process parameters and compositions combined with the advantage of minimized contamination ensured by the high vacuum levels. The combinatorial magnetron sputtering, on the other hand, provides a further advantage of producing a continuous range of compositions in a single sputtering session and enables a precisely controlled experimental approach. Based on these advantages mentioned above, we employed combinatorial magnetron sputtering for the synthesis of the Zr-Ta and Cu-Ta films.

In this study, in the light of recent findings and methodological advances, we systematically investigate the microstructure and mechanical properties of ZrTa and CuTa alloys over a wide compositional range. In addition, we investigate a novel route of improving the mechanical response of MGs through composition modulations.

1.2 Metallic Glasses

1.2.1 General Features

Unlike crystalline materials, which possess ordered atomic structure, in amorphous materials, atoms are arranged in a random pattern, so they do not encounter the restriction and defects of crystalline materials like dislocations and grain boundaries [1–4,15]. These amorphous alloys depict a broad range of ideal characteristics, including remarkable strength, high elastic limit, corrosion resistance, and wear resistance [4]. Due to their random atomic arrangement and metastable form possess distinctive structural and mechanical characteristics [16]. The lack of dislocations and long-range order of atoms found in crystalline materials makes amorphous materials stronger and harder than their crystalline counterparts. Furthermore, the large design space provided by MGs, as well as the lack of grain boundaries, allow for the manufacture of wear-resistant, corrosion-resistant, and biocompatible coatings [15,17,18]. In other words, Amorphous metallic alloys combine the high strength of advanced metal alloys with the elasticity of polymers [3,4].

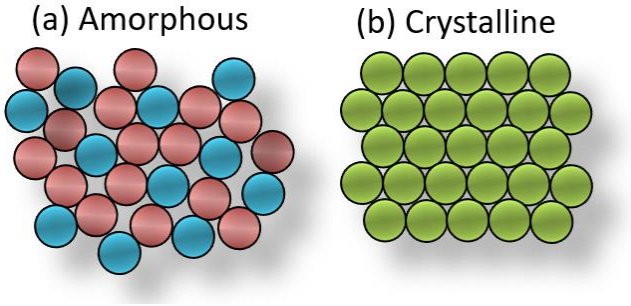

Figure 1. Schematic illustration of (a) amorphous material. (b) crystalline material.

BMGs frequently have higher yield strengths and elastic limits than their polycrystalline counterpart of identical composition. These characteristics, among others, imply that metallic glasses might be ideal structural materials. However, at room temperature, they have little plasticity before fracture happening [19]. While

their lack of ductility prevents them from being used as a structural material reasonably quickly, their high-temperature sensitivity implies that BMGs might be used in certain shape-forming processes [20].

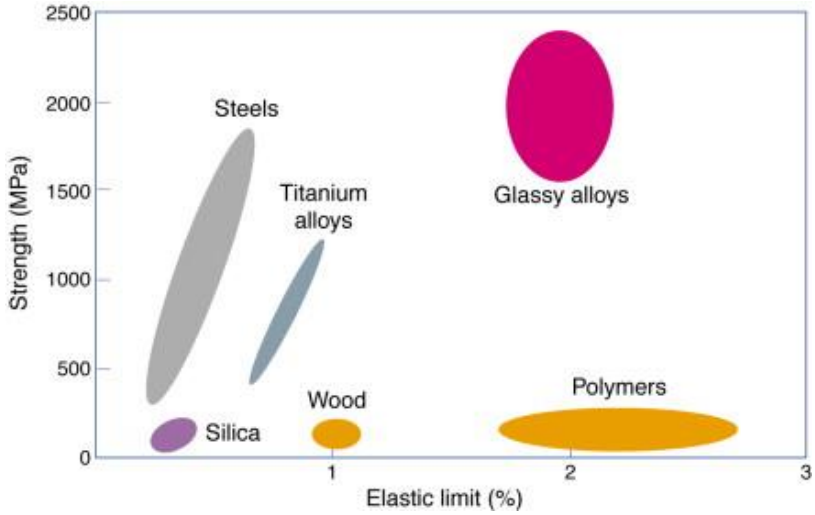

Figure 2. Amorphous metallic alloys combine the superior strength of crystalline metal alloys with the elasticity of polymers [21].

1.2.2 History and Applications

Amorphous metals were found by Klement et al. around a half-century ago, when they rapidly quenched a combination of gold and silicon to produce an amorphous alloy [22]. The melt was kinetically skipped the crystallization step due to low atomic mobility, resulting in the system solidifying into a meta-stable state with no long-range order. To put it simply, a high cooling rate was required to prevent crystallization. The fabrication was confined to foils, ribbons, and powders as a result. In 1990, metallic glasses which needed lower critical cooling rates to be produced were found, allowing the production of specimens with thicknesses greater than a few millimeters [23].

Later on, MGs were industrialized [24], and trying complicated alloying compositions enhanced the fabricability of metallic glasses, which facilitated bulk metallic glasses (BMGs) to be developed at slower cooling rates [25,26].

Bulk MGs offer several distinguishing characteristics, including excellent wear resistance, high strength-to-weight ratio, high hardness, elastic modulus, and high corrosion resistance [27–29]. Sports equipment, watches, electromagnetic casings, optical equipment, decorative products, choke coils, power inductors, magnetic field detection devices, electromagnetic wave shielding sheets, medical instruments, thin-film coatings, motor parts, and pressure sensors have all been made with bulk MGs [15].

Even though there is a huge amount of local plastic deformation at the shear bands in metallic glasses, the macro plastic deformation is still restricted [30]; therefore, the technical applications of MGs are similarly constrained.

Thin film metallic glasses as a category of MGs lately attracted interest from both a scientific and a practical perspective [6]. Thin-film MGs permit us to conduct fundamental research of structure-property relationships in MGs; their special characteristics also provide opportunities in terms of application. Thin film metallic glasses are promising candidates for the MEMS industry such as fabrication of micro-actuators due to their outstanding and unique structure and properties [6,8].

1.2.3 Mechanical Behavior

Metals and alloys are malleable, distinguishing them from other materials such as ceramics, semiconductors, and specific polymers. That is, they may be plastically deformed to get the desired shape. Furthermore, their ductility may be modulated, allowing the level of malleability to be defined according to the needs of the production process [31].

Every crystalline material contains defects. These defects influence the mechanical characteristics of metals. The point, linear, and planar crystal defects are the three

types of crystal defects in crystalline materials. Linear defects are known as dislocations. Planar defects are interfaces between homogenous regions of the material. Grain boundaries, stacking faults, and external surfaces are examples of planar defects.

Crystalline materials are composed of various grains of different sizes. Crystallinity defects like grain boundaries and dislocations are induced into the structure by these grains. Plastic deformation in material occurs due to the movement of dislocations. Plastic deformation develops when a sufficient load is applied to enable these dislocations to move. This load is typically much smaller than the load required to separate atomic planes by breaking interatomic bonding. When grains become small enough, grain boundaries become a vast majority of the material and govern the deformation mechanism. Because grain boundaries can slide easily, a smaller load is required to distort a material along its grain boundaries. Grain boundaries further to the material's drawbacks by facilitating chemical reactions like oxidation and corrosion. As a result, the mechanical properties of crystalline material are inextricably linked to its crystallographic structure. Dislocation theory is commonly regarded as a simple explanation of the correlation between crystal structure and crystalline material strength and ductility [32].

MGs are devoid of any homogenous plastic deformation in the absence of dislocation-mediated crystallographic slip [3,16]. Much study has been devoted to explaining MG deformation, which has recently been described as a sequence of six events [33]. The first event is STZs nucleation, which occurs when atoms attempt to organize themselves following the shear strain imposed. The second is the development and propagation of shear bands [34]. The third is adiabatic heating, which occurs in locally strained areas [35]. The fourth step is the formation of nanocrystallites inside or near emerging shear bands [36]. The fifth step is to create nanovoids in existing shear bands [3]. The sixth is merging the voids, which results in increasingly larger voids and, eventually, fractures [37].

Another model that could describe the deformation process of MGs is the free volume model, which defines inhomogeneous deformation in MGs as a result of biased stacking of free volumes at stressed regions [38]. The schematic illustration of STZ and free-volume models are depicted in Figure 3.

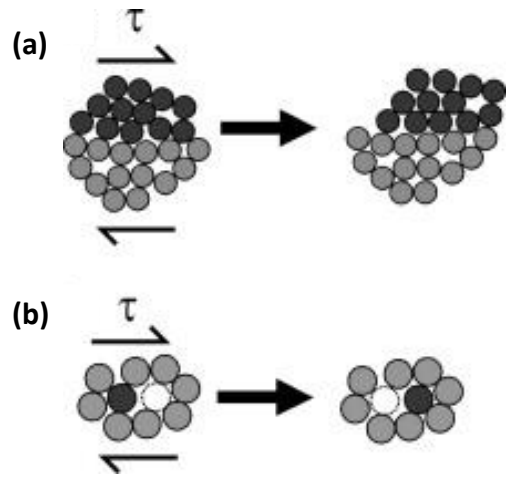

Figure 3. Schematic representation [16] of (a) STZ model when under an applied shear force, hundreds of atoms shear collectively [39] (b) an individual atomic jump in the free-volume model [38].

1.3 Metallic Glass-Crystalline Composites

One of the most significant disadvantages of MGs is their brittleness. Brittleness, which is thought to be a predominantly inherent characteristic of MGs, is principally caused by shear transformation zones [9] – the carriers of plasticity in metallic glasses, causing shear banding behavior. Shear bands, localized deformation paths with shear softening result in rapid and catastrophic failure, especially under tensile loading [27]. Earlier attempts to solve this issue centered on the fabrication of amorphous-crystalline composites [10].

To be more specific, two simple types of amorphous-crystalline composites fabrication. The first approach is the fabrication of nanolayered samples, which consist of alternative crystalline and amorphous layers. In this vein, remarkable

ductility can be obtained using metallic glass layers, which are brittle in the bulk form [40–42]. The existence of crystalline layers efficiently prevents the catastrophic growth of shear bands in amorphous layers. It inhibits brittle failure, mainly when the layer thickness is similar to the length scale required for shear localization [41]. The suitability of the flow strengths of the amorphous and crystalline layers has been demonstrated to enhance codeformation, which also increases nanocomposite ductility [40,43].

The second method of amorphous-crystalline composites fabrication can produce and develop monolithic samples while both the amorphous and crystalline phases are present in the structure of the material. Similarly, in this case, the distribution of a crystalline phase acts as a barrier to the spread of unstable shear bands [44], forcing the amorphous matrix to tolerate more plasticity by forming new shear bands.

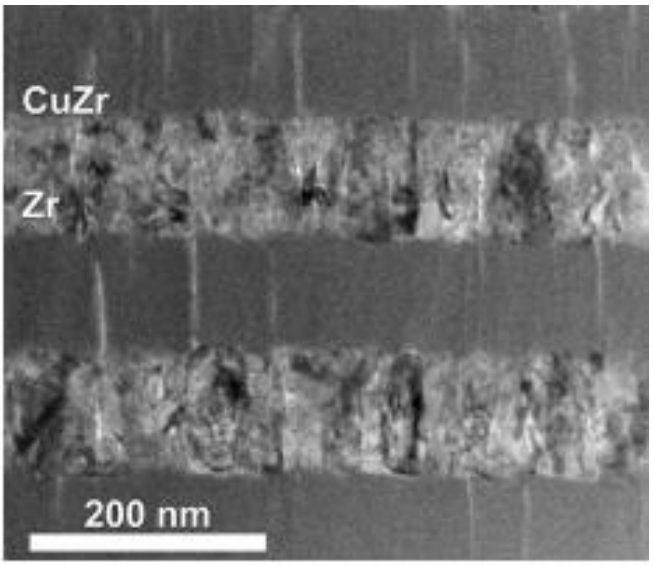

Figure 4. Cross-sectional bright-field TEM image of CuZr/Zr-100 nanolayers [45] as an example of crystalline-amorphous nanolayered composite.

1.4 Metallic Glasses with Nanoscale Heterogeneities

Although the fabrication of amorphous-crystalline composites has been effective and practical, these semi-crystalline structures appear to have lost some of the distinctive benefits of completely amorphous alloys, such as outstanding formability, corrosion resistance, and ultra-high hardness [11,12]. Moreover, the microstructures in these composites are susceptible to substantial structural changes when alloyed or deformed, making their usage in applications difficult. As a result, efforts to produce ductility in metallic glasses while preserving an utterly amorphous structure have been ongoing. This direction has made recent progress feasible by introducing metallic glasses with nanoscale heterogeneities [13,14]. Based on nanoscale phase separations and thermodynamically mediated modulations in the medium-range order, these heterogeneities cause perturbations in the regional mechanical properties and function as significant barriers to catastrophic shear band growth.

According to recent researches, intentionally increasing structural inhomogeneities in an amorphous alloy will facilitate distributed plastic flow. Developing the material's microstructure to prevent extreme strain localization and promoting plastic flow can help improve the ductility of amorphous alloys [13]. Also, recent work through MD simulations suggests that nanoscale heterogeneities in a glassy structure can prevent the localization of strain and prevent catastrophic shear banding [14].

The toughening is especially effective when the structure is composed of hard and soft phases, where the soft phase accommodates the majority of the plasticity and the hard phase act as barriers to shear bands. So far, most research in this area has concentrated on nanoheterogeneities that arise naturally in metallic glass systems due to the thermodynamic environment that encourages phase separation. To the best of our knowledge, no study has attempted to directly design the amplitude and frequency of such modulations in a controlled manner.

1.5 Nanolayered Composites

The mechanical characteristics of nanolayered metals have been extensively studied during the last two decades. These structures' outstanding strength [46], thermal stability [47], and radiation resistance [48] make them ideal engineering materials. Furthermore, metallic nanolayers offer a regulated and systematic method for investigating the mechanical behavior of materials and surfaces at the nanoscale [49]. Using physical vapor deposition to fabricate nanolayers, in particular, provides an opportunity for accurate adjustment of layer thicknesses and gives a sharp interface for studying interface-dominated plastic behavior [50]. Previous researches in this subject have concentrated on crystalline/crystalline nanolayers. C/C nanolayers often have significantly greater strength values than their components. The idea of nanolayered metals has recently been applied to amorphous/crystalline (A/C) nanolayers with a metallic glass as one of the component layers. Outstanding ductility may be obtained by employing metallic glass components brittle in bulk form in A/C nanolayers [40,41]. The presence of crystalline layers efficiently prevents catastrophic propagation of shear bands in amorphous layers and prevents brittle failure, particularly when the layer thickness is equivalent to the length scale required for shear localization [41]. All the over-mentioned nanolayered composites consist of crystalline layers, and they may not take advantage of the presence of amorphous alloy in the composite structure completely. These semi-crystalline (A/C) or fully crystalline (C/C) structures appear to not have or lose some of the advantages of completely amorphous alloys, such as outstanding formability, corrosion resistance, and ultra-high hardness [11,12]. In this regard, producing fully amorphous nanolayered composites while keeping their high hardness, and improving their ductility and toughness can be an influential work. As a result, efforts to produce ductility in metallic glasses while preserving a fully amorphous structure attracted attention. However, there has been no study to date on producing Amorphous/Amorphous nanolayers consist of alternating amorphous layers with different mechanical properties.

1.6 Thin Film Metallic Glasses

Thin film metallic glasses (TFMGs) are a subclass of MGs that are often manufactured by physical vapor deposition [6]. This approach's ultra-high cooling speeds broaden the range of glass-forming compositions even more.

1.6.1 Physical Vapor Deposition (PVD)

Physical vapor deposition (PVD) is a common method for preparing thin films [51]. The target material is evaporated into a vacuum chamber containing the substrate. This method may be used to develop nanostructured materials in the form of thin films.

Magnetron sputtering is the most widely utilized PVD method in research. This method employs magnetically accelerated inert gas ions (often Ar+) to knock off atoms of a target material, sputter them into a vacuum chamber, and finally force them to condense onto a substrate [52]. Ion bombardment of the target material's surface creates secondary electrons, resulting in a steady plasma in the chamber. The mechanism of magnetron sputtering is depicted in Figure 5. Two sputtering targets can be placed in the chamber at the same time, allowing the deposition of two distinct materials.

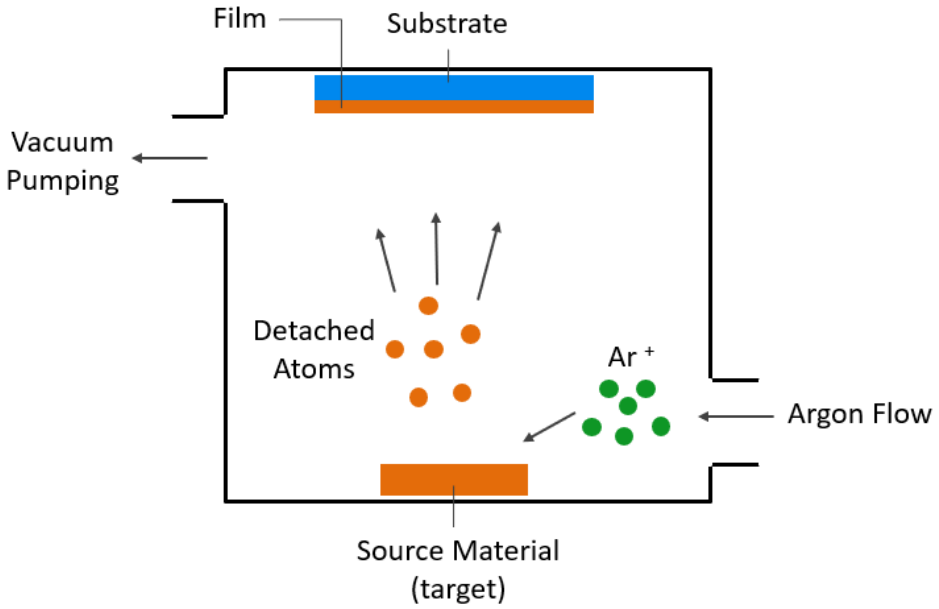

Figure 5. Schematic illustration of magnetron sputtering.

1.7 Mechanical and Micromechanical Characterization of Thin Films

Recent advancements in micromechanical testing have made it feasible to measure the mechanical characteristics of a nanomaterial. Hardness, elastic modulus, strength, adhesion, and wear resistance are all micromechanical characteristics that have been described in the literature [53–55]. Moreover, some novel techniques are discussed in the literature to facilitate the study of some of the mechanical properties of materials like fracture toughness for thin films [56,57]. The mechanical and micromechanical characterization techniques utilized in the thesis study are discussed in this section.

1.7.1 Nanoindentation

The nanoindentation test is the most widely used method for determining the hardness of materials at the nanoscale [53–55]. Nanoindentation makes use of a

diamond tip that is pushed into the surface of a material in order to penetrate and leave an impression [58]. The load-displacement curve of the test was created using a nanoindentation device equipped with force and displacement sensors.

In addition to hardness and elastic modulus, nanoindentation may be utilized to evaluate a material's yield strength [59]. Some disadvantages of nanoindentation have been described in the literature, including the substrate, pile-up, and sink-in effects [60].

1.7.2 Fracture Toughness Measurements

Toughness is a material's capacity to absorb energy during deformation up to fracture [61,62]. However, the capability of a material to resist the development of a present crack is referred to as fracture toughness. Toughness includes both the energy necessary to form the crack and the energy required to allow the crack to propagate until it fractures, whereas fracture toughness considers the energy meant to allow the crack to propagate until it fractures [63].

There are several methods to measure toughness and fracture toughness for thin films, such as bending, buckling, scratching, indentation, and tensile tests. We will discuss the indentation-based and tensile-based approaches below in detail [63].

1.7.2.1 Indentation-Based Fracture Toughness Measurements

Indentation is the most commonly used and helpful methodology for analyzing thin film coating toughness [63–65].

Indentation techniques for measuring toughness have been established for bulk brittle materials and suitably thick, brittle coatings [66,67]. The fracture morphology becomes increasingly sophisticated as the coating thickness decreases and complex composition and structure are introduced. This makes assessing fracture toughness

more challenging. Stress analysis and energy-based are two methods for determining fracture toughness in the indentation-based models [68].

1.7.2.1.1 Models Based on Radial Crack Propagation

In the indentation test of materials, several types of cracks depending on the load, material, environment conditions, and indenter can present [69]. In this vein, depending on the type of crack induced in the sample toughness of the material can be determined according to the stress-analysis-based model.

The fracture behavior of thin films is a complicated function of the mechanical properties of the film, the substrate, residual stresses, film thickness, and indentation depth [70–76]. When the indentation results in visible radial cracks, the size, and morphology of these cracks can be used to predict the fracture toughness [63].

1.7.2.1.2 Models Based on Energy Methods

With the development of complicated coating systems like multilayers and appearing different types of cracks during indentation, it needs to develop a method that can be useful to determine fracture toughness in different cases. Therefore, there are several energy-based models, and totally we can categorize them into two main methods. The first one is based on crack-induced pop-in in the load-displacement curve. In this model, the calculation of fracture toughness can be done in three different ways, and all of them are useful when there are excursions or pop-ins in the load-displacement curves of the sample.

The second approach is suitable for the cases that there is no excursion in the load-displacement curve. This method is a very suitable approach when we cannot use the stress-analysis-based model because of the absence of radial cracks, and the energy method based on crack-induced pop-in in the load-displacement curve is not applicable due to the absence of excursion in a load-displacement curve. This

approach consists of two distinct methods. One of these methods is based on the analysis of irreversible work in the load-displacement curve proposed by Chen et al. [68,76]. According to the energy-based approach in the case of uncracked materials under displacement control experiments, fracture plays an important role in transforming some accumulated elastic energy into irreversible energy [76]. In this method, the essential factor is to get the plastic work during nanoindentation.

1.7.2.2 Uniaxial Tensile-Based Fracture Toughness Measurements

One of the recently developed methods for exploring fracture behavior and measuring fracture toughness of the thin films is using the tensile test. Fabrication of freestanding thin films needs some restrictions, such as difficult and complicated sample preparation process. Moreover, performing a tensile test on freestanding thin films cannot be applicable for films with thickness lower than 3 μm [57]. To overcome such problems, deposition of thin films on polyimide substrates seems to be a suitable technique. Recent studies show that polyimide-supported metal thin films can deform up to large strains [77]. In this method, polyimide sheets should be cut into dogbone-shaped tensile specimens. After the deposition process, a uniaxial tensile test can be applied on coated polyimide samples.

This model is proposed based on the linear elastic response of the substrate and the coating [78]. Fracture toughness value is a function of elastic modulus, fracture stress, film thickness, and the Poisson ratio of the film in this method. Furthermore, the tensile test can provide some information about the ductility of the films based on fracture strain results.

CHAPTER 2

EXPERIMENTAL PROCEDURES AND METHODOLOGY

Aiming to investigate the microstructure and mechanical properties of metallic thin films fabricated in this study; several types of microstructural analysis and different types of mechanical and micro-mechanical tests are done on the samples. Before beginning property analysis of samples produced in this study, all of them were fabricated using the magnetron sputtering technique. Then the composition of the samples is investigated using EDS, and microstructural analyses are done using XRD and TEM. To investigate the mechanical properties of produced samples, nanoindentation and tensile tests are done them. As an important part of this study, two different energy methods are used to measure the fracture toughness of the samples. All the above-mentioned experiments and methods are explicitly described in this chapter.

2.1 Sample Preparation

In this work, a VAKSİS magnetron sputterer equipped with two guns (RF and DC) was used to coat all the films. Figure 6 shows the sputterer used in this thesis. Different sets of films have been prepared.

For the first part of this thesis, ZrTa thin film samples were prepared. We used the combinatorial technique to sputter these samples in a single step of the sputtering process. Secondly, we prepared nanolayered samples. Both sets of samples were sputtered on SiO_2 wafers. All the monolithic and nanolayered samples have a total thickness of 1 μm. The three nanolayered films prepared had layer thicknesses of 10, 30, and 100 nm. These samples will be discussed more in Chapter 3.

In the second part of this study, CuTa thin film samples were prepared. We used again combinatorial technique to sputter these monolithic samples, and two different substrates, SiO_2 and polyimide sheet, are used in the fabrication process. Secondly, we sputtered two sets of nanolayered samples, and each set contains three nanolayered films with layer thicknesses of 20, 40, and 100 nm and a total thickness of 1μm. These samples will be used and discussed in more detail in Chapter 4.

The sputter rates of source materials mounted on corresponding guns were calibrated previously by using the stylus and optical microscopy to measure the film thickness of the sputtered films in a certain period of time.

Figure 6. VAKSİS Magnetron Sputterer.

The thickness of the samples was checked by both optical and stylus profilometry. An uncoated area was created on each sample using compatible vacuum tape masking half of the substrate. A profilometer was used to scan the samples from left to the right at 5 mm intervals. Figure 7 depicts the tape application and the interface utilized for profilometry. Figure 8 shows the Profilometry measurements of a coated film using a stylus profilometer. This figure indicates the film thickness in different locations of the sample. The sputtering rate is calculated based on the average film thickness values in different locations, considering the sputtering time. The inset shows the result of profilometry at a single location on the sample

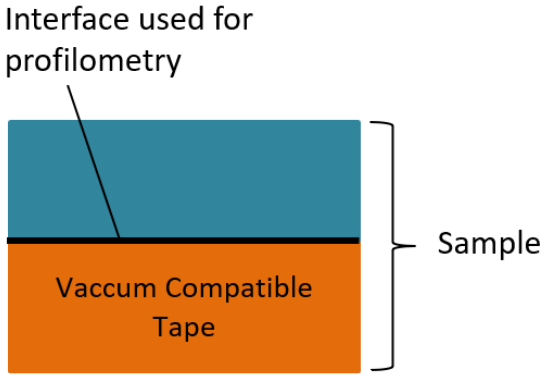

Figure 7. The schematic view of the profilometry measurement.

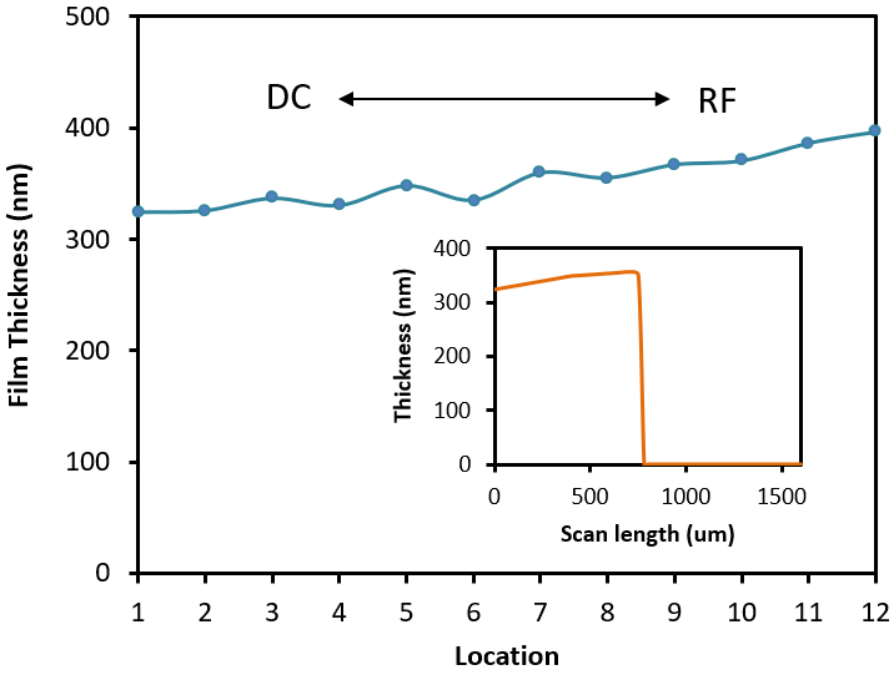

Figure 8. Stylus-profilometry measurements of a Ta film coated at 100 W for 60 minutes. Ta target was located at RF gun. The inset shows the result of the profilometry at a single location on the sample.

2.2 Microstructural Characterization

Several characterization techniques were utilized to characterize the samples' composition and microstructure. X-Ray Diffraction, Scanning Electron Microscopy, Energy-Dispersive X-ray Spectroscopy, Wavelength-Dispersive X-ray Spectroscopy, Focused Ion Beam, Transmission Electron Microscopy, and Atomic Force Microscopy are the most common of these methods. This section will go through each of these briefly.

2.2.1 X-ray Diffraction

To describe the microstructure of the films, X-ray diffraction measurements were done, primarily in terms of crystallography and grain size. The XRD method works by emitting an incident X-ray that interacts with a material's atomic planes and is then diffracted with the same angle of incidence, theta.

The device then measures the intensity of the diffracted rays. The diffractogram's highest intensity angles correspond to crystallographic planes. Using Bragg's Law, the interplanar spacing (*d*) may therefore be simply determined.

$$n\lambda = 2d_{hkl}sin\theta \quad (1)$$

Where *d* is the interplanar spacing, is the X-ray wavelength, and *n* is the order of diffraction. The crystallographic directions of the atomic planes contained in the film are denoted by *hkl*.

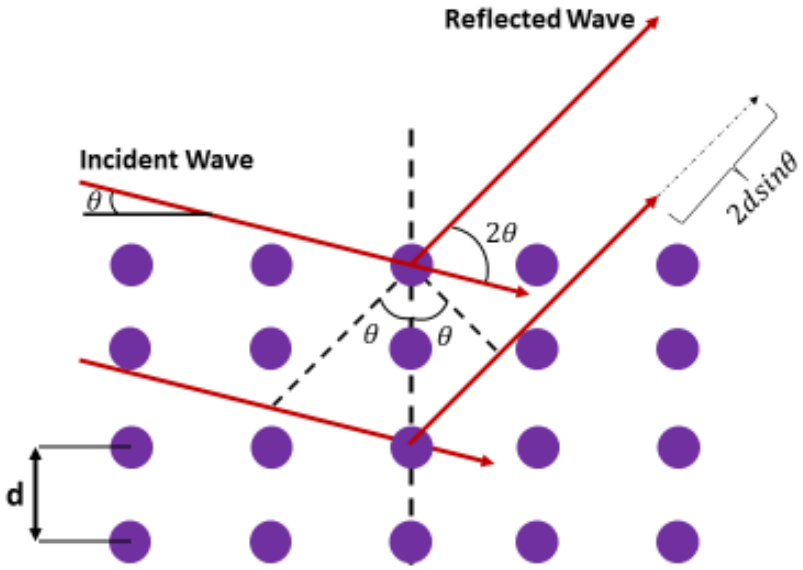

Figure 9. Illustration of Bragg's Law [79].

The Scherrer Equation will then be used to get the estimated crystal size by correlating the peak width (*B*) and crystallite size (*L*):

$$L = \frac{K\lambda}{B(2\theta)cos\theta} \quad (2)$$

Where *K* is a dimensionless number corresponding to the shape factor and *B* is the full width of the related diffraction peak at half maximum (*FWHM*). *K* has a range of acceptable values ranging from 0.89 to 0.94 [79]; we selected 0.9 as an estimate. The equation demonstrates that larger peaks correspond to smaller crystallites. A thorough discussion of the approach and computation may be found in the literature [80]. The XRD measurements on all of the films were taken with a Rigaku Ultima-IV diffractometer in grazing incidence mode at 1°. Jade MDI program used the Scherrer equation to approximate the average crystal size in the films. The wavelength used by the machine is that of copper wavelength, i.e. ($K\alpha$) is 1.5418 Å at 22.85°C.

2.2.2 Scanning Electron Microscopy and Energy-Dispersive X-ray Spectroscopy

Scanning electron microscopy is one of the most used methods for inspecting materials with microscale features. SEM works by directing an electron beam to a specific location on a sample and collecting all of the electrons that resulted from the contact with the sample's surface; these electrons contain a wealth of information about the composition and topography of the scanned sample [81]. Energy-Dispersive X-ray Spectroscopy is a method used in conjunction with SEM that collects the resultant X-ray from contact with the surface. SEM device uses secondary electrons coming from the sample to produce the surface image of the sample in the selected area. Collecting the resultant X-ray emitting from the sample gives us information about the chemical composition of the thin film sample. Surface

imaging and EDS were done in our study using an FEI Quanta 400F scanning electron microscope (SEM).

2.2.3 Focused Ion Beam

Focused Ion Beam milling is a popular technique for machining materials at the micro and even nanoscale. This method was used to create TEM samples and SEM cross-sections. In this study, an FEI Nova 600 Nanolab focused ion beam (FIB) was employed. This system can do FIB and SEM at the same time. Figure 10 depicts a diagram of the system.

To protect the surface from damages, the samples are first coated with platinum. By focusing positive Gallium ions on the surface, the sample is milled into the required form.

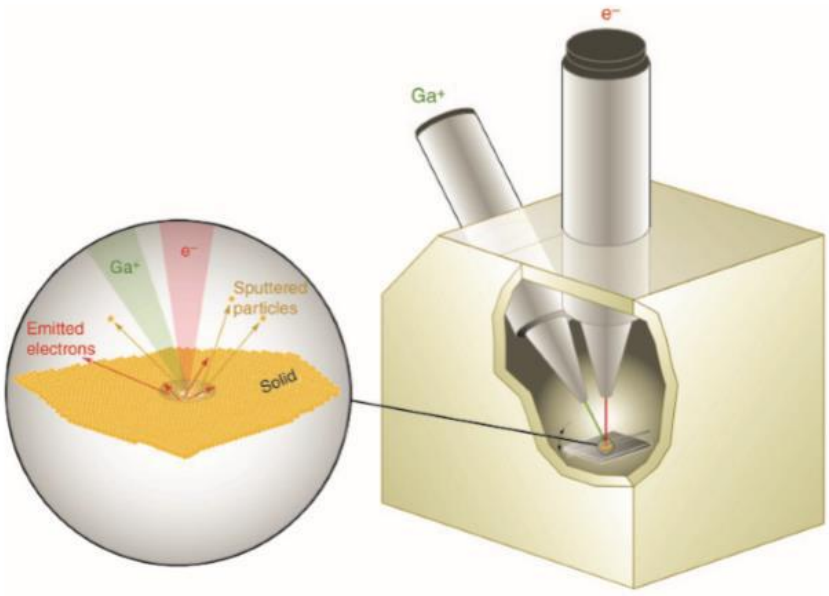

Figure 10. Illustration of FIB and SEM dual system [83].

2.2.4 Transmission Electron Microscopy

Transmission electron microscopy is a method that employs an electron beam to penetrate a sample that is 100 nm thick or thinner in order to produce an image utilizing the electrons transmitted. The image is subsequently magnified and sent to a camera or a fluorescent screen. This method can scan individual atoms and enables for the imaging of very tiny things. The TEM microscopy in this work was performed using a Jeol JEM2100F Field Emission Transmission Electron Microscope. The TEM samples were produced utilizing the lift-out approach using a Nova 600 Nanolab focused ion beam (FEI Company, OR, USA) (see section 2.2.3).

In addition, we deposited 40 nm thick films on transmission electron microscopy (TEM) grids containing 18 nm-thick freestanding SiO_2 windows (by Ted Pella, CA, USA) to verify the amorphous structure. Figure 11 shows a schematic illustration of it in the PVD chamber.

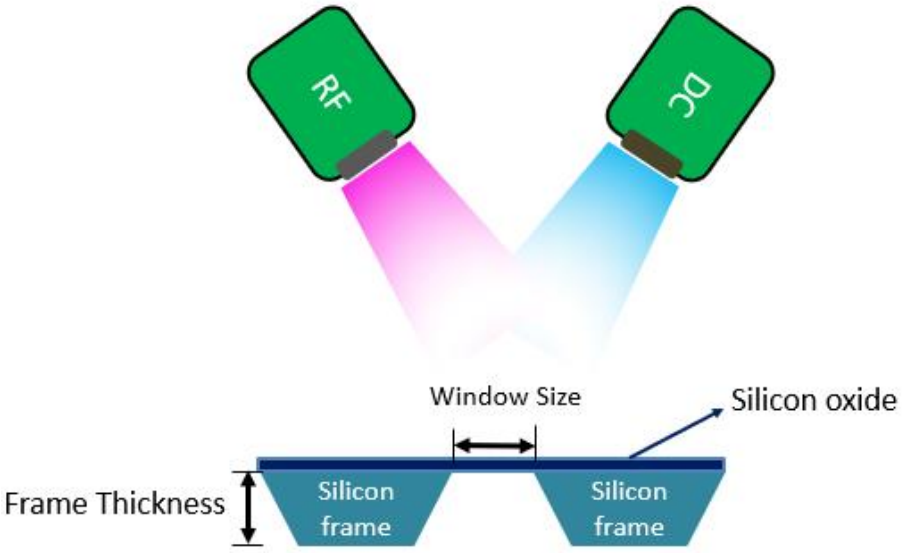

Figure 11. Schematic illustration of TEM grid in the PVD chamber.

2.3 Mechanical Characterization

As previously stated, micromechanical testing has enabled the measurement of a nanomaterial's mechanical characteristics. Hardness, elastic modulus, strength, adhesion, and wear resistance are all micromechanical characteristics that have been described in the literature [17,53–55]. The instruments utilized to perform micromechanical characterization techniques in the thesis study are discussed in this section.

Moreover, some novel techniques are discussed in the literature to facilitate the study of some of the mechanical properties of materials like fracture toughness for thin films [56,57]. The mechanical and micromechanical characterization techniques utilized in the thesis study are discussed in this section.

2.3.1 Nanoindentation

The nanoindentation technique (described in section 1.7.1) was used to determine the hardness and elastic modulus values of all films. The hardness of the films was measured using an Agilent G200 nanoindenter with a Berkovich tip in continuous stiffness measurement mode [84].

2.3.1.1 Nanoindentation-Based Hardness and Elastic Modulus Measurements

Figure 12 depicts a typical load-displacement curve graphically. The hardness and elastic modulus data were analyzed using Nanosuite software, and hardness and elastic modulus values were acquired at a depth of roughly 20% of the total film thickness.

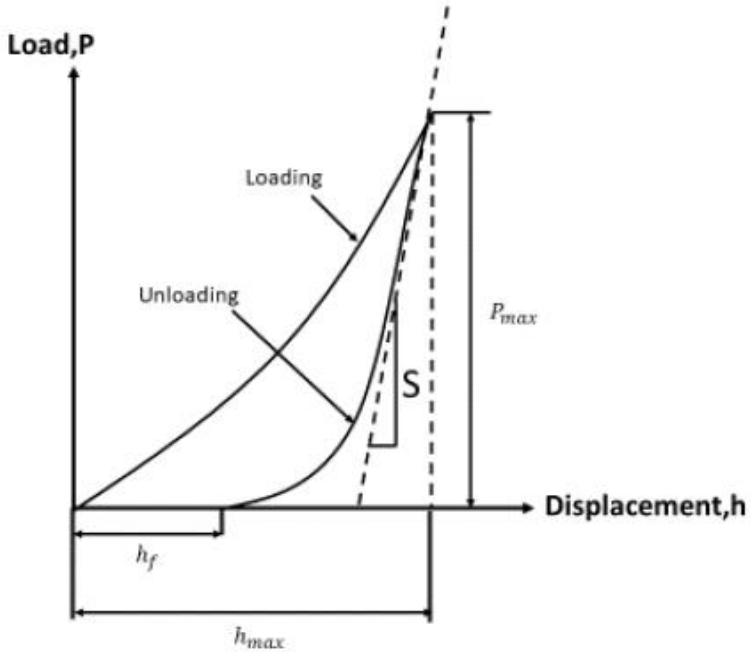

Figure 12. The schematic of a load-displacement curve for indentation [46].

A material's nanoindentation hardness is defined as [58]:

$$H = \frac{P_{max}}{A_p} \tag{3}$$

Where H denotes hardness, P_{max} represents maximum load during indentation, and Ap indicates the projected contact area between the indenter tip and the sample at maximum applied load. The nanoindenter directly detects P_{max}, but calculating the contact area, A_p is difficult. The well-known Oliver-Pharr technique[58] was used to calculate A_p. The complete specifics of this approach may be found in the literature [58], and the procedure is detailed here. The technique begins with calculating the contact stiffness, S, of the indent at the point of greatest load. A power-law curve fit was conducted on the unloading portion of the force-displacement curve in the following form:

$$P = A\left(h - h_f\right)^m \tag{4}$$

Where P is the load as a function of h, which symbolizes the displacement into the surface. h_f is the unloading curve's x-intercept, as seen in Figure 12.

The contact stiffness is then computed as $S = dP / dh$ at h_{max}, where h_{max} is the greatest displacement into the sample. Once the stiffness has been determined, the contact depth, h_c, must be calculated. If a three-dimensional surface is defined as the collection of locations where the tip and the sample come into contact with one other, the contact depth is the height of this surface along the sample surface normal. Sneddon's equation can be used to calculate contact depth:

$$h_c = h_{max} - \epsilon \frac{P_{max}}{S} \tag{5}$$

where for axisymmetric indenters, epsilon is defined as:

$$\epsilon = \frac{2}{\pi}(\pi - 2) \tag{6}$$

The contact depth of the indenter has a clear correlation with the projected area of the contact, which is specified by the geometry of the indenter itself. In our situation, it is the same as a Berkovich tip, which is defined as:

$$A_p = 24.5 h_c^2 \tag{7}$$

A_p is the projected area, so the hardness can be calculated through Equation(3).

2.3.1.2 Nanoindentation-Based Fracture Toughness Measurements

2.3.1.2.1 Stress Analysis Method

The nanoindenter also indented selected specimens using a diamond cube-corner tip for fracture toughness measurements. The fracture toughness of indented materials was proved to be related to the applied force and crack length in the case of a well-developed radial fracture induced by indentation through this equation [85]:

$$K_{IC} = \delta \left(\frac{E}{H}\right)^{\frac{1}{2}} \left(\frac{P}{c^{\frac{3}{2}}}\right) \quad (8)$$

Where P is the applied indentation load, E and H are the elastic modulus and hardness of the film, respectively. δ is an empirical constant that is dependent on the geometry of the indenter. This constant has different values for different indenters like Berkovich and cube corner.

A cube corner tip geometry is a common choice, as it induces higher strains and promotes crack formation more effectively [86] compared to a Berkovich tip that is standard for hardness measurements. Furthermore, for a given depth, the plastic zone under a cube corner is smaller, which can help to reduce the substrate effect [76].

2.3.1.2.2 Energy-Based Method

Indentation-based energy methods to measure fracture toughness of the thin films are briefly discussed in section 1.7.2.1. According to this method, in the case of uncracked films and no excursion and pop-ins appearing in the load-displacement curves, a method based on the analysis of irreversible work in load-displacement can be used to determine fracture toughness.

Based on this method, indentation work can be expressed in the following format:

$$W_t = W_p + U_{fra} + W_e + W_{other} \quad (9)$$

Where W_t is total work, W_p is plastic work; W_e is work of elastic deformation, U_{fra} is the fracture dissipated energy, and W_{other} includes items such as the heat dissipated during indentation and etc., which are ignorable.

In this method, total and elastic works can be calculated directly from load-displacement curves. Irreversible work is the sum of plastic deformation energy, elastic deformation energy, and fracture dissipated energy. By determining W_p, the fracture dissipated energy, and after that, fracture toughness can be calculated.

Our analysis based on the model by Chen [68] is schematically demonstrated in Figure 13.

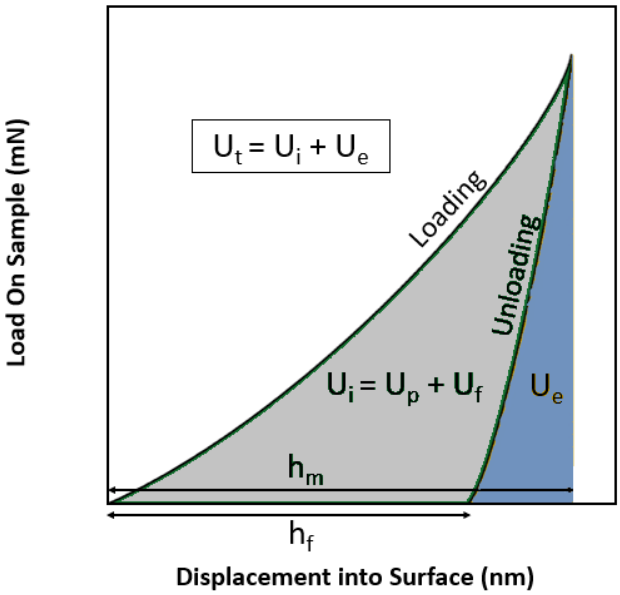

Figure 13. Schematic description of the energy-based fracture toughness formulation. U_e: elastic energy, U_i: irreversible energy, U_t: total energy.

The model defines the area below the load-displacement curve as the total energy spent on the indentation process, U_t. Upon unloading, the stored elastic energy, U_e, is released. Subtraction of the elastic component from the total energy provides the irreversible energy, U_i, corresponding to the plastic deformation and/or fracture of the film [68]:

$$U_i = U_t - U_e \tag{10}$$

Irreversible energy consists of plastic energy, U_p, and energy dissipated by fracture, U_f.

$$U_i = U_p + U_f \tag{11}$$

One can predict the pure plastic component, U_p, based on the analysis of Cheng et al. [87], as follows.

$$U_p = U_t\left(1 - \left[\frac{1 - 3\left(\frac{h_f}{h_m}\right)^2 + 2\left(\frac{h_f}{h_m}\right)^3}{1 - \left(\frac{h_f}{h_m}\right)^2}\right]\right) \quad (12)$$

In this equation, h_f and h_m are the final (residual) and the maximum indentation depths, respectively. Equation (10) and (11) enables the calculation of the fracture energy, U_f and then one can obtain the critical energy release rate, G_c, as [88,89]:

$$G_c = \frac{U_f}{A_m} \quad (13)$$

Where A_m is the contact area between the indenter and specimen at maximum depth. For a cube corner, the contact area is as follows [89]:

$$A_m = 2.6h_m^2 \quad (14)$$

Lastly, the fracture toughness K_c is determined as [89]:

$$K_c = \sqrt{G_c E_r} \quad (15)$$

where E_r is the reduced elastic modulus of the film, calculated as part of the Oliver-Pharr analysis [58,90]:

$$\frac{1}{E_r} = \frac{1 - v_s^2}{E} + \frac{1 - v_i^2}{E_i} \quad (16)$$

In this equation, v is Poisson's ratio, and E is elastic modulus. Subscripts s and i correspond to the sample, and the indenter, respectively.

2.3.2 Tensile Testing

As discussed in the section 1.7.2.2, performing a tensile test on polyimide-supported thin films can be a promising technique to measure fracture toughness and ductility of the thin films. In this experiment, polyimide sheets should be cut into dog bone-shaped rectangular specimens in accordance with the ISO 37 Type II dumbbell

standard and are used as substrates for the deposition process. In this experiment, the Zwick/Roell Z250 universal testing machine is used in order to do tensile tests. All the tests were done under the constant strain rate.

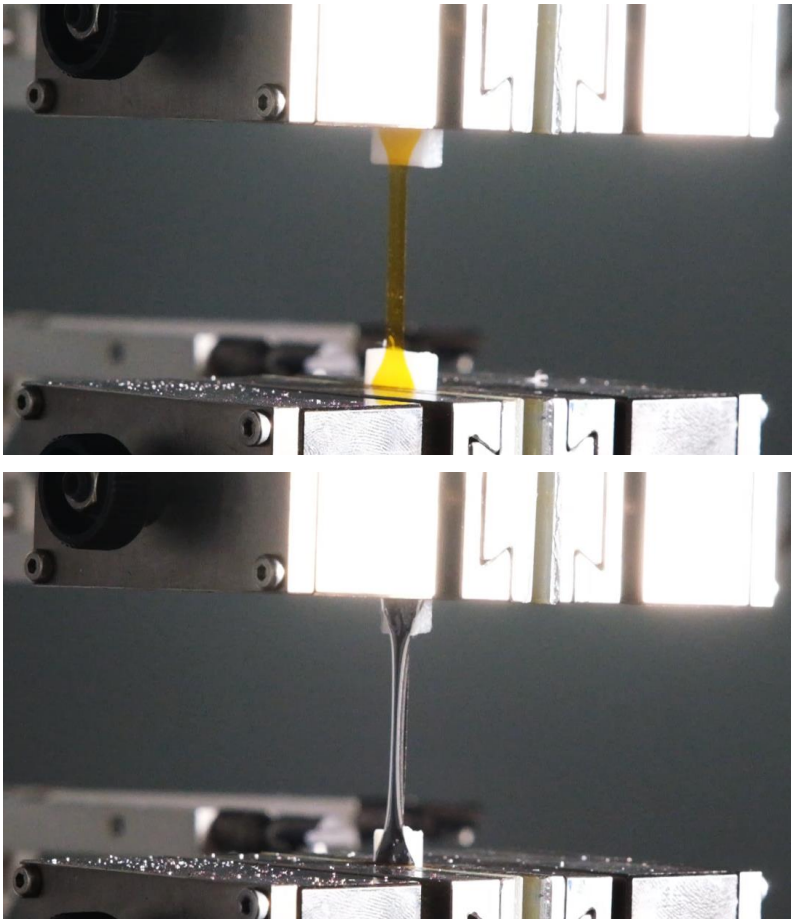

Figure 14. Uncoated (at the top) and coated (at the bottom) polyimide samples under tensile test.

In order to determine the rupture point of the film under tensile test finding the critical resistance is helpful. Critical strain is a strain in which microcracks start to initiate and propagate in film. In order to find critical strain, it needs to measure electrical resistance change during the tensile test at each strain and draw the resistance change versus strain curve for each sample. In resistance change versus

strain curves, critical strain is a point in which the resistance change starts to increase abruptly [56].

During the tensile test, the voltage of the samples (V_{out}) was measured versus the time of the experiment using an electrical circuit. In order to record the voltage versus time data, a program called DEVESOFT is used. The below figure shows a schematic view of the electrical circuit.

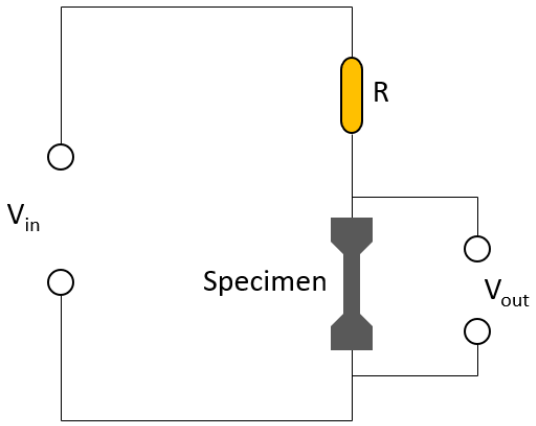

Figure 15. Schematic illustration of the electrical circuit.

In the electrical circuit, the input voltage is 1*V*, and the resistor has a 120 **Ω** resistance. Based on the circuit, the current of the specimen can be calculated like below:

$$I_{sample} = \frac{1 - V_{out}}{120} \tag{17}$$

So, the resistance of the specimen in each millisecond of the test will be calculated through the below equation:

$$R_{sample} = \frac{120\ V_{out}}{1 - V_{out}} \tag{18}$$

In the above equations, V_{out} (Voltage difference between two distinct parts of the sample) is the voltage acquired directly using the DEVESOFT program.

After determination of the resistance of the sample, one can draw electrical resistance change ($R=\Delta R/R_0$) versus the strain curve. So, the critical strain of the films can be acquired.

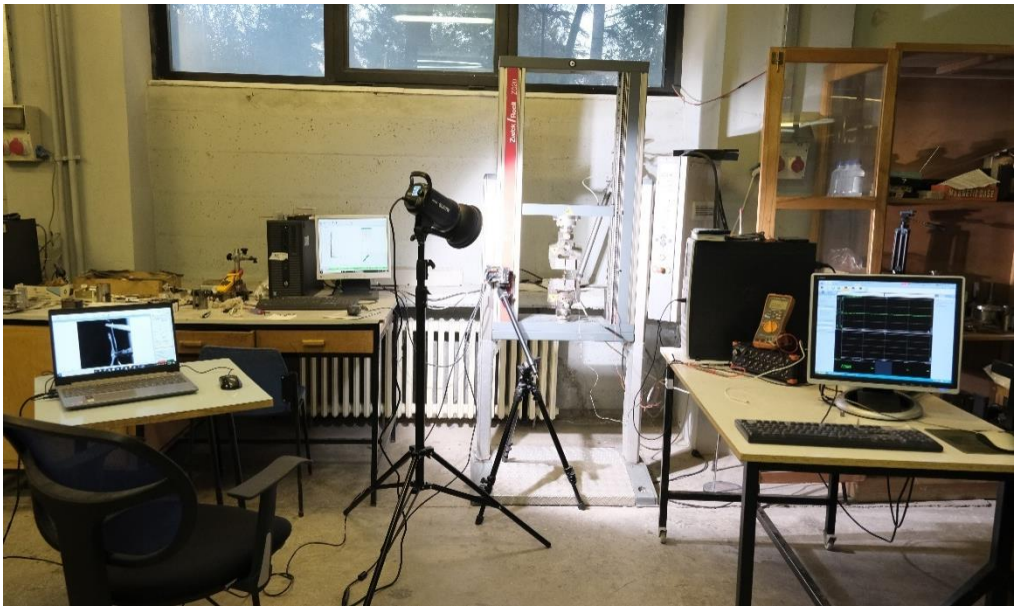

Figure 16. Tensile test and electrical resistance measurements setup.

2.3.2.1 Tensile Test-Based Fracture Toughness Measurements

After doing the tensile test, the force applied to the film can be calculated by subtracting the force applied to the substrate from the total force applied to both film and substrate at each strain, so a separate tensile test should be done on the uncoated polyimide sample [56,57].

$$F_{\mathrm{f}} = F_t - F_{\mathrm{s}} \tag{19}$$

In the above equation, $F_{s,}$ $F_{f,}$ and F_t are the tensile loads of uncoated PI substrate, film, and coated PI specimens.

After determination of tensile load of film, the tensile stress of the film can be calculated as:

$$\sigma = \frac{F_f}{wt} \tag{20}$$

Where *w* and *t* are the width and thickness of the film.

Finding critical strain of the films and having stress-strain curves of them leads to determine fracture stress of the films (σ_f). Fracture stress is a stress corresponding to critical strain in the stress-strain curve. By knowing fracture stress, the energy release rate of the films during the tensile test can be found through an energy model proposed by Beuth in 1992. In this model *G*, the energy release rate of the films can be calculated through below equation [78]:

$$G = \frac{\pi\, \sigma_f^2 h}{2E}(1 - \upsilon^2)\; g(\alpha, \beta) \tag{21}$$

Where E is the elastic modulus of the films derived from stress-strain curves, h is the total thickness of the film, and g(α, β) is a dimensionless value which is a function of elastic modulus between the film and substrate. This dimensionless value can be found by interpolation from the reference [78].

After finding energy release rate values, the fracture toughness of the films can be calculated through an equation proposed by Freund and Suresh [91] :

$$K_{Ic} = \sqrt{\frac{EG}{(1 - \upsilon^2)}} \tag{22}$$

CHAPTER 3

AN INVESTIGATION OF THE ZIRCONIUM-TANTALUM SYSTEM

This chapter is based on the manuscript submitted to "Journal of Alloys and Compounds" titled "Nanostructured ZrTa Metallic Glasses Thin Films with High Strength and Toughness" authored by Ali B. Behboud, Amir Motallebzadeh, and Sezer Özerinç

3.1 Introduction

Numerous studies have previously investigated a large number of binary systems including CuZr [92], CuTi [93], NiZr [94], CuNb [95], CuW [96], CuTa [97], FeZr [98] and TaTi [99] to name a few. The large majority of these studies employed metal pairs with FCC-BCC or FCC-HCP crystal structures in pure form and usually considered a soft and a hard metal, with the latter being a refractory alloy most of the time. On the other hand, the studies on metallic glasses formed by two refractory elements are quite limited. In this study, we explore this route by investigating the binary system of Zr and Ta.

Zr-Ta is one of the promising systems for coating applications, whose constituent elements possess desirable properties [100–102]. The high hardness and desirable biocompatibility characteristics of Zr and Ta in the pure form [100,101,103–105] and the unique combination of the respective tetragonal and HCP phases of Zr and Ta render this pair an interesting model system to explore the glass-forming ability and the structure-property relationships of refractory metallic glass thin film coatings [100–102].

The properties of metallic glasses are very sensitive to the exact composition [106–111]. Because of this, research in this field usually requires the preparation of tens of samples separately. We employed combinatorial sputtering, which provided a

wide range of compositions at a single deposition step. Instead of time-consuming and expensive approaches, this project utilized a recently developed combinatorial sputtering technique. This technique enabled the preparation of continuously varying compositions on the same substrate at a single deposition step.

In this work, first, we investigated the microstructure and mechanical properties such as hardness, elastic modulus, and fracture toughness of ZrTa binary samples with different compositions. The second part of the study investigated nanolayered films composed of alternating layers of $Zr_{35}Ta_{65}$ and $Zr_{70}Ta_{30}$ for layer thicknesses in the range of 10 – 100 nm. This way, the structural heterogeneity is increasing in the nanolayer samples because they consist of alternating layers of amorphous layers with different elastic modulus and hardness. We investigated the microstructure and mechanical properties of Amorphous/Amorphous nanolayered ZrTa samples and examined the effect of inducing nanoscale heterogeneities on their toughness.

3.2 Experimental Details

A magnetron sputterer equipped with two guns deposited all the samples on oxidized silicon substrates. The base pressure of the chamber was about 1×10^{-7} Torr, and the Ar pressure was 2.7×10^{-3} Torr during deposition. Sputtering targets were 2" diameter disks of pure Zr (99.99% purity) and pure Ta (99.99% purity) from Kurt J. Lesker (PA, USA). Ta was sputtered using the RF gun, while Zr was sputtered using the DC gun.

Table 1 shows a list of samples prepared for this work, summarizing the naming convention, compositions, and film thicknesses. We obtained a range of monolithic Zr_xTa_{1-x} films with varying compositions by using combinatorial sputtering. In addition, we prepared pure Zr, pure Ta, and nanolayered $Zr_{35}Ta_{65}$ / $Zr_{70}Ta_{30}$ films using conventional sputtering. The three nanolayered films prepared had layer thicknesses of 10, 30, and 100 nm.

Table 1. Summary of the samples investigated in the ZrTa study.

Sample Name	Description	Thickness
Zr	nanocrystalline Zr	1 μm, monolithic
Ta	nanocrystalline Ta	1 μm, monolithic
Zr_xTa_{100-x}	x = 21 – 70 at.%	~1 μm, monolithic
$Zr_{35}Ta_{65}$ / $Zr_{70}Ta_{30}$ - t	Alternating nanolayers of $Zr_{35}Ta_{65}$ and $Zr_{70}Ta_{30}$	t (layer thickness) = 10, 30, 100 nm

Figure 17 shows a schematic view of the combinatorial sputtering approach. The substrate was a 13 cm × 2 cm single crystal silicon wafer piece with a 1 μm-thick oxide layer, which was divided into 13 pieces of 1 cm × 2 cm upon sputtering. This approach provided 13 specimens at a single sputtering session with varying compositions. We adjusted the power of each gun such that the composition is $Zr_{50}Ta_{50}$ at the midpoint of the substrate.

In addition, we deposited 40 nm thick $Zr_{50}Ta_{50}$, $Zr_{21}Ta_{79,}$ and $Zr_{25}Ta_{75}$ films on transmission electron microscopy (TEM) grids containing 18 nm-thick freestanding SiO_2 windows (by Ted Pella, CA, USA) for the verification of the amorphous structure.

A stylus profilometer verified the thickness of all films. An FEI QUANTA 400F Field Emission SEM (OR, USA) measured the compositions of the films by Energy-dispersive X-ray spectroscopy (EDS) and imaged the indentation marks on selected samples. A Rigaku Ultima IV diffractometer performed X-ray diffraction measurements at grazing incidence mode with an incoming beam at 1°.

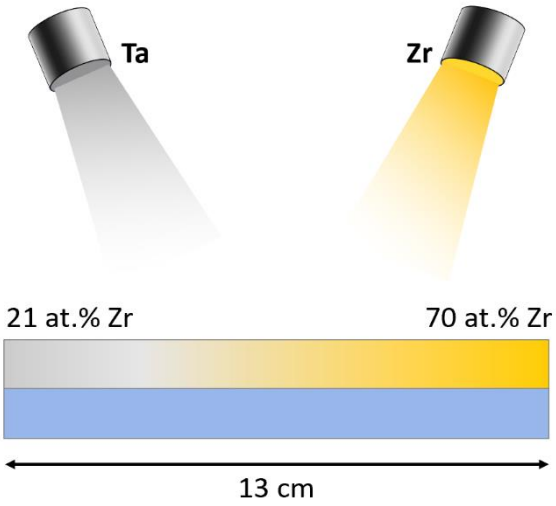

Figure 17. Schematic view of combinatorial sputtering for ZrTa study.

An Agilent G200 nanoindenter (CA, USA) performed nanoindentation hardness measurements using a Berkovich tip in continuous stiffness measurement mode [84]. The indenter repeated the measurements at 15 locations for each sample. Reported hardness values represent the data at a depth around 20% of the film thickness, where the hardness vs. depth curve exhibited a plateau. The nanoindenter also indented selected specimens using a diamond cube-corner tip for fracture toughness measurements.

An FEI Nova 600 Nanolab (FEI, OR, USA) focused ion beam (FIB) prepared cross-sectional foils of $Zr_{35}Ta_{65}$ / $Zr_{70}Ta_{30}$ – 30 nm using the lift-out technique. In addition, 40 nm-thick films of $Zr_{21}Ta_{79}$, $Zr_{25}Ta_{75}$, and $Zr_{50}Ta_{50}$ were sputtered on 18 nm-thick free-standing SiO_2 windows. These samples prepared for transmission electron microscopy (TEM) analyses were imaged by a JEOL JEM2100F TEM at 200 kV in bright field mode.

3.3 Results and Discussion

3.3.1 Microstructure

Figure 18 (a) shows the EDS-measured compositions of the Zr_xTa_{1-x} films prepared by combinatorial sputtering. The Zr concentration monotonically varied in the range of 21 at.% to 79 at.%. The results show that there is approximately a linear variation of composition with the position. Sample #8 had the equiatomic composition of $Zr_{50}Ta_{50}$.

Figure 18 (b) indicates the XRD spectra of all monolithic ZrTa coatings. For the Zr concentrations in the range of 21 – 25 at.%, several crystalline peaks of Ta and Zr are visible. As Zr content increases, these peaks disappear, and for Zr contents of 35 at.% and higher, two broad, amorphous humps become evident. Figure 19 shows the variation of grain size with Zr content, as calculated by the Scherrer equation based on the Ta (212) peak around 38.7°. The grain size of Ta, based on Ta (410) peak around 36.2°, the grain size of Zr, based on Zr (002) peak around 34.8°, are also shown for comparison. Grain sizes of pure Zr and Ta are 19 nm and 21 nm, respectively. The grain sizes of monolithic ZrTa samples are in the range of 10 – 20 nm for the films with crystalline peaks (21 – 25 at.% Zr). The grain size abruptly decreases with increasing Zr content and goes below 2 nm beyond 30 at.% Zr, suggesting an XRD-amorphous structure up to the highest Zr concentration considered in this study – 70 at.%. Figure 19 also shows the variation of d-spacing (or interatomic spacing for the amorphous samples) with Zr content. The interatomic spacing monotonically increases with increasing Zr content, and an opposite trend is evident for the d-spacing.

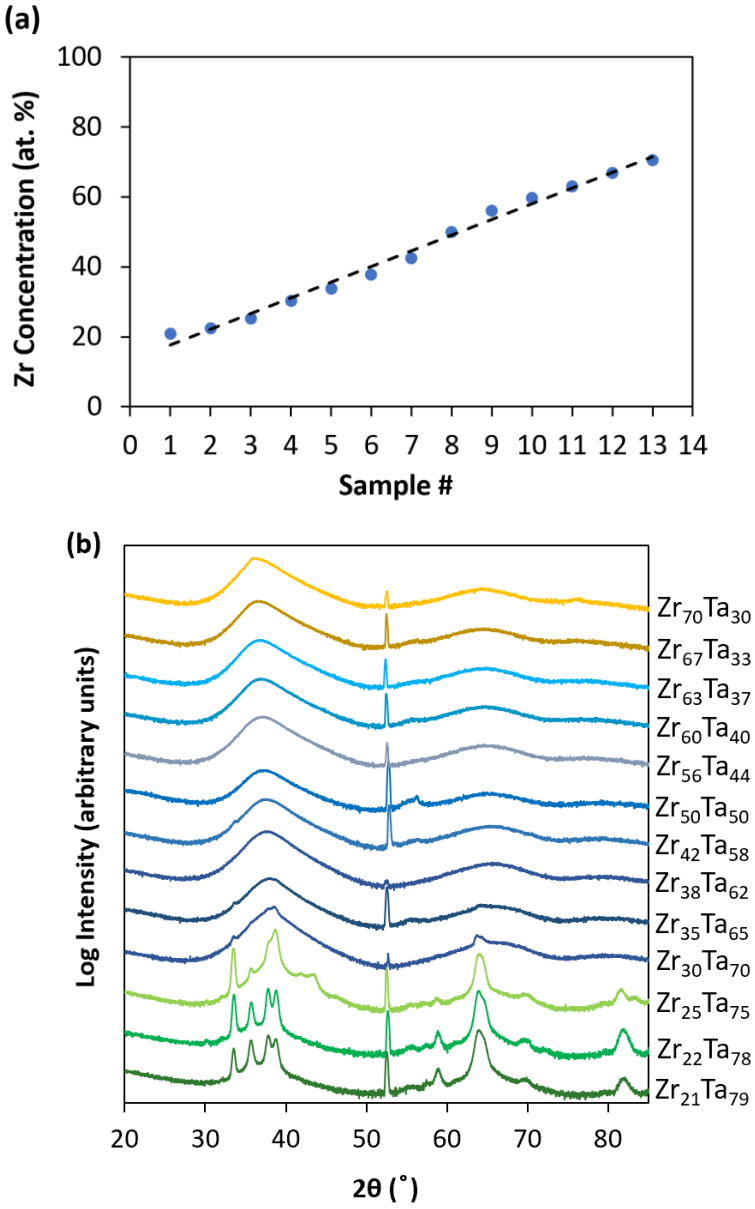

Figure 18. (a) Compositions of the ZrTa films prepared by combinatorial sputtering, as measured by EDS. (b) XRD data of all monolithic ZrTa coatings.

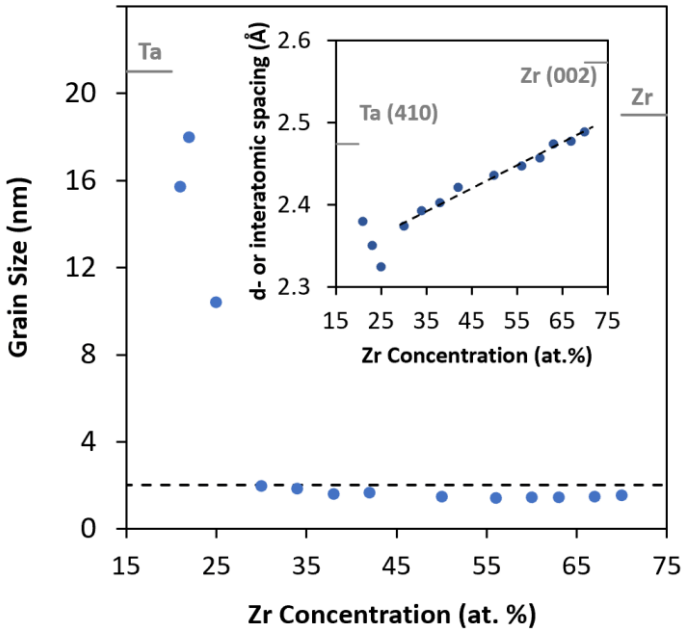

Figure 19. Average grain sizes of monolithic ZrTa coatings, as calculated by the Scherrer equation. The inset shows the variation of d-spacing (or average interatomic spacing) with Zr concentration.

Figure 20 shows the XRD spectra of the films with crystalline peaks and that of pure Ta in further detail. Pure Ta film exhibits several peaks corresponding to the tetragonal crystal structure of Ta (β-Ta). This film has a grain size of about 20 nm, as predicted by the Scherrer equation.

Films in the range of 21 – 25 at.% Zr exhibit Zr and Ta peaks as well as an underlying hump, suggesting the presence of both crystalline and amorphous phases. The Ta peaks of these amorphous films match with those of pure Ta, indicating that the crystalline Ta phase has the same tetragonal crystal structure. On the other hand, Zr peaks with a somewhat lower intensity match with that of HCP Zr. Ta crystals constitute a higher volume fraction of the crystalline phase compared to that of Zr, as Ta peak intensities are considerably higher than those of Zr. All Ta peaks in these films shifted to smaller angles than those of pure Ta, which shows that a considerable amount of Zr is present in Ta crystals in solid solution form. Similarly, there are Zr

peaks shifted towards larger angles, indicating the presence of Ta within the Zr phase.

A slight increase in the Zr concentration from 21 at.% and 25 at.% dramatically change the microstructure. 21 at.% Zr film has high-intensity peaks with a predicted grain size of 18 nm, comparable to the grain size of the pure Ta film. Therefore, the microstructure is dominated by the β-Ta phase. As Ta concentration increases from 21 to 25 at.%, amorphous humps centered around 37° and 65° emerge, with an accompanying widening in the crystalline peaks of Zr and Ta. This transition is a sign of an increase in amorphization, which eventually leads to a fully amorphous structure for Zr concentrations of 30% and higher, as discussed above.

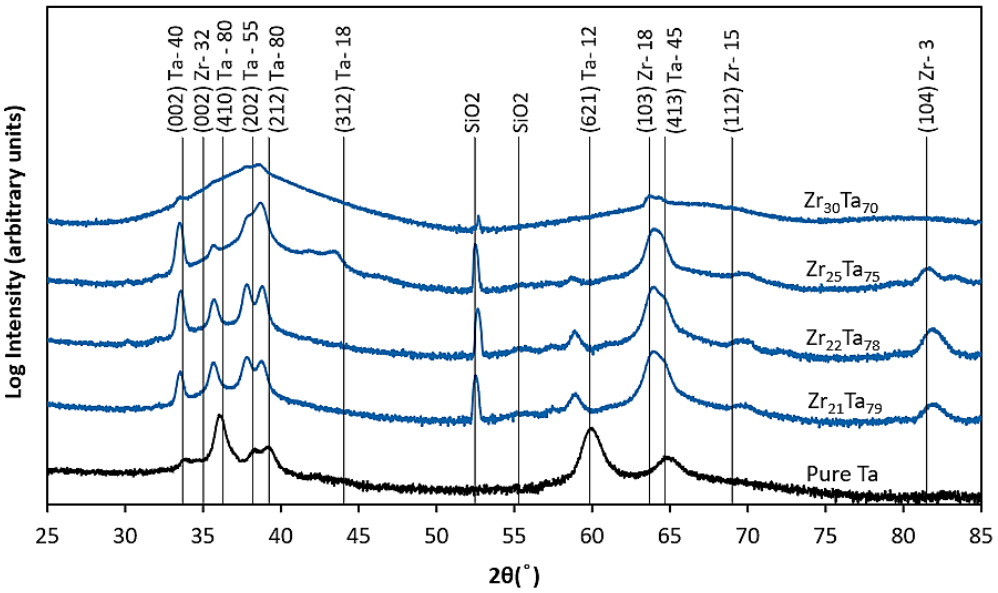

Figure 20. XRD data of $Zr_{21}Ta_{79}$, $Zr_{22}Ta_{78}$, $Zr_{25}Ta_{75}$, $Zr_{30}Ta_{70}$, and pure Ta films.

The positive mixing enthalpy of the ZrTa system and its relatively small atomic radius mismatch [112] suggest a far-from ideal system in terms of the glass-forming ability. The surprisingly wide range of compositions with a fully amorphous structure in our case is the result of the magnetron sputtering approach, which provides cooling rates that are orders of magnitude higher than conventional bulk

rapid solidification techniques. The glass-forming compositional range of sputtered TaZr was previously reported as 27-70 at.% Zr [112], in close agreement with our findings.

As a final note, the peaks around 52.5° and 55° are reflections from the substrate, sometimes called forbidden Si peaks, with intensities depending on the substrate orientation. We observed the presence of these peaks also on uncoated substrates, further verifying that they are not the result of any reflection from the samples.

Figure 21 shows the XRD spectra of all nanolayered ZrTa coatings, consisting of alternating layers of $Zr_{35}Ta_{65}$ and $Zr_{70}Ta_{30}$. Three different layer thicknesses were considered, namely, 10 nm, 30 nm, and 100 nm. The figure also shows the XRD results of the corresponding monolithic films for comparison. There is no major difference between the spectra, suggesting that both $Zr_{35}Ta_{65}$ and $Zr_{70}Ta_{30}$ maintain their amorphous structure when confined into a layered morphology. On the other hand, there is a considerable shift of the peaks to lower angles for smaller layer thickness. We attribute this behavior to the variation in the film stress with layer thickness, a commonly observed behavior in nanolayered films [113].

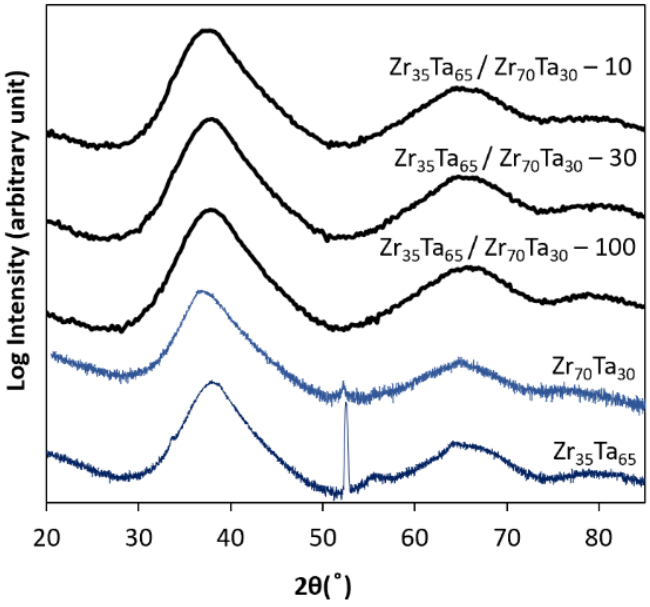

Figure 21. XRD patterns of ZrTa nanolayers and monolithic ZrTa.

Figure 22 shows bright-field TEM images of monolithic films of $Zr_{21}Ta_{79}$, $Zr_{25}Ta_{75}$, and $Zr_{50}Ta_{50}$. $Zr_{50}Ta_{50}$ exhibits a featureless microstructure and a diffraction pattern in the form of a diffuse ring, verifying the XRD predictions of a fully amorphous structure. $Zr_{25}Ta_{75}$, on the other hand, exhibits a distribution of crystallites in a featureless matrix. The diffraction pattern with relatively weak spots confirms the appearance of the crystalline phase at this composition. The average crystallite size is 10.1 nm. With a slight decrease in the Zr concentration, the fraction of the crystalline phase considerably increases, as demonstrated fort the case of $Zr_{21}Ta_{79}$. The accompanying increase in the average crystallite size remains incremental (13.3 nm). Therefore, the additional Ta concentration is mostly accommodated by an increase in the number density of the crystalline domains.

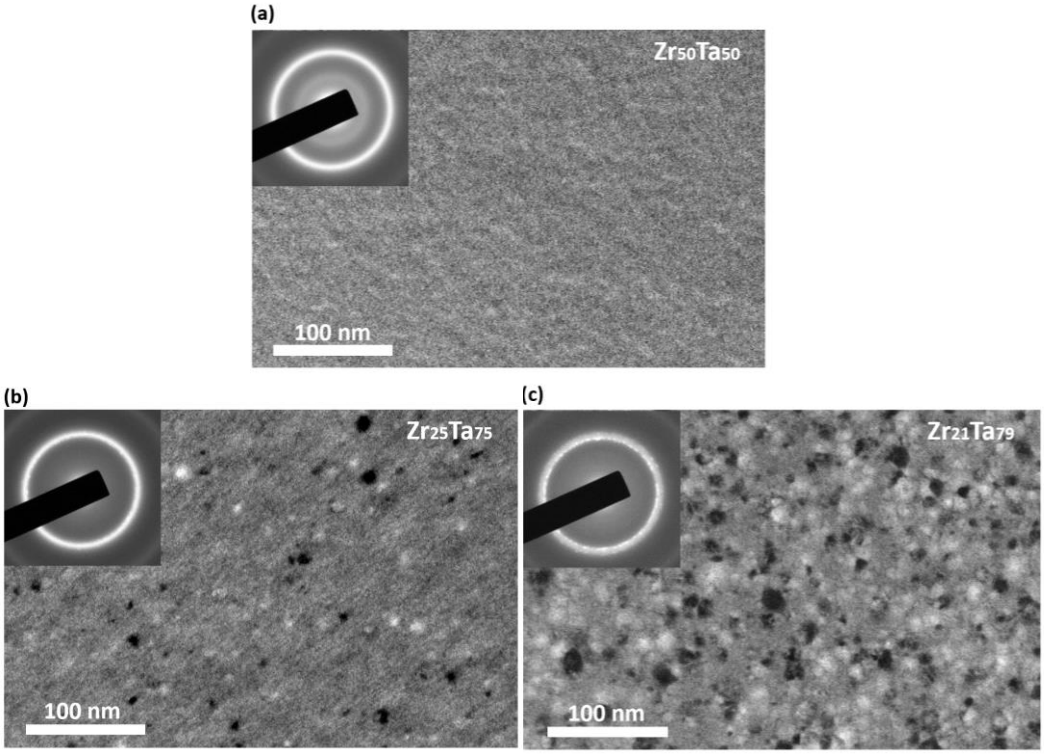

Figure 22. Bright-field TEM images of (a) $Zr_{21}Ta_{79}$, (b) $Zr_{25}Ta_{75}$ and (c) $Zr_{50}Ta_{50}$, deposited on free-standing SiO_2 windows. Insets show the diffraction pattern of the same.

The microstructural features demonstrated by TEM are in close agreement with the XRD results. Although the Scherrer equation is known for its relatively low accuracy at predicting the grain sizes of nanocrystallites, in our case, there is a reasonable agreement between the grain size predictions of TEM and XRD.

Figure 23 illustrates cross-sectional bright-field TEM images of $Zr_{35}Ta_{65}/Zr_{70}Ta_{30}$ nanolayered films with a layer thickness of 30 nm. The modulation, in contrast, verifies the layered structure with two separate compositions. Both layers exhibit a featureless microstructure, showing that the amorphous structure of the monolithic counterparts is maintained.

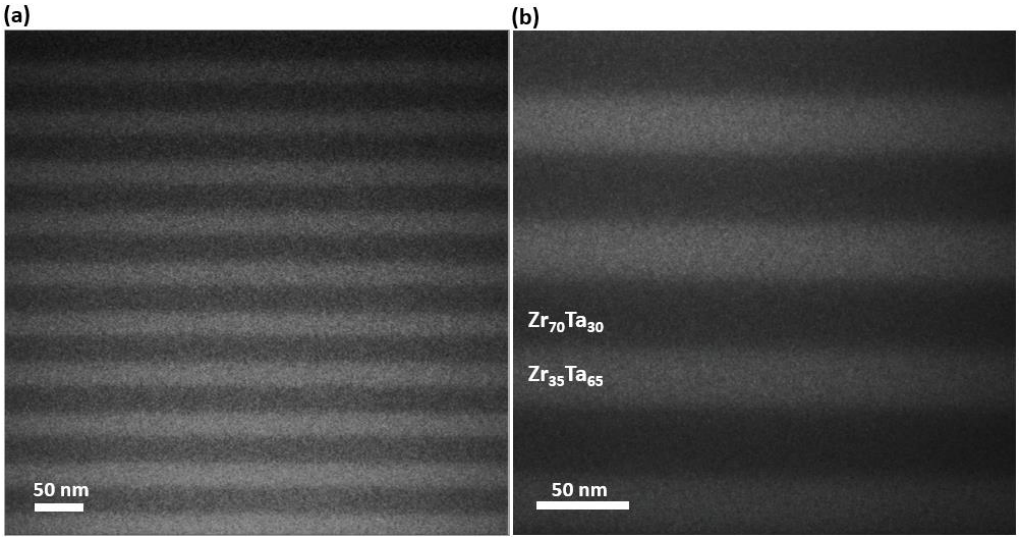

Figure 23. Cross-sectional bright-field TEM images of the nanolayered sample $Zr_{35}Ta_{65}/Zr_{70}Ta_{30}$ – 30.

3.3.2 Hardness and Elastic Modulus

Figure 24 indicates the load-displacement curves of 15 measurements on the $Zr_{50}Ta_{50}$ specimen as an example. The inset of the figure shows hardness variation with depth, as determined by continuous stiffness measurements. The results demonstrate the high repeatability of the indentation measurements.

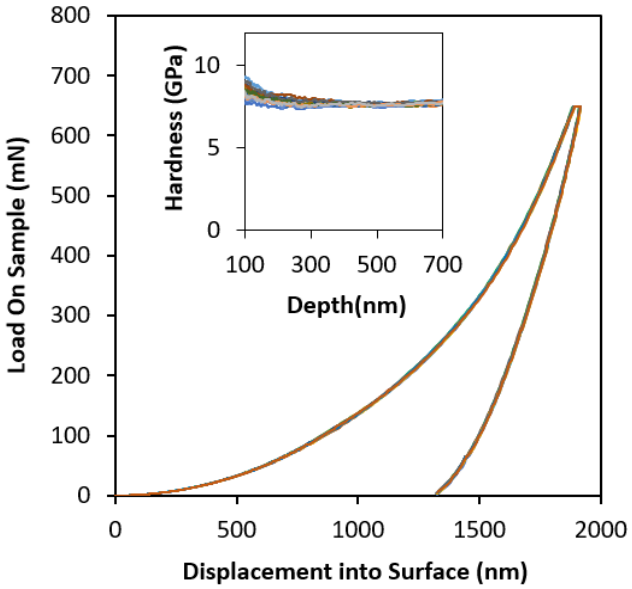

Figure 24. Load-displacement data of $Zr_{50}Ta_{50}$ at 15 different locations. The inset indicates the hardness as a function of indentation depth for the same.

Figure 25 (a) shows the hardness and elastic modulus of pure Ta and pure Zr films, as well as those of monolithic ZrTa films as a function of Ta concentration. Pure Ta and Zr have hardness values of 19.15 GPa, and 6.84 GPa, respectively. The hardness of the ZrTa films exhibits a considerable variation in the range of ~5.5 – 12.5 GPa. The hardness monotonically increases with increasing Ta concentration, and this increasing trend becomes more pronounced for 70 at.% Ta and higher. Elastic modulus data are shown in Figure 25 (b), which has a similar and almost linearly increasing trend with Ta concentration.

Previous measurements on tetragonal Ta (β-Ta) resulted in values of 18.0 GPa [100], 18.7 GPa [114], and 20 GPa [115], which are in good agreement with our results. The hardness of tetragonal Ta is considerably higher than BCC Ta (α-Ta), varying between 10 – 15 GPa [100,114]. This higher hardness of tetragonal Ta is primarily due to the four-layer stacking arrangement, hindering dislocation glide [105]. When it comes to Zr, previous measurements yielded values in the range of 4-7 GPa [116,117]. Our measurements correspond to the higher end of this range, which we

attribute to the partial alignment of the basal planes with the film surface, generating additional resistance to plasticity under the compressive stress state of indentation [45].

Monotonic hardness trends are common for binary systems of metallic glasses, especially when there exists a significant difference between the hardness of the constituent elements; some examples include Cu-Mo [118], Cu-Ta [97], and Cu-W [96]. Comparing the experimental data with the rule of mixture (ROM) predictions is a common approach to gain insight into these trends. The Voigt-type and Reuss-type ROM expressions can be written as follows, respectively.

$$H_V = V_{Zr} H_{Zr} + V_{Ta} H_{Ta} \tag{23}$$

$$H_R = \left(\frac{V_{Zr}}{H_{Zr}} + \frac{V_{Ta}}{H_{Ta}}\right)^{-1} \tag{24}$$

Where *V* indicates the volume fraction and *H* indicates the hardness of the respective constituents.

The ROM-based hardness predictions depicted in Figure 25 (a) are significantly higher than the experimentally determined values. This trend is somewhat opposed to the typical behavior of MGs providing higher hardness than those of the constituents.

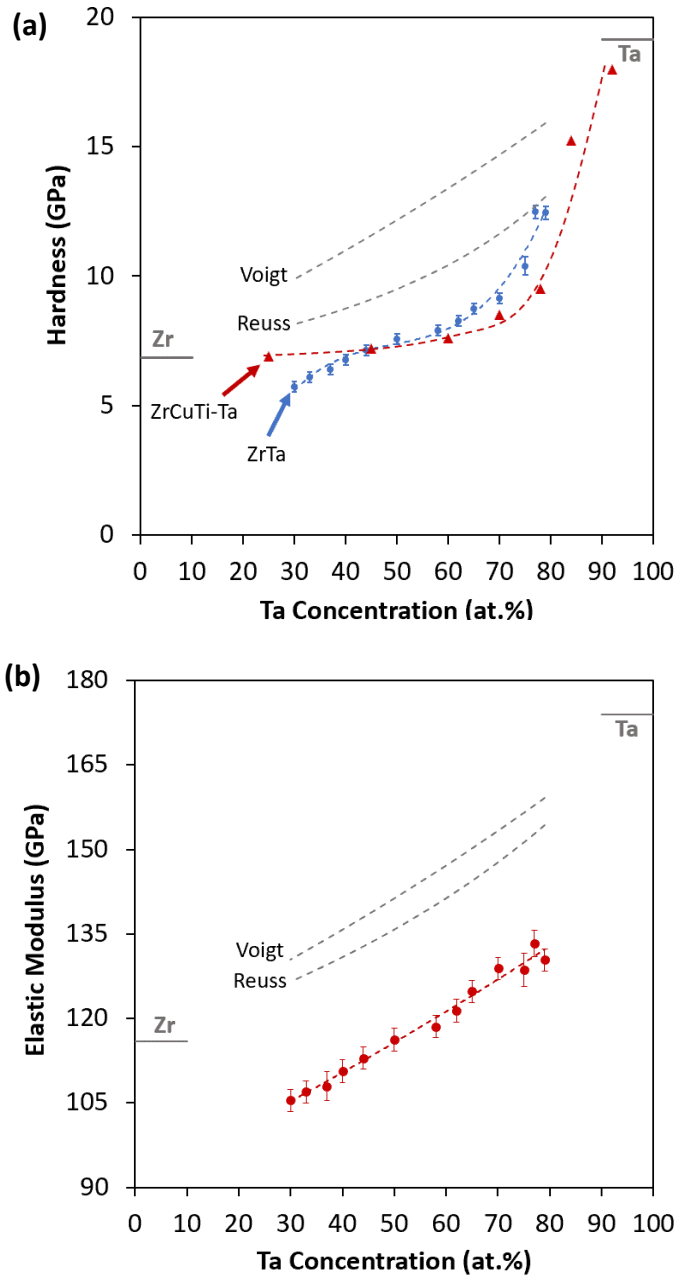

Figure 25. (a) Variation of hardness with Ta concentration, hardness values calculated by Voigt and Reuss rule of mixture models, and hardness variation of ZrCuTi-Ta samples by increasing Ta content. (b) Variation of elastic modulus with Ta concentration and elastic modulus values calculated by Voigt and Reuss rule of mixture models.

The amorphization-induced hardening is primarily due to eliminating the defects and dislocations from the structure, which are responsible for yielding at a small fraction of the theoretical strength for crystalline metals. However, in nanocrystalline Ta, the limited number of slip planes, the high binding energies, and the contribution of Hall-Petch strengthening give rise to a hardness of ~17.5 GPa [97], approaching its theoretical strength. As a result, the advantage of amorphization in the context of hardening diminishes. Nanoindentation measurements on ZrCuTi-Ta metallic glasses with Ta content in the range of 0 – 75 at.% shows a similar trend, with hardness values below the ROM predictions [115]. In fact, there is a remarkable agreement between the hardness of ZrTa and ZrCuTi-Ta, especially in the vicinity of 50 at.% Ta. A similar overprediction of ROM occurs for elastic modulus, as demonstrated in Figure 25 (b). The lower values, in this case, are primarily due to the intrinsically compliant structure of amorphous metals caused by the random atomic configurations and free volume.

Another interesting feature of the data is the significant increase in the slope of hardness for concentrations of about 70 at.% Ta and higher. This transition in hardness matches with the onset of crystallization (see Figure 20). Therefore, we propose that the increasing presence of the β-Ta phase with outstanding hardness causes this behavior, a trend also observed in ZrCuTi-Ta and CuZr-Ta films upon crystallization [115,119].

Figure 26 (a) shows a summary of the hardness results of the nanolayered samples and selected compositions of the monolithic binary alloys. The hardness of the nanolayered films is about 8.5 GPa. The hardness difference between nanolayers with different layer thicknesses is comparable to the standard deviation of the data, suggesting that nanolayers' hardness does not change with layer thickness.

The first observation is that the ~8.5 GPa hardness of the nanolayers is virtually identical to that of $Zr_{35}Ta_{65}$ (8.7 GPa), which is the harder of the constituent layers. This is quite a remarkable result, as the remaining 50% of the composite volume is occupied by $Zr_{70}Ta_{30}$, with a much lower hardness of 5.7 GPa. Before interpreting

this behavior, it is worth discussing the implications of hardness data on yield strength. The average strain under the deformation by a Berkovich tip is about 8% [120]. As strain hardening is mostly negligible in nanocrystalline and amorphous systems, one can conclude that the measured hardness indicates yield strength through Tabor's Equation, $\sigma_y \approx H / 3$ [121]. The hardness of crystalline-crystalline and amorphous-crystalline nanolayers is usually dominated by the softer constituent layers [93,122], as the softer layers are first to yield under load. An exact opposite behavior is a case for ZrTa nanolayers, where the harder phase seems to determine the hardness. We attribute this behavior to the similarity between the length scales of the shear transformation zones and the layer thickness, which promotes co-deformation of the layers. In such a deformation mode, the onset of plasticity can no longer be mediated by the softer layers. Instead, the plastic response becomes a complicated convolution of each layers' atomic configurations, which will delay the yielding to a stress level high enough for the cooperative action of shear transformation zones in each adjacent layer.

The second important observation is the layer-thickness independent hardness of the nanolayers. This behavior is in agreement with the size-independent strength of MGs in general, as demonstrated by micropillar measurements over a wide range of sizes [123]. Literature data on amorphous-amorphous [124] nanolayers exhibit a similar trend. The same is observed in crystalline-amorphous nanolayered films [93] when the amorphous layer is softer than the crystalline counterpart. This size-independent behavior is in stark contrast to the crystalline metals that exhibit grain size [125] and layer thickness-dependent [122] hardness.

When it comes to the elastic modulus data represented in Figure 26 (b), the trends suggest that a ROM approach can predict the behavior of the nanolayered films. This is an expected outcome, as elastic modulus response in a layered system is analogous to a system of springs in series.

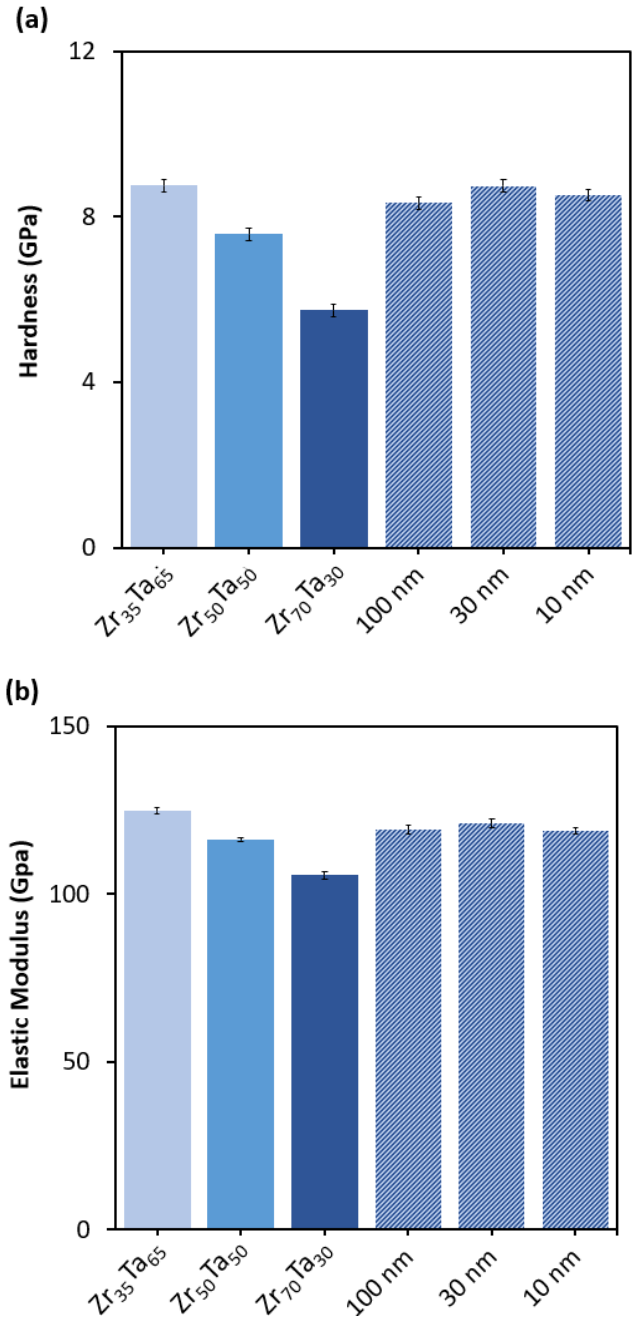

Figure 26. (a) The hardness of monolithic Zr35Ta65, Zr50Ta50, Zr70Ta30, and nanolayered Zr35Ta65/Zr70Ta30 films with different layer thicknesses. (b) shows the same for elastic modulus.

3.3.3 Fracture Toughness

Figure 27 shows load-displacement curves of cube corner indentations on five different compositions of ZrTa. These five cases represent three fully amorphous compositions and two amorphous-crystalline composites with different crystallinity levels. The figure represents five curves for each sample, demonstrating the excellent repeatability of the results.

We analyze the indentation response to predict the fracture toughness of the specimens. The fracture behavior of thin films is a complicated function of the mechanical properties of the film, the substrate, residual stresses, film thickness, and indentation depth [70–76]. When the indentation results in visible cracks, the size, and morphology of these cracks can be used to predict the fracture toughness [126]. In the absence of such cracks. On the other hand, energy-based methods can estimate fracture toughness [76,88,89,127]. Some of these models require pop-in events in the load-displacement curve for the associated calculations. As load-displacement curves of this study do not exhibit any pop-in behavior, we employed an approach proposed by Chen [68] based on the concept of irreversible work. Details of this approach are discussed entirely in the second chapter, section 2.3.1.2.2.

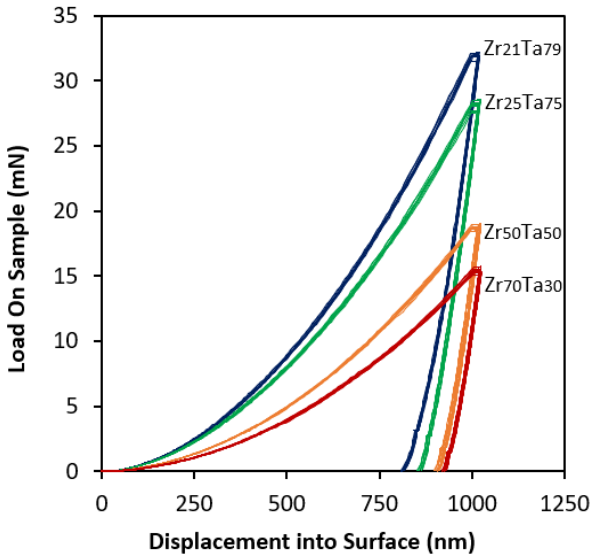

Figure 27. Typical load-displacement curves of cube-corner indentations on monolithic ZrTa films. Five curves were represented for each case.

Figure 28 (a) shows the fracture toughness predictions for pure Ta, pure Zr, and ZrTa films according to the above procedure. The fracture toughness of nanocrystalline Ta, exceeding 8 MPa.m$^{1/2}$, is the highest toughness among the films. Pure Zr has a considerably lower fracture toughness of 3.7 MPa.m$^{1/2}$. The fracture toughness of the fully amorphous films is even lower than that of pure Zr and decreases with increasing Zr concentration, reaching a minimum for $Zr_{70}Ta_{30}$ (2.3 MPa.m$^{1/2}$). Fracture toughness of the metallic matrix-crystalline composite films, on the other hand, provides a considerable improvement over fully amorphous films, and even exceeds that of pure Zr.

First of all, the HCP structure of the Zr thin films with a strong texture causes an unfavorable orientation for plasticity and is the primary reason for the relatively low fracture toughness value. Pure Ta, on the other hand, exhibits the highest toughness among the films considered here. This is due to the larger number of slip systems of β-Ta, which is considerably more ductile than α-Ta [100]. The even lower toughness of the amorphous films is an expected result due to the featureless microstructure facilitating the catastrophic propagation of shear bands [128], combined with the size

effects previously observed for Zr-based thin film metallic glasses [94]. $Zr_{70}Ta_{30}$, the hardest of all binary alloys considered in this study, also exhibits the lowest toughness, providing an example for the well-known strength-ductility trade-off [129].

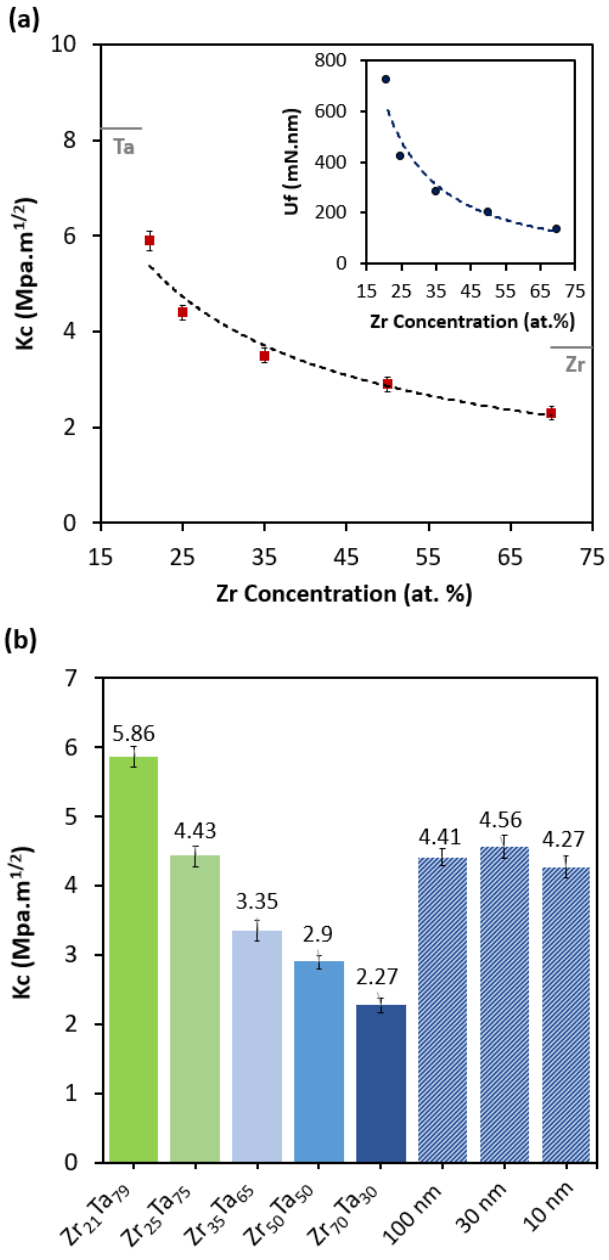

Figure 28. (a) Fracture toughness predictions for five different compositions of ZrTa, pure Zr, and pure Ta. (b) Fracture toughness predictions of nanolayers compared to several monolithic ZrTa films.

The toughness offered by $Zr_{25}Ta_{75}$ corresponds to ~100% improvement compared to the monolithic $Zr_{70}Ta_{30}$. This considerably higher fracture toughness can be explained by the presence of the crystalline phase, which effectively hinders the catastrophic propagation of shear bands and forces the structure to accommodate further plasticity through secondary shear bands before fracture [130]. $Zr_{21}Ta_{79}$ has a higher volume fraction of the crystalline phase compared to Zr_{25}, providing a denser network of secondary particles for inhibiting fracture. As a result, it exhibits an even higher fracture toughness with an improvement of about 30% compared to Zr_{25}.

Figure 28 (b) shows the fracture toughness of the $Zr_{35}Ta_{65}/Zr_{70}Ta_{30}$ nanolayers, together with those of the monolithic ZrTa films. Nanolayered films have a fracture toughness around 4.5 MPa.$m^{1/2}$, and the layer thickness does not have a strong influence on the toughness.

First of all, we can compare the fracture toughness of the nanolayers with those of the monolithic films $Zr_{70}Ta_{30}$ and $Zr_{35}Ta_{65}$, which correspond to the two compositions forming the nanolayered films. $Zr_{70}Ta_{30}$ and $Zr_{35}Ta_{65}$ have toughness values of 2.27 MPa.$m^{1/2}$ and 3.35 MPa.$m^{1/2}$, respectively, and nanolayered films' toughness of 4.5 MPa.$m^{1/2}$ is significantly higher. In fact, the fracture toughness of the nanolayered films is higher than any other fully amorphous compositions considered here.

The results constitute the first experimental demonstration of toughness improvements in a fully amorphous film through a nanoscale modulation in composition. The unique properties of MGs with heterogeneities at the nanoscale can explain these findings [131]. Such heterogeneities, caused by phase separation or a particular medium-range order, have been the subject of several simulations [132,14] and experimental studies [131,133,134] focusing on the implications of such features on mechanical behavior. These modulations in the local atomic order and physical properties have been shown to improve the ductility and the toughness of MGs considerably [134,135]. While the details of the toughening behavior are not

fully understood, the initial findings suggest a classical mechanics-based approach can explain the results. In this interpretation, the softer regions of the metallic glass mediate the initial stages of plastic deformation, and the harder phase hinders the catastrophic propagation of localized deformation [132]. As stress levels increase, the harder phase starts to deform as well, and the co-deformation scheme enables the maintenance of a remarkable level of ductility.

Once can obtain further insight into the implications of the data, by calculating the plastic energy of each film, according to Equation (12*).*

Figure 29 shows the plastic energy, U_p, for pure Ta, pure Zr, $Zr_{50}Ta_{50}$, $Zr_{70}Ta_{30}$, and the nanolayers. The data more clearly indicate the superior accommodation of the plasticity in the nanolayers, which almost reaches that of a fully crystalline Zr. While the fracture toughness values are virtually the same for each layer thickness among the nanolayers, an interesting trend for the case of U_p is the relatively lower plastic energy of the nanolayers with 100 nm layer thickness. This is in line with the previous work suggesting that the effectiveness of heterogeneity diminishes as the size scale governing the modulations becomes considerably larger than the size scale of the fundamental plasticity mechanism, namely shear transformation zones, with sub-10 nm size [14,136,137].

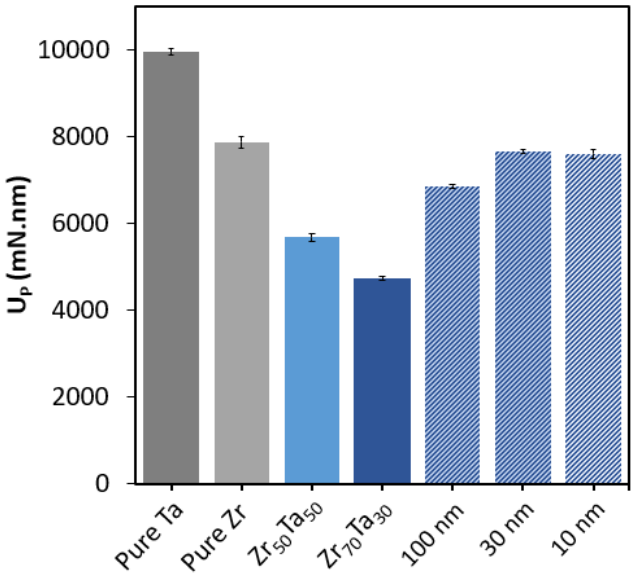

Figure 29. Plastic energy amount induced in the pure Ta, pure Zr, Zr50Ta50, Zr70Ta30 samples and nanolayers during displacement control nanoindentation.

Figure 30 (a) shows the SEM images of cube corner indentation marks on $Zr_{21}Ta_{79}$, $Zr_{25}Ta_{75}$, $Zr_{50}Ta_{50}$, and $Zr_{70}Ta_{30}$ monolithic films, and

Figure **30** (b) shows the same for the nanolayered films. The maximum depth was 1 μm in all of these indentations. As mentioned previously, radial cracks do not appear in any of these indentations, which is a commonly observed behavior when the elastic limit of the substrate is larger than that of the coating ($E_f / H_f > E_s / H_s$). Radial cracks are more frequently encountered in the opposite scenario, where the considerable deformation of the substrate and the bending of the coating promotes radial cracking during indentation [76].

SEM images of $Zr_{50}Ta_{50}$ and $Zr_{70}Ta_{30}$ exhibit pile-ups appearing around the edges of the indentation mark. These pile-ups have the form of stepped arcs, which are the signs of shear band formation in these two samples [138,139]. The spacing between shear bands is larger for the case of $Zr_{50}Ta_{50}$, which is in line with the increasing fracture toughness with increasing Zr content. When it comes to $Zr_{21}Ta_{79}$, the shear bands completely disappear, and only a sign of smooth pile-up remains, suggesting

that the density of the crystalline phase is now high enough to mediate homogeneous plasticity.

When it comes to the $Zr_{35}Ta_{65}/Zr_{70}Ta_{30}$ nanolayered films, we observe a larger number of shear bands compared to the cases of the fully glassy $Zr_{50}Ta_{50}$ and $Zr_{70}Ta_{30}$. In other words, the shear band spacing is smaller than the monolithic MGs, a sign of improved ductility. The shear band spacing further decreases with a decrease in layer thickness, suggesting that the modulated structure triggers a more extensive network of shear bands for smaller layer thicknesses.

Lastly, the implications of the modulated MG design for both fundamental and applied studies deserve an explanation. The studies so far in the development of heterogeneous MGs have mostly utilized specific alloy designs or complicated thermal/mechanical processing routes to induce the nanoscale heterogeneities. While these studies have been of crucial importance, especially for understanding the underlying physics and developing new bulk MGs, they did not provide means for directly engineering the length scales and modulation amplitudes of the heterogeneities. Our approach, on the other hand, enables such precise control of the modulation parameters and provides a systematic framework for both fundamental and applied studies. Basic studies on this matter should focus on the identification of the relationships between the modulation characteristics and mechanical properties, and applied studies can attempt to optimize mechanical properties for coating applications accordingly.

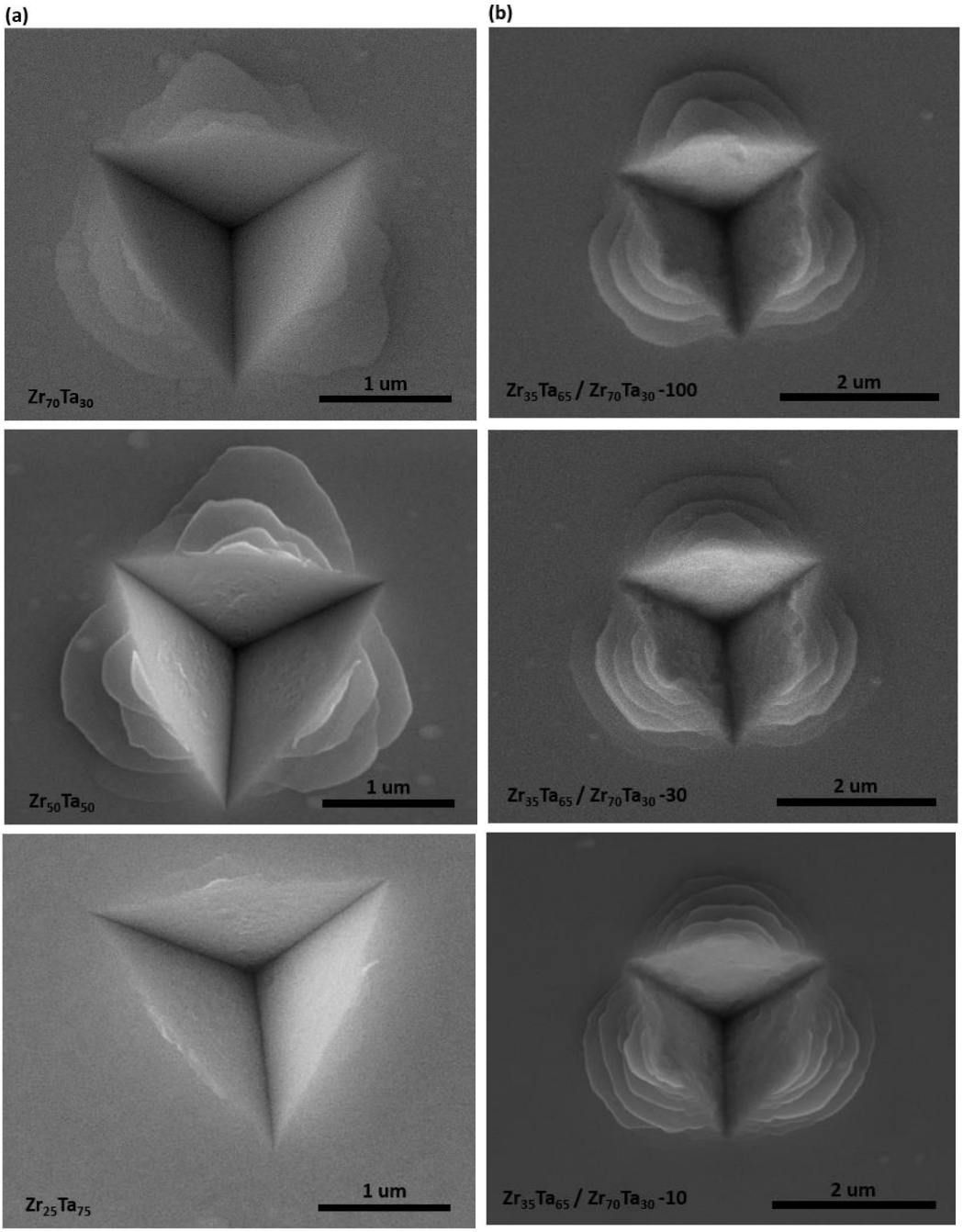

Figure 30. (a) SEM images of cube corner indentations on Zr25Ta75, Zr50Ta50, and Zr70Ta30 monolithic samples. (b) SEM images of cube corner indentation on Zr35Ta65/Zr70Ta30 nanolayers with different layer thicknesses.

3.4 Conclusions

The study investigated the structure-property relationships in the ZrTa system. The microstructural transition from a fully amorphous alloy to an amorphous-crystalline composite has a significant impact on the mechanical properties. Specifically, the semi-crystalline $Zr_{21}Ta_{79}$ combines high hardness with improved fracture toughness due to the unique combination of a hard crystalline phase and a softer amorphous matrix.

The fully amorphous ZrTa films with modulated composition demonstrated a balanced combination of hardness and ductility and provided an improvement over MG films with homogeneous composition. Therefore, the nanolayered MG concept provides a new and effective route to the development of heterogeneous MG coatings with optimized strength and ductility.

CHAPTER 4

AN INVESTIGATION OF THE COPPER-TANTALUM SYSTEM

4.1 Introduction

Some studies have previously investigated the glass-forming ability of some binary alloy systems, typically known as immiscible metallic alloys such as Cu-W [140], Cu-Co [141], and Cu-Ta [97,142]. According to the binary phase diagrams, there are many immiscible systems in which the two components are entirely immiscible in the liquid phase because of the positive enthalpy of formation [143]. This immiscible effect makes the production of such bulk samples complex without macro-segregation [97]. However, physical vapor deposition makes the glass formability of these immiscible alloys possible in the thin-film form. As a typical of immiscible alloy systems, the Cu-Ta system has been the topic of several studies focused on whether amorphization can be accomplished in an alloy system with positive heat of formation [144,145]. Producing metallic glasses or amorphous materials and using them is one of interest for scientists. Cu–Ta amorphous alloy is one of the promising systems for coating applications because constituent elements possess desirable properties. The high hardness, high heat and wear resistance, and desirable biocompatibility properties of Ta in its pure form [100,105], as well as the significant atomic radius difference between Ta and Cu, make this pair an attractive model as a system that combines excellent mechanical properties and remarkable stability at high temperatures [97].

Moreover, recent studies on CuTa binary alloy system show that this system has the capability to offer a wide compositional range of amorphous structure and, as a result, a wide spectrum of mechanical properties in the amorphous phase [97,146]. Due to this reason, as similarly discussed in Chp.3, this capability of the CuTa system

provides an opportunity for perfect modulation of mechanical properties and heterogeneity enhancement in the fabrication of nanolayered samples.

All the overmentioned details render this pair an interesting model system to explore the structure-property relationships of metallic glass thin film coatings.

We employed combinatorial sputtering, which provided a wide range of compositions at a single deposition step. Instead of time-consuming and expensive approaches, this project utilized a recently developed combinatorial sputtering technique. This technique enabled the preparation of continuously varying compositions on the same substrate at a single deposition step.

In this work, first, we investigated the microstructure and mechanical properties such as hardness, elastic modulus, and fracture toughness of CuTa binary samples with different compositions. The second part of the study investigated two sets of Amorphous/Amorphous and Crystalline/Amorphous nanolayered films. The Amorphous/Amorphous nanolayers are composed of alternating layers of $Cu_{40}Ta_{60}$ and $Cu_{75}Ta_{25}$ for layer thicknesses in the range of 20 – 100 nm. The Crystalline/Amorphous nanolayers are composed of alternating $Cu_{25}Ta_{75}$ semi-crystalline and $Cu_{75}Ta_{25}$ amorphous layers. This way, we try to investigate the effect of enhanced structural heterogeneity on the mechanical properties of the samples, and moreover, we can investigate the effect of introducing crystalline to amorphous structures on mechanical properties such as ductility and toughness.

4.2 Experimental Details

A magnetron sputterer equipped with two guns deposited all the samples on oxidized silicon substrates. The base pressure of the chamber was about 1×10^{-7} Torr, and the Ar pressure was 2.7×10^{-3} Torr during deposition. Sputtering targets were 2" diameter disks of pure Cu (99.99% purity) and pure Ta (99.99% purity) from Kurt J. Lesker (PA, USA). Ta was sputtered using the DC gun, while Cu was sputtered using the RF gun.

Table 2 shows a list of samples prepared for this work, summarizing the naming convention, compositions, and film thicknesses. We obtained a range of monolithic Cu_xTa_{1-x} films with varying compositions by using combinatorial sputtering. In addition, we prepared nanolayered $Cu_{75}Ta_{25}$ / $Cu_{40}Ta_{60}$ and $Cu_{75}Ta_{25}$ / $Cu_{25}Ta_{75}$ films on SiO_2 using conventional sputtering. The six nanolayered films prepared had layer thicknesses of 20, 40, and 100 nm.

Table 2. Summary of the samples investigated in the CuTa study.

Sample Name	Description	Thickness
Cu_xTa_{100-x}	x = 25 – 84 at.%	~1 μm, monolithic
$Cu_{75}Ta_{25}$ / $Cu_{40}Ta_{60}$ - t	Alternating nanolayers of $Cu_{75}Ta_{25}$ and $Cu_{40}Ta_{60}$	t (layer thickness) = 20, 40, 100 nm
$Cu_{75}Ta_{25}$ / $Cu_{25}Ta_{75}$ - t	Alternating nanolayers of $Cu_{75}Ta_{25}$ and $Cu_{25}Ta_{75}$	t (layer thickness) = 20, 40, 100 nm

Figure 32 shows a schematic view of the combinatorial sputtering approach in the CuTa system. The substrate was a 12 cm × 2 cm single crystal silicon wafer piece with a 1 μm-thick oxide layer, which was divided into 12 pieces of 1 cm × 2 cm upon sputtering. This approach provided 12 specimens at a single sputtering session with varying compositions. We adjusted the power of each gun such that the composition is $Cu_{50}Ta_{50}$ at the midpoint of the substrate. Moreover, we deposited a Cu-rich semi-crystalline (Cu84Ta16), Ta-rich semi-crystalline (Cu25Ta75), full amorphous (Cu50Ta50), $Cu_{75}Ta_{25}$ / $Cu_{40}Ta_{60}$ – 20 nm and $Cu_{75}Ta_{25}$ / $Cu_{25}Ta_{75}$ – 20 nm thin films on polyimide substrates to perform tensile test on them.

The polyimide sheet was cut into dog bone-shaped rectangular specimens in accordance with the ISO 37 Type II dumbbell standard with 4×20 mm^2 gauge area and are used as substrates for the deposition process. In this experiment, the Zwick/Roell Z250 universal testing machine is used in order to do tensile tests. All the tests were done under the constant strain rate of 4×10^{-4} s^{-1} at room temperature. The electrical resistance of the samples was measured using an electrical circuit and recorded using DEVESOFT software (section 2.3.2).

Figure 31. Coated polyimide substrates.

A stylus profilometer verified the thickness of all films. An FEI QUANTA 400F Field Emission SEM (OR, USA) measured the compositions of the films by Energy-dispersive X-ray spectroscopy (EDS) and imaged the indentation marks on selected samples. A Rigaku Ultima IV diffractometer performed X-ray diffraction measurements at grazing incidence mode with an incoming beam at 1°.

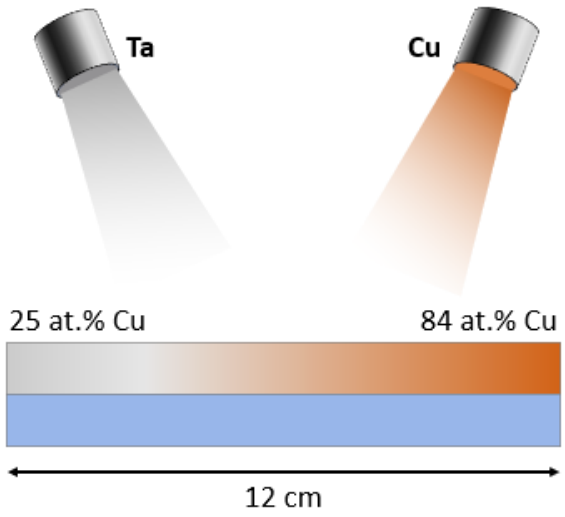

Figure 32. Schematic view of combinatorial sputtering for the CuTa study.

An Agilent G200 nanoindenter (CA, USA) performed nanoindentation hardness measurements using a Berkovich tip in continuous stiffness measurement mode [84]. The indenter repeated the measurements at 16 locations for each sample. Reported hardness values represent the data at a depth around 20% of the film thickness, where the hardness vs. depth curve exhibited a plateau. The nanoindenter also indented selected specimens using a diamond cube-corner tip for fracture toughness measurements.

4.3 Results and Discussion

4.3.1 Microstructure

Figure 33 shows the EDS-measured compositions of the Cu_xTa_{1-x} films prepared by combinatorial sputtering. The Ta concentration monotonically varied in the range of 16 at.% to 75 at.%. The results show that there is approximately a linear variation of

composition with the position. Sample #6 had the equiatomic composition of $Cu_{50}Ta_{50}$.

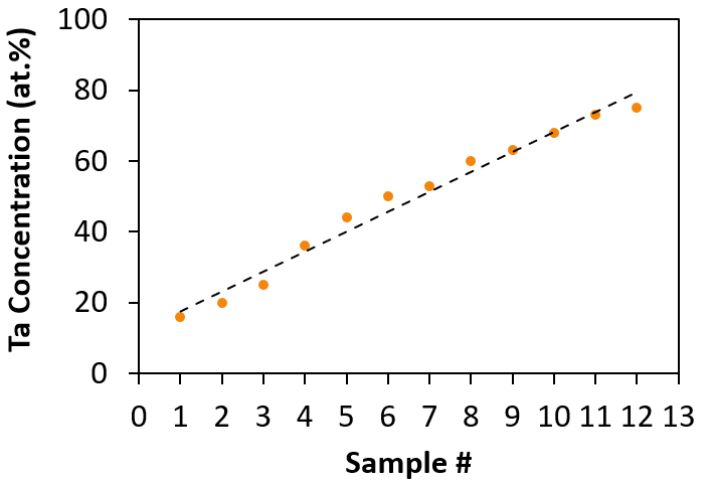

Figure 33. Compositions of the CuTa films prepared by combinatorial sputtering, as measured by EDS.

Figure 34 indicates the XRD spectra of all monolithic CuTa coatings. For the Ta concentrations in the range of 68 – 75 at.%, several crystalline peaks of Ta are visible. Reference XRD spectrum information such as material crystalline plane and intensity of each peak is illustrated next to each peak. As Ta content decreases, these peaks disappear, and for Ta contents of 25-63 at.%, two broad, amorphous humps become evident. For the Ta concentrations in the range of 16 – 20 at.%, a crystalline peak of Cu appears around 72°, corresponding to Cu (220) crystalline plane.

Films in the range of 68 – 75 at.% Ta exhibit Ta peaks as well as an underlying hump, suggesting the presence of both crystalline and amorphous phases. The Ta peaks of these amorphous films match with peaks corresponding to the tetragonal crystal structure of Ta (β-Ta), indicating the presence of crystalline Ta β-phase in the structure of these metallic glass-crystalline composites. All Ta peaks in these films shifted to larger angles than crystalline peaks of Ta, which shows that a considerable

amount of Cu is present in Ta crystals in solid solution form. Similarly, in the samples with Ta concentrations in the range of 16 – 20 at.% Cu (220) peak shifted towards smaller angles, indicating the presence of Ta within the Cu phase.

A slight decrease in the Ta concentration from 68 at.% to 63 at.% dramatically changes the microstructure. As Ta concentration decreases from 68 to 63 at.%, amorphous humps centered around 37° and 65° emerge, with an accompanying widening in the crystalline peaks of Cu and Ta. This transition is a sign of an increase in amorphization, which eventually leads to a fully amorphous structure for Ta concentrations of 63 at.% to 25 at.%.

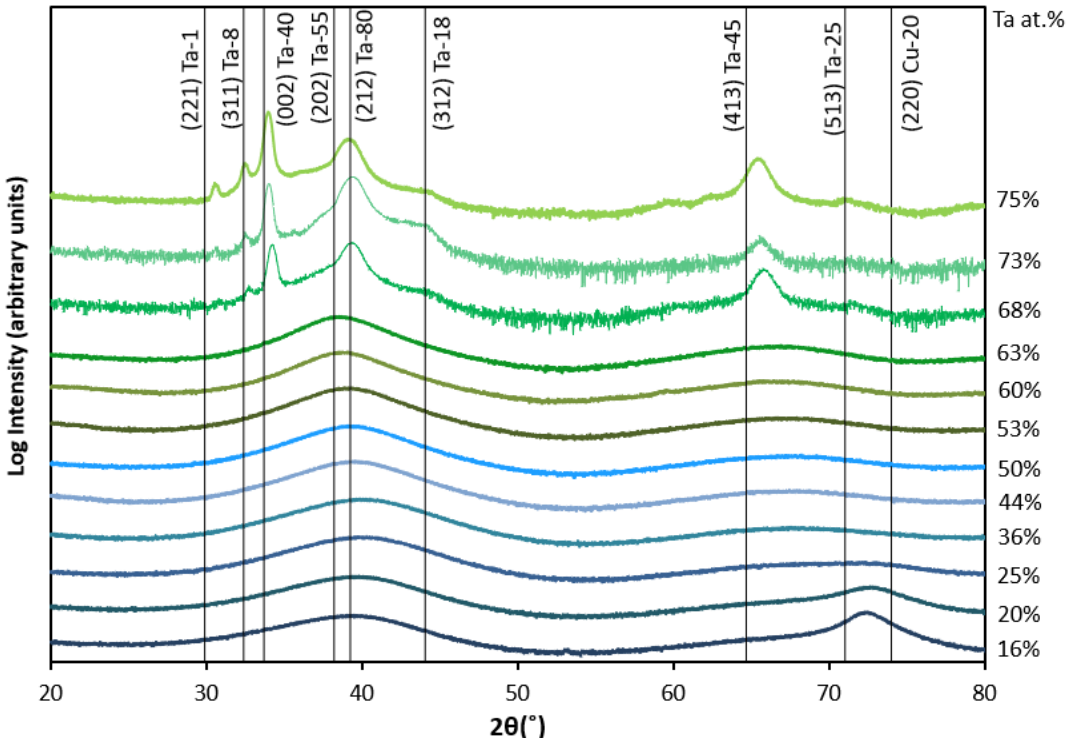

Figure 34. XRD spectra of all monolithic CuTa coatings.

The positive mixing enthalpy of the CuTa system [97] suggests a far-from ideal system in terms of the glass-forming ability. The surprisingly wide range of

compositions with a fully amorphous structure in our case is the result of the magnetron sputtering approach, which provides cooling rates that are orders of magnitude higher than conventional bulk rapid solidification techniques. The glass-forming compositional range of sputtered CuTa was previously reported as 20-60 at.% Ta [97], in close agreement with our findings.

Figure 35 shows the variation of grain size with Ta content, as calculated by the Scherrer equation based on the highest peaks appearing in the XRD pattern of the samples.

In detail, grain sizes are based on Ta (002) peaks around 33.7° for $Cu_{25}Ta_{75}$, Ta (002), and Ta (212) peaks for $Cu_{27}Ta_{73}$ and $Cu_{32}Ta_{68}$. The grain size of Ta, based on Ta (002) peak around 36.2°, the grain size of Cu, based on Cu (111) peak around 43.2°, are also shown for comparison. Grain sizes of pure Cu and Ta are 22 nm and 21 nm, respectively.

The grain sizes of monolithic CuTa samples are in the range of 10 – 20 nm for the films with Ta crystalline peaks (68 – 75 at.% Ta). The grain size abruptly decreases with decreasing Ta content and goes below 2 nm below 63 at.% Ta, suggesting an XRD-amorphous structure to the Ta concentration of 25 at.%. Grain sizes of XRD-amorphous samples (Ta concentration of 25-63 at.%) are based on the humps located around 37 ° in the XRD pattern. The grain sizes of monolithic CuTa samples are in the range of 2 – 5 nm for the films with a small Cu crystalline peak (16 – 20 at.% Ta).

Figure 36 shows the variation of d-spacing (or interatomic spacing for the amorphous samples) with Ta content. The interatomic spacing monotonically increases with increasing Ta content in the amorphous range, and an opposite trend is evident for the d-spacing. d-spacing abruptly increases when Ta concentration increase above 63 at.%, and Ta β-phase crystallites appear in the microstructure.

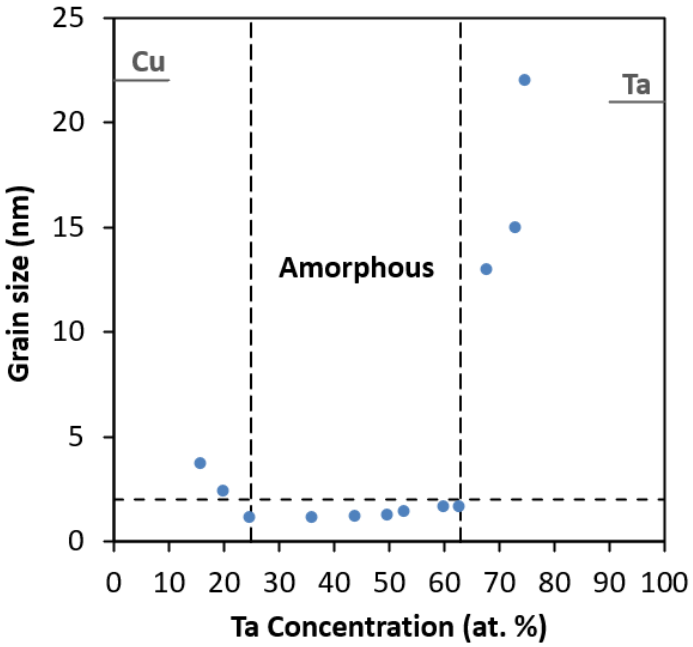

Figure 35. Average grain sizes of monolithic CuTa coatings, as calculated by the Scherrer equation.

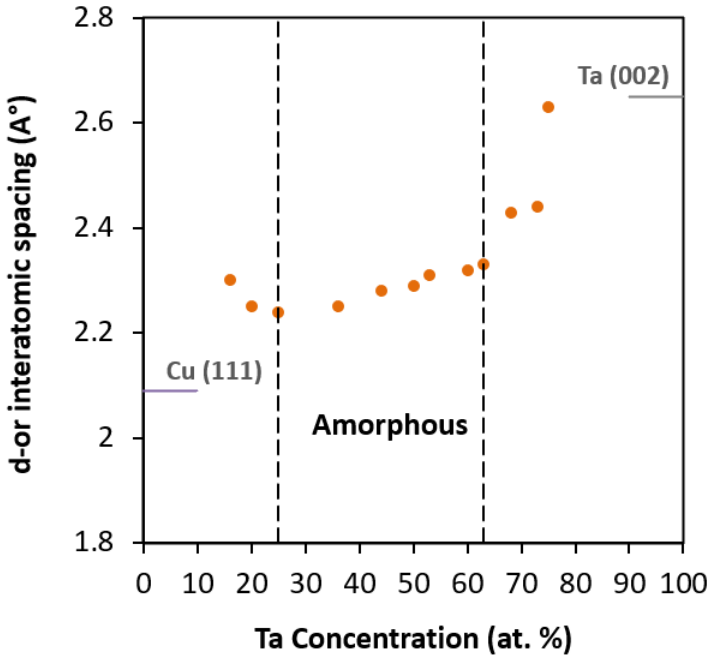

Figure 36. Variation of d-spacing (or average interatomic spacing) with Ta concentration.

Figure 37 shows the XRD spectra of all Amorphous/Amorphous nanolayered CuTa coatings, consisting of alternating layers of $Cu_{75}Ta_{25}$ and $Cu_{40}Ta_{60}$. Three different layer thicknesses were considered, namely, 20 nm, 40 nm, and 100 nm. The figure also shows the XRD results of the corresponding monolithic films for comparison. There is no major difference between the spectra, suggesting that both $Cu_{75}Ta_{25}$ and $Cu_{40}Ta_{60}$ maintain their amorphous structure when confined into a layered morphology. On the other hand, there is a shift of the peaks to lower angles for smaller layer thickness. We attribute this behavior to the variation in the film stress with layer thickness, a commonly observed behavior in nanolayered films [113].

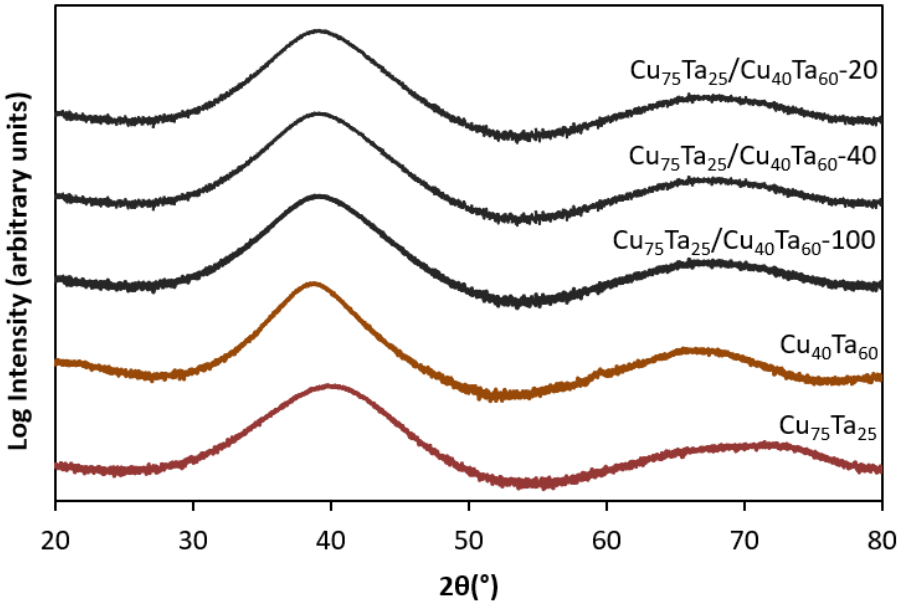

Figure 37. XRD patterns of CuTa amorphous/amorphous nanolayers and their constituents.

Figure 38 shows the XRD spectra of all Amorphous/Semi-crystalline nanolayers (metallic glass-crystalline composite), consisting of alternating layers of $Cu_{75}Ta_{25}$ and $Cu_{25}Ta_{75}$. Three different layer thicknesses were considered, namely, 20 nm, 40 nm, and 100 nm. The figure also shows the XRD results of the corresponding monolithic films for comparison. In the XRD pattern of nanolayers, crystalline peaks corresponding to β-phase tetragonal tantalum are appearing due to the existence of

$Cu_{25}Ta_{75}$ nanocrystalline layer in the nanolayers structures. The highest peak in the nanolayers corresponds to the Ta (212) around 39˚. However, the highest peak in the XRD pattern of the $Cu_{25}Ta_{75}$ monolithic sample corresponds to Ta (002) around 33.7˚. It seems that generally, the intensity of the peaks in nanolayers is lower compared to the $Cu_{25}Ta_{75}$ nanocrystalline sample.

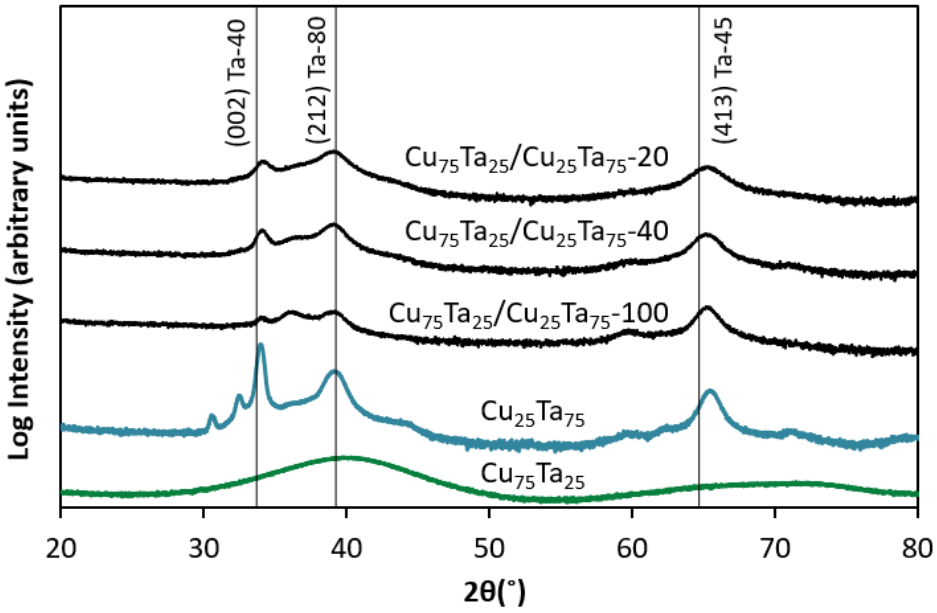

Figure 38. XRD patterns of CuTa amorphous/semi-crystalline nanolayers (metallic glass-crystalline composite) and their constituents.

Table 3 represents the grain size values of Amorphous/Semi-crystalline CuTa nanolayers. The grain sizes of these metallic glass-crystalline composites are calculated using the Scherrer formula. Results correspond to the highest peak in their XRD pattern, which is Ta (212). The grain size decreases with decreasing layer thickness, and it varies from 3.5 nm to 5 nm. Comparing grain size of the monolithic $Cu_{25}ta_{75}$ (19 nm) with that of these nanolayers shows that the fabrication of nanolayers consisting of alternating semi-crystalline (with relatively larger grain size) and amorphous (with grain size below 2 nm) layers leads to get samples with interestingly smaller grain size compared to their nanocrystalline constituent.

Table 3. Average grain sizes of Amorphous/Semi-crystalline CuTa nanolayers, as calculated by the Scherrer equation.

Sample Name	Grain size (nm)
$Cu_{75}Ta_{25}$ / $Cu_{25}Ta_{75}$ - 100	5
$Cu_{75}Ta_{25}$ / $Cu_{25}Ta_{75}$ - 40	4.5
$Cu_{75}Ta_{25}$ / $Cu_{25}Ta_{75}$ - 20	3.5

4.3.2 Hardness and Elastic Modulus

Figure 39 (a) shows the hardness and elastic modulus of pure Ta and pure Cu films, as well as those of monolithic CuTa films as a function of Ta concentration. Pure Ta and Cu have hardness values of 19.15 GPa, and 2.2 GPa, respectively. The hardness of the CuTa films exhibits a considerable variation in the range of ~ 6 – 17 GPa. The hardness monotonically increases with increasing Ta concentration, and this increasing trend becomes more pronounced for 63 at.% Ta and higher. Elastic modulus data are shown in Figure 39 (b), which has a similar increasing trend with Ta concentration.

The ROM-based hardness predictions depicted in Figure 39 (a) and (b) are in good match with experimentally determined values. In the case of hardness, experimental values are very close to the prediction values calculated based on the Voigt model. However, these values become divergent for the samples with Ta concentration above 63 at. %. For elastic modulus, experimental values are very close to the prediction values calculated based on the Reuss model. However, same as what we mentioned for the hardness trend, these values become divergent for the samples with Ta concentration above 63 at. %.

The amorphization-induced hardening is primarily due to eliminating the defects and dislocations from the structure, which are responsible for yielding at a small fraction

of the theoretical strength for crystalline metals. However, in nanocrystalline Ta, the limited number of slip planes, the high binding energies, and the contribution of Hall-Petch strengthening give rise to a hardness of ~17.5 GPa [97], approaching its theoretical strength. As a result, the advantage of amorphization in the context of hardening diminishes.

One of the interesting features of the data is the significant increase in the slope of hardness for concentrations of about 63 at.% Ta and higher. This transition in hardness matches with the onset of crystallization (see Figure 34). Therefore, we propose that the increasing presence of the β-Ta phase with outstanding hardness causes this behavior [115,119].

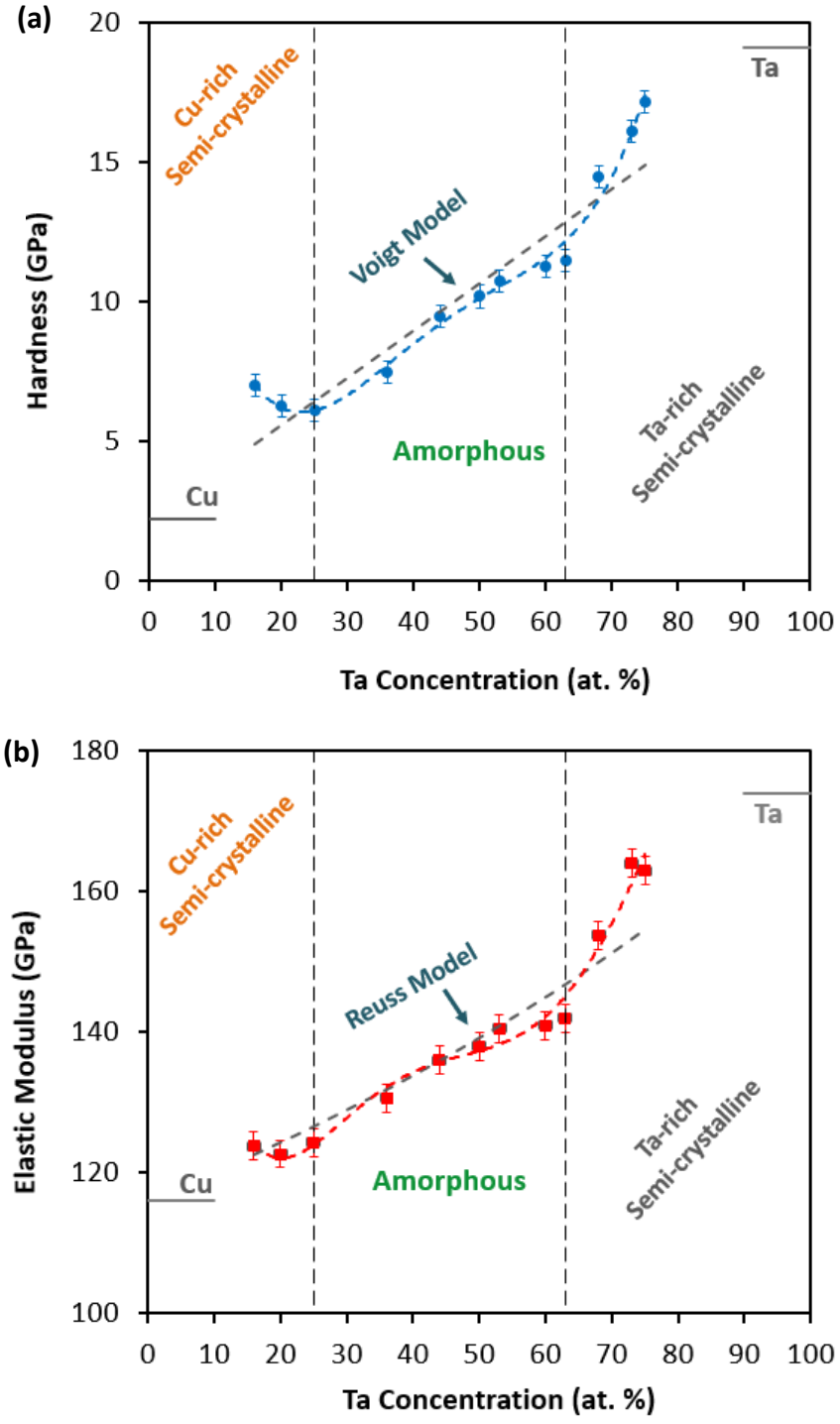

Figure 39. (a) Variation of hardness with Ta concentration. Experimental data and Voigt-type rule of mixture predictions are shown. (b) Variation of elastic modulus with Ta concentration and elastic modulus values calculated by the Reuss-type rule of mixture model.

Figure 40 (a) summarizes the hardness results of the Amorphous/Amorphous nanolayered samples and their constituent monolithics. The hardness of the nanolayered films is about 8.5 GPa. The hardness difference between nanolayers with different layer thicknesses is comparable to the standard deviation of the data, suggesting that nanolayers' hardness does not change with layer thickness.

The first observation is that the ~8.5 GPa hardness of the nanolayers is somehow equal to the average of their constituents' hardness. This is an expected result as 50% of the composite volume is occupied by $Cu_{40}Ta_{60,}$ and the other 50% is occupied by $Cu_{75}Ta_{25}$.

The second important observation is the layer-thickness independent hardness of the nanolayers. This behavior is in agreement with the size-independent strength of MGs in general, as demonstrated by micropillar measurements over a wide range of sizes [123]. Literature data on amorphous-amorphous [124] nanolayers exhibit a similar trend. The same is observed in crystalline-amorphous nanolayered films [93] when the amorphous layer is softer than the crystalline counterpart. This size-independent behavior is in stark contrast to the crystalline metals that exhibit grain size [125] and layer thickness-dependent [122] hardness.

When it comes to the elastic modulus data represented in Figure 40 (b), the trends suggest that a ROM approach can predict the behavior of the nanolayered films. This is an expected outcome, as elastic modulus response in a layered system is analogous to a system of springs in series.

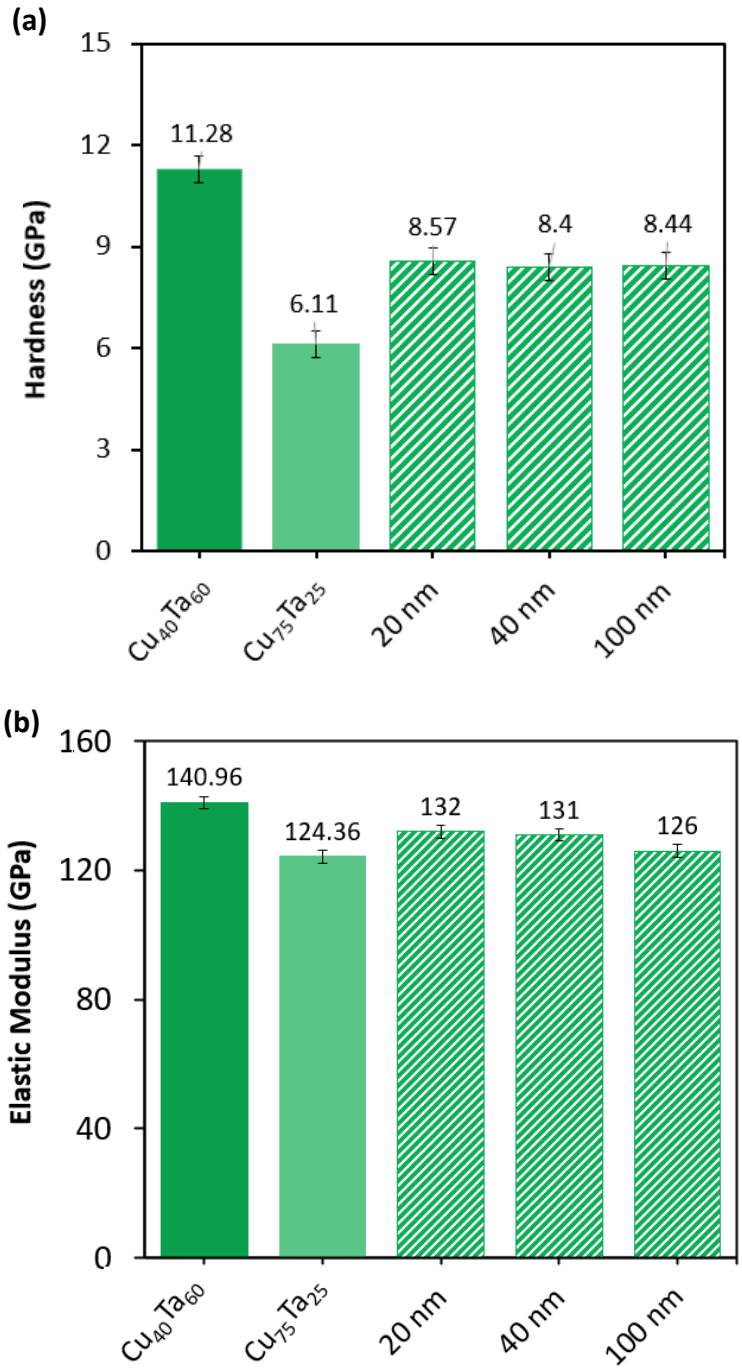

Figure 40. (a) The hardness of monolithic $Cu_{40}Ta_{60}$, $Cu_{75}Ta_{25}$, and nanolayered $Cu_{75}Ta_{25}/Cu_{40}Ta_{60}$ films with different layer thicknesses. (b) shows the same for elastic modulus.

Figure 41(a) summarizes the hardness results of the Amorphous/semi-crystalline nanolayered samples and their constituent monolithic samples. The hardness of the nanolayered films is about 11.7 GPa for films with 20nm and 40nm layer thicknesses. The nanolayered sample with 100nm layer thickness has lower hardness compared to other nanolayers.

The first observation is that the hardness of the nanolayers is somehow equal to the average of their constituents' hardness. This is an expected result as 50% of the composite volume is occupied by $Cu_{25}Ta_{75,}$ and the other 50% is occupied by $Cu_{75}Ta_{25}$.

The second important observation is the layer-thickness independent hardness of the nanolayers in samples containing layers with thickness of 20nm and 40nm. This behavior is in agreement with the size-independent strength of MGs in general, as demonstrated by micropillar measurements over a wide range of sizes [123]. Literature data on amorphous-amorphous [124] nanolayers exhibit a similar trend.

When it comes to the elastic modulus data represented in Figure 41 (b), the trends suggest that a ROM approach can predict the behavior of the nanolayered films. This is an expected outcome, as elastic modulus response in a layered system is analogous to a system of springs in series.

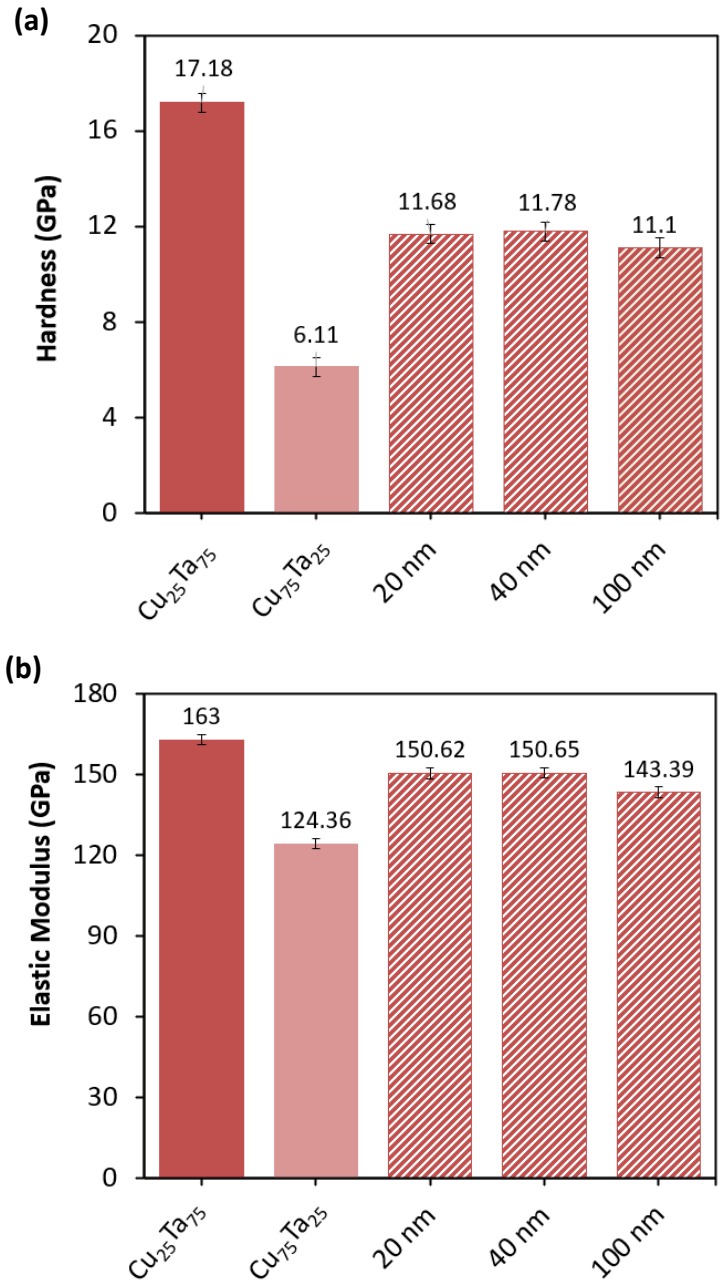

Figure 41. (a) The hardness of monolithic $Cu_{25}Ta_{75}$, $Cu_{75}Ta_{25}$, and nanolayered $Cu_{75}Ta_{25}/Cu_{25}Ta_{75}$films with different layer thicknesses. (b) shows the same for elastic modulus.

4.3.3 Ductility and Fracture Toughness

In order to analyze ductility and fracture toughness of CuTa samples, three monolithic samples, namely $Cu_{84}Ta_{16}$ (Cu-rich semi-crystalline), $Cu_{50}Ta_{50}$ (Amorphous), $Cu_{25}Ta_{75}$ (Ta-rich semi-crystalline), and two nanolayers, $Cu_{75}Ta_{25}/Cu_{40}Ta_{60}$-20 and $Cu_{75}Ta_{25}/Cu_{25}Ta_{75}$-20 samples are selected. These films were deposited on polyimide and SiO2 at the same time. After performing a tensile test on selected samples, ductility and fracture toughness are measured as described in section 2.3.2.1. Moreover, we employed an energy-based method proposed by Chen [68], based on the concept of irreversible work in load-displacement curves of cube corner indentations (section 2.3.1.2.2) to compare fracture toughness values determined in both indentation-based and tensile test-based approaches.

Figure 42 shows electrical resistance change versus strain for $Cu_{84}Ta_{16}$, $Cu_{50}Ta_{50}$, $Cu_{25}Ta_{75}$, $Cu_{75}Ta_{25}/Cu_{40}Ta_{60}$-20 and $Cu_{75}Ta_{25}/Cu_{25}Ta_{75}$-20 samples during tensile test. Through using these curves, critical resistance (ε_c) for nucleating microcracks of the samples can be determined. In these curves, two different regions could be seen. In the first region, the films deform elastically. Despite there are small changes in electrical resistance because of lengthening and decrease in cross-section, it has a linear change up to the specific strain. This linear change can be calculated accurately through taking derivatives from every two adjacent points. This linear increase is because of not existing damage and microcracks in samples up to a certain strain. By increasing strain more and more, damage induces in the sample, and the microcracks propagate, which leads to a significant increase in electrical resistance and the presence of a second region (nonlinear) in the curves. The critical strain is defined as a strain in which the curves transform from linear region to second nonlinear region. To sum up critical strain of all the samples are calculated through taking derivatives of two adjacent points on the curves and detect the slope changes. According to the Figure 42 critical strain is approximately equal to 1.68 %, 1.32%, 1.53%, 2.12% and 2.65% for $Cu_{84}Ta_{16}$, $Cu_{50}Ta_{50}$, $Cu_{25}Ta_{75}$, $Cu_{75}Ta_{25}/Cu_{40}Ta_{60}$-20 and $Cu_{75}Ta_{25}/Cu_{25}Ta_{75}$-20 samples respectively. Critical strain can provide some

information about the samples. Firstly, it can provide information about the ductility of the samples. A higher critical strain means higher plastic deformation and ductility. $Cu_{75}Ta_{25}/Cu_{25}Ta_{75}$-20 nanolayered sample has the highest critical strain, and $Cu_{50}Ta_{50}$ has the lowest critical strain between the samples. Second, through finding critical strain, fracture stress (σ_f) of the samples could be determined.

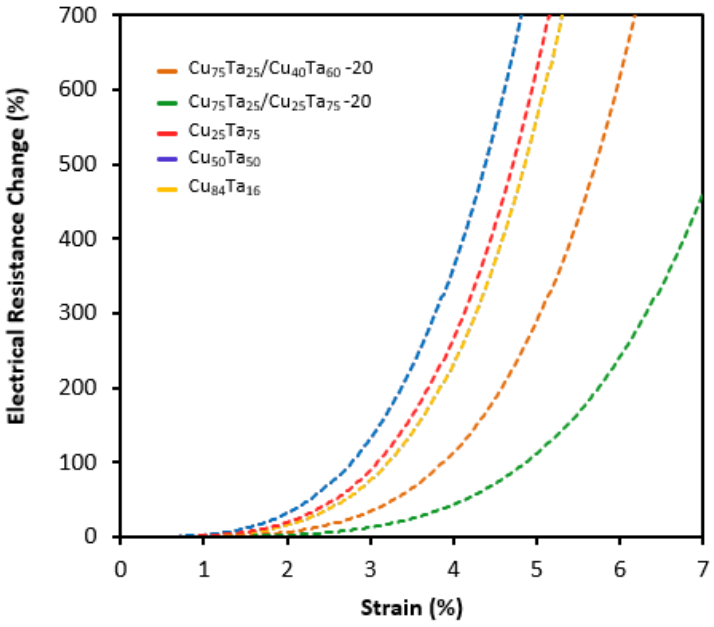

Figure 42. Electrical resistance versus strain for $Cu_{84}Ta_{16}$, $Cu_{50}Ta_{50}$, $Cu_{25}Ta_{75}$, $Cu_{75}Ta_{25}/Cu_{40}Ta_{60}$-20 and $Cu_{75}Ta_{25}/Cu_{25}Ta_{75}$-20 samples.

Figure 43 indicates stress-strain curves for the same samples. Arrows indicate the previously determined critical strain for each sample on the corresponding curve. As it is obvious in the inset of Figure 43 according to stress-strain curves of all monolithic samples, stress is increasing with strain up to a specific strain for each sample, and after reaching the maximum stress, it decreases severely, especially in the case of the $Cu_{50}Ta_{50}$ sample which is a fully amorphous sample, and this behavior is due to its high brittleness. For the other two monolithic samples, due to the existence of Cu and Ta crystalline phases respectively in $Cu_{84}Ta_{16}$ and $Cu_{25}Ta_{75}$ samples (See Figure 34), after maximum stress, the slope of decrease in stress with

respect to strain is smaller. $Cu_{50}Ta_{50}$ sample has the lowest ductility between the monolithic samples, and the $Cu_{84}Ta_{16}$ sample has the highest ductility among them. To sum up, for all the monolithic samples, stress reaches the maximum point at critical strain approximately, and after the critical strain, stress relaxation happens due to shear band and crack formation.

In nanolayered samples, stress increases with respect to strain up to the maximum point, and after that, the slope of decrease in stress with respect to strain is smaller compared to monolithic samples. Moreover, these nanolayered samples possess higher ductility compared to monolithic samples. This result can be due to the suitable structural and property modulation in samples and heterogeneity increase which causes samples to experience more plastic deformation and late fracture. In other words, the critical strain occurs after plastic deformation, while in monolithic samples, it occurs in the elastic deformation region. In this line of thought, fracture toughness measurements may give us a sight to understand more about these outcomes.

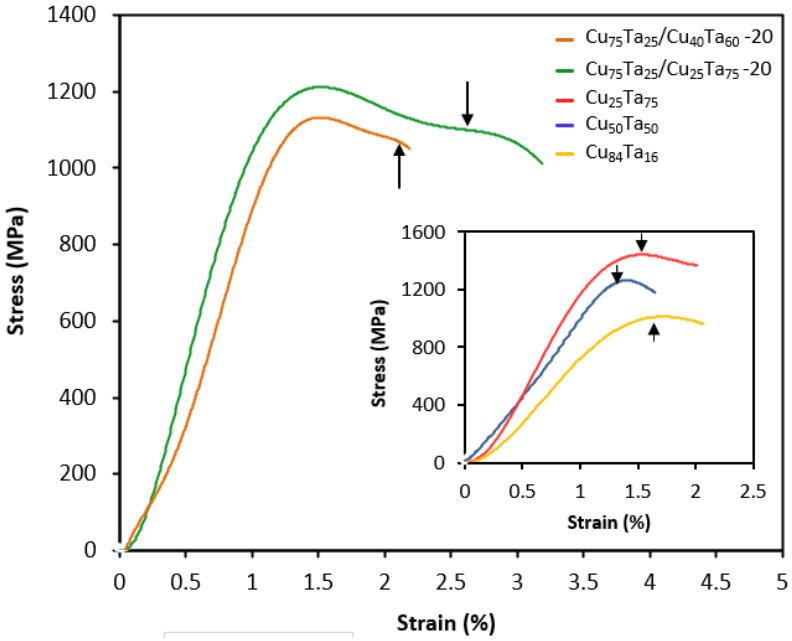

Figure 43. Stress-strain curves of $Cu_{84}Ta_{16}$, $Cu_{50}Ta_{50}$, $Cu_{25}Ta_{75}$, $Cu_{75}Ta_{25}/Cu_{40}Ta_{60}$-20 and $Cu_{75}Ta_{25}/Cu_{25}Ta_{75}$-20 samples. The arrows indicate the critical strain.

Table 4 shows the mechanical properties of $Cu_{84}Ta_{16}$, $Cu_{50}Ta_{50}$, $Cu_{25}Ta_{75}$, $Cu_{75}Ta_{25}/Cu_{40}Ta_{60}$-20, and $Cu_{75}Ta_{25}/Cu_{25}Ta_{75}$-20 samples extracted directly from stress-strain curves and electrical resistance measurements. Among monolithic samples, elastic modulus and fracture stress increase with Ta concentration in the samples. In the case of critical strain, Cu-rich semi-crystalline ($Cu_{84}Ta_{16}$) and Ta-rich semi-crystalline ($Cu_{25}Ta_{75}$) have larger critical strain than full amorphous $Cu_{50}Ta_{50}$. In the case of nanolayered samples, $Cu_{75}Ta_{25}/Cu_{25}Ta_{75}$-20 has a larger elastic modulus, critical strain, and fracture stress compared to $Cu_{75}Ta_{25}/Cu_{40}Ta_{60}$-20. Higher ductility of, $Cu_{75}Ta_{25}/Cu_{25}Ta_{75}$-20 sample with respect to $Cu_{75}Ta_{25}/Cu_{40}Ta_{60}$-20 is probably due to the existence of a semi-crystalline $Cu_{25}Ta_{75}$ layer in the system. Furthermore, having in mind that the only difference in these two nanolayered samples is replacing $Cu_{25}Ta_{75}$ semi-crystalline layer instead of full amorphous $Cu_{40}Ta_{60}$ layer, it can be concluded that $Cu_{25}Ta_{75}$ which has the highest fracture stress among the samples, causes $Cu_{75}Ta_{25}/Cu_{25}Ta_{75}$-20 sample to has higher fracture stress compared to full amorphous $Cu_{75}Ta_{25}/Cu_{40}Ta_{60}$-20 nanolayered sample. Comparing two $Cu_{50}Ta_{50}$ and $Cu_{75}Ta_{25}/Cu_{40}Ta_{60}$-20 amorphous samples, the nanolayered sample has 60% higher ductility than the monolithic sample. Comparing $Cu_{25}Ta_{75}$ and $Cu_{75}Ta_{25}/Cu_{25}Ta_{75}$-20 samples in terms of ductility shows that introducing an amorphous $Cu_{75}Ta_{25}$ layer and fabrication of nanolayered sample caused approximately 73% increase in ductility and its due to enhancement in heterogeneity and interlayer area in the system and results in stretchability of nanolayered sample. It seems that the amorphous $Cu_{75}Ta_{25}$ layer acts as an obstacle against shear banding and crack propagation. The same behavior is reported in previous studies when Cu crystalline layer is introduced to the amorphous system [56].

Table 4. Mechanical properties of $Cu_{84}Ta_{16}$, $Cu_{50}Ta_{50}$, $Cu_{25}Ta_{75}$, $Cu_{75}Ta_{25}/Cu_{40}Ta_{60}$-20 and $Cu_{75}Ta_{25}/Cu_{25}Ta_{75}$-20 samples extracted from stress-strain curves.

Samples	***E* (GPa)**	**ε_c (%)**	**σ_f (MPa)**
$Cu_{84}Ta_{16}$	86.2±2.9	1.68±0.07	1004.25±10.7
$Cu_{50}Ta_{50}$	102.9±2.5	1.32±0.05	1251.4±8.4
$Cu_{25}Ta_{75}$	126.4±2.9	1.53±0.01	1429.05±15.4
$Cu_{75}Ta_{25}/Cu_{40}Ta_{60}$-20	108.8±4.7	2.12±0.15	1053.28±5.8
$Cu_{75}Ta_{25}/Cu_{25}Ta_{75}$-20	120.6±3.7	2.65±0.26	1089.83±12.6

Table 5 shows the comparison of fracture toughness values calculated using both tensile test and indentation-based methods for $Cu_{50}Ta_{50}$, $Cu_{25}Ta_{75}$, $Cu_{75}Ta_{25}/Cu_{40}Ta_{60}$-20, and $Cu_{75}Ta_{25}/Cu_{25}Ta_{75}$-20 samples. In the case of fracture toughness calculation through the tensile test, $Cu_{25}Ta_{75}$ has the highest fracture toughness among samples, while nanolayered samples possess the lowest toughness. The high toughness of the monolithic $Cu_{25}Ta_{75}$ sample is due to the high concentration of Ta in this sample. It seems in the case of tensile test, fabrication of nanolayers does not increase fracture toughness, and it depends mostly on overall Ta concentration in the samples. In the case of the indentation test, again, $Cu_{25}Ta_{75}$ has the highest fracture toughness, and $Cu_{75}Ta_{25}/Cu_{40}Ta_{60}$-20 sample possesses the lowest fracture toughness value. $Cu_{75}Ta_{25}/Cu_{25}Ta_{75}$-20 sample has a high fracture toughness of 5.06 $MPa.m^{1/2}$ compared to $Cu_{75}Ta_{25}/Cu_{25}Ta_{75}$-20 and $Cu_{50}Ta_{50}$ samples. It seems in the case of nanoindentation, because of different deformation modes compared to tensile test, the fabrication of $Cu_{75}Ta_{25}$ and $Cu_{25}Ta_{75}$ nanolayers on top of each other leads to enhanced fracture toughness. Comparing the values of fracture toughness resulted from two different techniques for each sample indicates that in the case of amorphous samples ($Cu_{50}Ta_{50}$ and $Cu_{75}Ta_{25}/Cu_{40}Ta_{60}$-20), both results are close to each other. But when it comes to $Cu_{25}Ta_{75}$ and $Cu_{75}Ta_{25}/Cu_{25}Ta_{75}$-

20 samples, there is a relatively big difference between the values resulted from indentation-based and tensile test-based methods. In the case of the $Cu_{75}Ta_{25}/Cu_{40}Ta_{60}$-20 sample, it seems that the effect of modulation of heterogeneity is somehow lost; however, it is shown that it has relatively higher ductility. To sum up, $Cu_{75}Ta_{25}/Cu_{25}Ta_{75}$-20 has a high fracture toughness together with high ductility (Table 4), and in both deformation modes, it indicates relatively desired properties.

Table 5. Comparison of fracture toughness values calculated using both tensile test and indentation-based methods for $Cu_{50}Ta_{50}$, $Cu_{25}Ta_{75}$, $Cu_{75}Ta_{25}/Cu_{40}Ta_{60}$-20 and $Cu_{75}Ta_{25}/Cu_{25}Ta_{75}$-20 samples.

Samples	K_c **(MPa.m$^{1/2}$)**	
	Tensile test-based energy method	**Indentation-based energy method**
$Cu_{50}Ta_{50}$	3.92±0.03	4.24±0.13
$Cu_{25}Ta_{75}$	4.56±0.05	6.8±0.25
$Cu_{75}Ta_{25}/Cu_{40}Ta_{60}$-20	3.37±0.02	3.91±0.06
$Cu_{75}Ta_{25}/Cu_{25}Ta_{75}$-20	3.48±0.04	5.06±0.1

Figure 44 indicates microscopic images of tensile specimens after the tensile test. İn some images, straight lines are added to better show the cracks. In the case of monolithic samples number of cracks in the equal area of the samples is different. Measuring the distance between cracks in monolithic samples shows that the distance between the cracks in $Cu_{84}Ta_{16}$, $Cu_{50}Ta_{50,}$ and $Cu_{25}Ta_{75}$ is 157.3, 59.37, and 65.9 μm on average, respectively. $Cu_{84}Ta_{16}$ has the largest distance between cracks among samples. Distance between cracks in $Cu_{50}Ta_{50}$ has the lowest value in average, and it indicates that the density of cracks is higher in this sample compared to other monolithic samples validating the lower ductility of this sample. In the case of nanolayered samples, the distance between cracks is 91.2 and 148.17 μm for

$Cu_{75}Ta_{25}$/$Cu_{40}Ta_{60}$-20 and $Cu_{75}Ta_{25}$/$Cu_{75}Ta_{25}$-20, respectively. To conclude, obviously, there exists a relation between ductility (critical strain) and crack distancing (or crack density) in our samples, in a way that the samples which illustrate higher ductility have lesser crack density. This conclusion seems to be suitable for all the samples in this study except $Cu_{84}Ta_{16}$ which has the largest crack spacing but not high ductility compared to nanolayered samples.

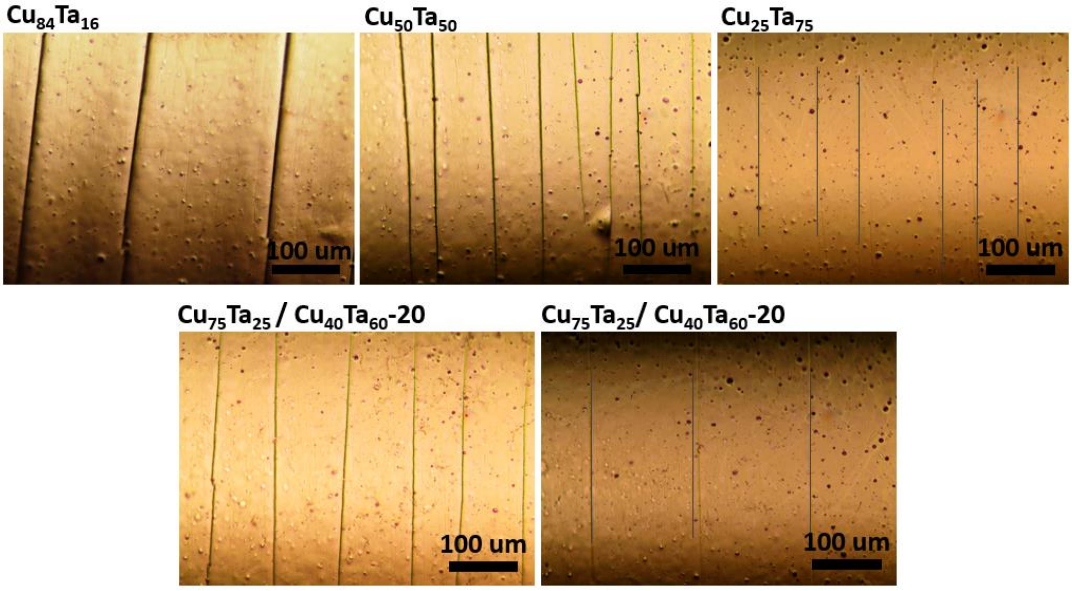

Figure 44. Microscopic images of tensile specimens after tensile test.

4.4 Conclusions

The study investigated the structure-property relationships in the CuTa system. The microstructural transition from a fully amorphous alloy to an amorphous-crystalline composite has a significant impact on the mechanical properties. Specifically, the semi-crystalline $Cu_{25}Ta_{75}$ combines high hardness with improved fracture toughness due to the unique combination of a hard crystalline phase and a softer amorphous matrix.

The metallic glass-crystalline nanolayered CuTa films with modulated composition demonstrated a balanced combination of hardness and ductility. Therefore, the nanolayered MG-Crystalline concept provides a new and effective route to the development of tough coatings with optimized strength and ductility. Furthermore, in the case of nanolayers, structural modulation resulted in a ductility increase, but fracture toughness was not improved based on the tensile test. However, indentation results for fracture toughness measurements are different, and the amorphous/semi-crystalline sample shows high fracture toughness. To conclude, we can say that the amorphous/semi-crystalline system in this study has a variety of desired properties like high tensile ductility, toughness, hardness, elastic modulus, and at the same time, small grain size, which makes it an optimum sample among the samples investigated in this study.

CONCLUSIONS AND FUTURE WORK

The study investigated the structure-property relationships in the ZrTa and CuTa systems. In the ZrTa study, it was noticed that the microstructural transition from a fully amorphous alloy to an amorphous-crystalline composite has a significant impact on the mechanical properties.

The fully amorphous ZrTa films with modulated composition demonstrated a balanced combination of hardness and ductility and provided an improvement over MG films with homogeneous composition. Therefore, the nanolayered MG concept provides a new and effective route to the development of heterogeneous MG coatings with optimized strength and ductility.

Table 6 contains the mechanical properties of $Zr_{21}Ta_{79}$, $Zr_{25}Ta_{75}$, $Zr_{50}Ta_{50,}$ and $Zr_{35}Ta_{65/}Zr_{70}Ta_{30}$ – 10 from ZrTa study. As it is obvious in terms of hardness, elastic modulus, and toughness, $Zr_{21}Ta_{79}$ and $Zr_{25}Ta_{75}$ MG-crystalline composite is a superior material in this study. In other words, the semi-crystalline $Z_{r21}Ta_{79}$ combines high hardness with improved fracture toughness due to the unique combination of a hard crystalline phase and a softer amorphous matrix. However, as it is discussed in Chapter 3, this kind of composites may sacrifice some advantages of fully amorphous alloys such as corrosion resistance, so in this regard, the fully amorphous ZrTa nanolayers with modulated composition ($Zr_{35}Ta_{65/}Zr_{70}Ta_{30}$ – 10) not only has advantage over MG-crystalline composite but also can provide an improvement over MG films with homogeneous composition.

To conclude, ZrTa MG-crystalline and MG/MG nanolayered composites are optimum coatings depending on the application area.

In the CuTa study, it was noticed that a wide compositional range of amorphous CuTa binary alloys is acquired, and as a result, an extensive range of hardness and elastic modulus is found in CuTa samples with different compositions. Furthermore, the microstructural transition from a fully amorphous alloy to an amorphous-

crystalline composite shows a significant impact on the mechanical properties too. Specifically, the semi-crystalline $Cu_{25}Ta_{75}$ combines high hardness with improved fracture toughness due to the unique combination of a hard crystalline phase and a softer amorphous matrix.

Table 6 also includes mechanical properties of $Cu_{25}Ta_{75}$, $Cu_{50}Ta_{50}$, $Cu_{75}Ta_{25}/Cu_{40}Ta_{60}$ – 20 and $Cu_{75}Ta_{25}/Cu_{75}Ta_{25}$ - 20 from CuTa study. In terms of hardness and elastic modulus, $Cu_{25}Ta_{75}$ and $Cu_{75}Ta_{25}/Cu_{75}Ta_{25}$ - 20 MG-crystalline composites have an advantage over other samples. Having these two samples in mind and investigating their toughness and ductility results, it can be realized that they possess high toughness values in the case of indentation. However, when it comes to the tensile test, the fracture toughness values are smaller. We attribute this behavior to the difference in deformation mode and deformation direction in tensile and indentation tests. In terms of ductility, nanolayered $Cu_{75}Ta_{25}/Cu_{75}Ta_{25}$ – 20 is more ductile than $Cu_{25}Ta_{75}$, and it seems that adding a soft amorphous layer to the system behaves such an obstacle to crack propagation and brittle fracture.

Considering $Cu_{50}Ta_{50}$ and $Cu_{75}Ta_{25}/Cu_{40}Ta_{60}$ – 20 full MG sample, fracture toughness is not improved in $Cu_{75}Ta_{25}/Cu_{40}Ta_{60}$ – 20 nanolayered sample, and somehow modulation of composition in MG/MG nanolayers couldn't enhance the fracture toughness. But when it comes to ductility, MG/MG nanolayer possess higher ductility compared to $Cu_{50}Ta_{50}$.

It seems that modulated composition in MG/MG nanolayers affected on the improvement of ductility but not on the enhancement of fracture toughness.

To sum up, both full amorphous and amorphous-crystalline samples are better and optimum materials in case of ductility.

As future work, this study gives an idea of measuring ductility of different alloys using an in-situ tensile test which gives us an opportunity to monitor the crack propagation step by step at each strain. Moreover, using different methods of machining, micro, and nano-scale tensile specimens can be produced on any kind

of substrates to perform the tensile test. In this vein, finite element simulations can be helpful to validate the ductility and toughness data derived from the tensile and indentation experiments.

As we found in the result of tensile experiments, crystallization in the monolithic samples did not affect the ductility as expected, but in the case of nanolayers, ductility enhanced considerably. So, it can be a good idea to study the correlation of crystallization and fracture toughness in metallic thin films especially considering two monolithic and multilayer systems. This way, it is also possible to extract the real effect of nanolayer fabrication on the ductility and toughness of the samples.

As the next step of this study, one can also investigate the change in the microstructure of the samples after the tensile test. As a result of such a study, useful findings can be achieved about the structural stability in different types of microstructures.

Table 6. Mechanical properties of selected samples in ZrTa and CuTa studies.

Sample	Description	*H* (GPa)	*E* (GPa)	K_c (MPa.m$^{1/2}$)		Ductility (%)
				Indentation	Tensile test	
$Zr_{21}Ta_{79}$	Ta-ich MG-crystalline composite	12.45	130.37	5.86	-	-
$Zr_{25}Ta_{75}$	Ta-rich MG-crystalline composite	10.4	128.64	4.43	-	-
$Zr_{50}Ta_{50}$	Full Amorphous	7.56	116.24	2.9	-	-
$Zr_{35}Ta_{65}/Zr_{70}Ta_{30}$ - 10	MG/MG nanolayered	8.52	118.91	4.27	-	-
$Cu_{25}Ta_{75}$	Ta-rich MG-crystalline composite	17.18	163	6.8	4.56	1.53
$Cu_{50}Ta_{50}$	Full Amorphous	10.2	138	4.24	3.92	1.32
$Cu_{75}Ta_{25}/Cu_{40}Ta_{60}$ - 20	MG/MG nanolayered	8.57	132	3.91	3.37	2.12
$Cu_{75}Ta_{25}/Cu_{25}Ta_{75}$- 20	MG/Semi-crystalline nanolayered	11.68	150.62	5.06	3.48	2.65

REFERENCES

[1] M.F. Ashby, A.L. Greer, Metallic glasses as structural materials, Scripta Materialia. 54 (2006) 321–326. https://doi.org/10.1016/j.scriptamat.2005.09.051.

[2] J. Schroers, G. Kumar, T.M. Hodges, S. Chan, T.R. Kyriakides, Bulk metallic glasses for biomedical applications, JOM. 61 (2009) 21–29. https://doi.org/10.1007/s11837-009-0128-1.

[3] M.M. Trexler, N.N. Thadhani, Mechanical properties of bulk metallic glasses, Progress in Materials Science. 55 (2010) 759–839. https://doi.org/10.1016/j.pmatsci.2010.04.002.

[4] W.H. Wang, C. Dong, C.H. Shek, Bulk metallic glasses, Materials Science and Engineering: R: Reports. 44 (2004) 45–89. https://doi.org/10.1016/j.mser.2004.03.001.

[5] A. Takeuchi, A. Inoue, Classification of Bulk Metallic Glasses by Atomic Size Difference, Heat of Mixing and Period of Constituent Elements and Its Application to Characterization of the Main Alloying Element, Materials Transactions. 46 (2005) 2817–2829. https://doi.org/10.2320/matertrans.46.2817.

[6] J.P. Chu, J.S.C. Jang, J.C. Huang, H.S. Chou, Y. Yang, J.C. Ye, Y.C. Wang, J.W. Lee, F.X. Liu, P.K. Liaw, Y.C. Chen, C.M. Lee, C.L. Li, C. Rullyani, Thin film metallic glasses: Unique properties and potential applications, Thin Solid Films. 520 (2012) 5097–5122. https://doi.org/10.1016/j.tsf.2012.03.092.

[7] P. Yiu, W. Diyatmika, N. Bönninghoff, Y.-C. Lu, B.-Z. Lai, J.P. Chu, Thin film metallic glasses: Properties, applications and future, Journal of Applied Physics. 127 (2020) 030901. https://doi.org/10.1063/1.5122884.

[8] J. Schroers, Q. Pham, A. Desai, Thermoplastic Forming of Bulk Metallic Glass— A Technology for MEMS and Microstructure Fabrication, J. Microelectromech. Syst. 16 (2007) 240–247. https://doi.org/10.1109/JMEMS.0007.892889.

[9] J. Langer, Shear-transformation-zone theory of deformation in metallic glasses, Scripta Materialia. 54 (2006) 375–379. https://doi.org/10.1016/j.scriptamat.2005.10.005.

[10] D.C. Hofmann, J.-Y. Suh, A. Wiest, G. Duan, M.-L. Lind, M.D. Demetriou, W.L. Johnson, Designing metallic glass matrix composites with high toughness and tensile ductility, Nature. 451 (2008) 1085–1089. https://doi.org/10.1038/nature06598.

[11] B.P. Sahu, C.K. Sarangi, R. Mitra, Effect of Zr content on structure property relations of Ni-Zr alloy thin films with mixed nanocrystalline and amorphous structure, Thin Solid Films. 660 (2018) 31–45. https://doi.org/10.1016/j.tsf.2018.05.050.

[12] H.S. Chou, J.C. Huang, Y.H. Lai, L.W. Chang, X.H. Du, J.P. Chu, T.G. Nieh, Amorphous and nanocrystalline sputtered Mg–Cu thin films, Journal of

Alloys and Compounds. 483 (2009) 341–345. https://doi.org/10.1016/j.jallcom.2008.07.187.
[13] E. Ma, J. Ding, Tailoring structural inhomogeneities in metallic glasses to enable tensile ductility at room temperature, Materials Today. 19 (2016) 568–579. https://doi.org/10.1016/j.mattod.2016.04.001.
[14] N. Wang, J. Ding, F. Yan, M. Asta, R.O. Ritchie, L. Li, Spatial correlation of elastic heterogeneity tunes the deformation behavior of metallic glasses, Npj Comput Mater. 4 (2018) 19. https://doi.org/10.1038/s41524-018-0077-8.
[15] A. Inoue, A. Takeuchi, Recent development and application products of bulk glassy alloys☆, Acta Materialia. 59 (2011) 2243–2267. https://doi.org/10.1016/j.actamat.2010.11.027.
[16] C. Schuh, T. Hufnagel, U. Ramamurty, Mechanical behavior of amorphous alloys, Acta Materialia. 55 (2007) 4067–4109. https://doi.org/10.1016/j.actamat.2007.01.052.
[17] T. Burgess, M. Ferry, Nanoindentation of metallic glasses, Materials Today. 12 (2009) 24–32. https://doi.org/10.1016/S1369-7021(09)70039-2.
[18] J.C. Ye, J.P. Chu, Y.C. Chen, Q. Wang, Y. Yang, Hardness, yield strength, and plastic flow in thin film metallic-glass, Journal of Applied Physics. 112 (2012) 053516. https://doi.org/10.1063/1.4750028.
[19] A.S. Argon, Mechanisms of inelastic deformation in metallic glasses, Journal of Physics and Chemistry of Solids. 43 (1982) 945–961. https://doi.org/10.1016/0022-3697(82)90111-1.
[20] Z. Li, Z. Huang, F. Sun, X. Li, J. Ma, Forming of metallic glasses: mechanisms and processes, Materials Today Advances. 7 (2020) 100077. https://doi.org/10.1016/j.mtadv.2020.100077.
[21] M. Telford, The case for bulk metallic glass, Materials Today. 7 (2004) 36–43. https://doi.org/10.1016/S1369-7021(04)00124-5.
[22] W. Klement, R.H. Willens, P. Duwez, Non-crystalline Structure in Solidified Gold–Silicon Alloys, Nature. 187 (1960) 869–870. https://doi.org/10.1038/187869b0.
[23] A. Inoue, T. Zhang, T. Masumoto, Zr–Al–Ni Amorphous Alloys with High Glass Transition Temperature and Significant Supercooled Liquid Region, Materials Transactions, JIM. 31 (1990) 177–183. https://doi.org/10.2320/matertrans1989.31.177.
[24] W.L. Johnson, Bulk Glass-Forming Metallic Alloys: Science and Technology, MRS Bulletin. 24 (1999) 42–56. https://doi.org/10.1557/S0883769400053252.
[25] T. Egami, Y. Waseda, Atomic size effect on the formability of metallic glasses, Journal of Non-Crystalline Solids. 64 (1984) 113–134. https://doi.org/10.1016/0022-3093(84)90210-2.
[26] A. Obeydavi, A. Rezaeian, A. Shafyei, P. Kameli, J.-W. Lee, Prediction of amorphous phase formation by thermodynamic and kinetic analysis, a Fe-based thin film metallic glass deposited by direct current magnetron sputtering, Mater. Res. Express. 6 (2019) 096407. https://doi.org/10.1088/2053-1591/ab2bc4.

[27] T.C. Hufnagel, C.A. Schuh, M.L. Falk, Deformation of metallic glasses: Recent developments in theory, simulations, and experiments, Acta Materialia. 109 (2016) 375–393. https://doi.org/10.1016/j.actamat.2016.01.049.
[28] F.X. Liu, F.Q. Yang, Y.F. Gao, W.H. Jiang, Y.F. Guan, P.D. Rack, O. Sergic, P.K. Liaw, Micro-scratch study of a magnetron-sputtered Zr-based metallic-glass film, Surface and Coatings Technology. 203 (2009) 3480–3484. https://doi.org/10.1016/j.surfcoat.2009.05.017.
[29] C.W. Chu, J.S.C. Jang, S.M. Chiu, J.P. Chu, Study of the characteristics and corrosion behavior for the Zr-based metallic glass thin film fabricated by pulse magnetron sputtering process, Thin Solid Films. 517 (2009) 4930–4933.
[30] C.T. Liu, L. Heatherly, J.A. Horton, D.S. Easton, C.A. Carmichael, J.L. Wright, J.H. Schneibel, M.H. Yoo, C.H. Chen, A. Inoue, Test environments and mechanical properties of Zr-base bulk amorphous alloys, Metall and Mat Trans A. 29 (1998) 1811–1820. https://doi.org/10.1007/s11661-998-0004-6.
[31] W.D. Kaplan, The mechanism of crystal deformation, Science. 349 (2015) 1059. https://doi.org/10.1126/science.aac9623.
[32] S.R. Agnew, B.R. Elliott, C.J. Youngdahl, K.J. Hemker, J.R. Weertman, Microstructure and mechanical behavior of nanocrystalline metals, Materials Science and Engineering: A. 285 (2000) 391–396. https://doi.org/10.1016/S0921-5093(00)00669-9.
[33] A.C. Lund, C.A. Schuh, The Mohr–Coulomb criterion from unit shear processes in metallic glass, Intermetallics. 12 (2004) 1159–1165. https://doi.org/10.1016/j.intermet.2004.07.001.
[34] P.E. Donovan, Compressive deformation of amorphous Pd40Ni40P20, Materials Science and Engineering. 98 (1988) 487–490. https://doi.org/10.1016/0025-5416(88)90213-3.
[35] W.J. Wright, R.B. Schwarz, W.D. Nix, Localized heating during serrated plastic flow in bulk metallic glasses, Materials Science and Engineering: A. 319–321 (2001) 229–232. https://doi.org/10.1016/S0921-5093(01)01066-8.
[36] P. Lowhaphandu, S.L. Montgomery, J.J. Lewandowski, Effects of superimposed hydrostatic pressure on flow and fracture of a Zr-Ti-Ni-Cu-Be bulk amorphous alloy, Scripta Materialia. 41 (1999) 19–24.
[37] Z.F. Zhang, J. Eckert, L. Schultz, Difference in compressive and tensile fracture mechanisms of Zr59Cu20Al10Ni8Ti3 bulk metallic glass, Acta Materialia. 51 (2003) 1167–1179. https://doi.org/10.1016/S1359-6454(02)00521-9.
[38] F. Spaepen, A microscopic mechanism for steady state inhomogeneous flow in metallic glasses, Acta Metallurgica. 25 (1977) 407–415. https://doi.org/10.1016/0001-6160(77)90232-2.
[39] A.S. Argon, Plastic deformation in metallic glasses, Acta Metallurgica. 27 (1979) 47–58. https://doi.org/10.1016/0001-6160(79)90055-5.
[40] M.C. Liu, X.H. Du, I.C. Lin, H.J. Pei, J.C. Huang, Superplastic-like deformation in metallic amorphous/crystalline nanolayered micropillars,

Intermetallics. 30 (2012) 30–34. https://doi.org/10.1016/j.intermet.2012.03.037.
[41] Y. Wang, J. Li, A.V. Hamza, T.W. Barbee, Ductile crystalline-amorphous nanolaminates, Proceedings of the National Academy of Sciences. 104 (2007) 11155–11160. https://doi.org/10.1073/pnas.0702344104.
[42] W. Guo, E. Jägle, J. Yao, V. Maier, S. Korte-Kerzel, J.M. Schneider, D. Raabe, Intrinsic and extrinsic size effects in the deformation of amorphous CuZr/nanocrystalline Cu nanolaminates, Acta Materialia. 80 (2014) 94–106. https://doi.org/10.1016/j.actamat.2014.07.027.
[43] M.C. Liu, J.C. Huang, H.S. Chou, Y.H. Lai, C.J. Lee, T.G. Nieh, A nanoscaled underlayer confinement approach for achieving extraordinarily plastic amorphous thin film, Scripta Materialia. 61 (2009) 840–843. https://doi.org/10.1016/j.scriptamat.2009.07.010.
[44] J.A. Kolodziejska, H. Kozachkov, K. Kranjc, A. Hunter, E. Marquis, W.L. Johnson, K.M. Flores, D.C. Hofmann, Towards an understanding of tensile deformation in Ti-based bulk metallic glass matrix composites with BCC dendrites, Sci Rep. 6 (2016) 22563. https://doi.org/10.1038/srep22563.
[45] M. Abboud, A. Motallebzadeh, N. Verma, S. Özerinç, Nanoscratch Behavior of Metallic Glass/Crystalline Nanolayered Composites, JOM. 71 (2019) 593–601. https://doi.org/10.1007/s11837-018-3270-9.
[46] N.A. Mara, D. Bhattacharyya, P. Dickerson, R.G. Hoagland, A. Misra, Deformability of ultrahigh strength 5nm Cu/Nb nanolayered composites, Appl. Phys. Lett. 92 (2008) 231901. https://doi.org/10.1063/1.2938921.
[47] A. Misra, R.G. Hoagland, H. Kung ‡, Thermal stability of self-supported nanolayered Cu/Nb films, Null. 84 (2004) 1021–1028. https://doi.org/10.1080/14786430310001659480.
[48] M.J. Demkowicz, R.G. Hoagland, J.P. Hirth, Interface Structure and Radiation Damage Resistance in Cu-Nb Multilayer Nanocomposites, Phys. Rev. Lett. 100 (2008) 136102. https://doi.org/10.1103/PhysRevLett.100.136102.
[49] J. Wang, Q. Zhou, S. Shao, A. Misra, Strength and plasticity of nanolaminated materials, Null. 5 (2017) 1–19. https://doi.org/10.1080/21663831.2016.1225321.
[50] N. Li, J. Wang, A. Misra, J.Y. Huang, Direct Observations of Confined Layer Slip in Cu/Nb Multilayers, Microscopy and Microanalysis. 18 (2012) 1155–1162. https://doi.org/10.1017/S143192761200133X.
[51] Q.M. Mehran, M.A. Fazal, A.R. Bushroa, S. Rubaiee, A Critical Review on Physical Vapor Deposition Coatings Applied on Different Engine Components, Null. 43 (2018) 158–175. https://doi.org/10.1080/10408436.2017.1320648.
[52] P.J. Kelly, R.D. Arnell, Magnetron sputtering: a review of recent developments and applications, Vacuum. 56 (2000) 159–172. https://doi.org/10.1016/S0042-207X(99)00189-X.
[53] M.A. Haque, M.T.A. Saif, A review of MEMS-based microscale and nanoscale tensile and bending testing, (2003) 8.

[54] D.N. Allsopp, I.M. Hutchings, Micro-scale abrasion and scratch response of PVD coatings at elevated temperatures, Wear. 251 (2001) 1308–1314. https://doi.org/10.1016/S0043-1648(01)00755-4.
[55] S.J. Bull, Failure modes in scratch adhesion testing, Surface and Coatings Technology. 50 (1991) 25–32. https://doi.org/10.1016/0257-8972(91)90188-3.
[56] H.T. Tran, H. Mraied, S. Izadi, A.A. Volinsky, W. Cai, Optimizing ductility and fracture of amorphous metal thin films on polyimide using multilayers, Int J Fract. 204 (2017) 129–142. https://doi.org/10.1007/s10704-016-0166-y.
[57] R.M. Niu, G. Liu, C. Wang, G. Zhang, X.D. Ding, J. Sun, Thickness dependent critical strain in submicron Cu films adherent to polymer substrate, Appl. Phys. Lett. 90 (2007) 161907. https://doi.org/10.1063/1.2722684.
[58] W. c. Oliver, G. m. Pharr, An improved technique for determining hardness and elastic modulus using load and displacement sensing indentation experiments, Journal of Materials Research. 7 (1992) 1564–1583. https://doi.org/10.1557/JMR.1992.1564.
[59] J.R. Cahoon, W.H. Broughton, A.R. Kutzak, The determination of yield strength from hardness measurements, Metallurgical Transactions. 2 (1971) 1979–1983. https://doi.org/10.1007/BF02913433.
[60] T.Y. Tsui, J. Vlassak, W.D. Nix, Indentation plastic displacement field: Part II. The case of hard films on soft substrates, Journal of Materials Research. 14 (1999) 2204–2209. https://doi.org/10.1557/JMR.1999.0296.
[61] G.E. Dieter, D.J. Bacon, Mechanical metallurgy, McGraw-hill New York, 1976.
[62] W.D. Callister, Materials science and engineering : an introduction, J. Wiley, New York, 2003.
[63] S. Zhang, D. Sun, Y. Fu, H. Du, Toughness measurement of thin films: a critical review, Surface and Coatings Technology. 198 (2005) 74–84. https://doi.org/10.1016/j.surfcoat.2004.10.021.
[64] A.A. Volinsky, N.R. Moody, W.W. Gerberich, Interfacial toughness measurements for thin films on substrates, Acta Materialia. 50 (2002) 441–466. https://doi.org/10.1016/S1359-6454(01)00354-8.
[65] J. Chen, S.J. Bull, Approaches to investigate delamination and interfacial toughness in coated systems: an overview, Journal of Physics D: Applied Physics. 44 (2010) 034001. https://doi.org/10.1088/0022-3727/44/3/034001.
[66] R.F. Cook, M.R. Pascucci, W.H. Rhodes, Lateral Cracks and Microstructural Effects in the Indentation Fracture of Yttria, Journal of the American Ceramic Society. 73 (1990) 1873–1878. https://doi.org/10.1111/j.1151-2916.1990.tb05238.x.
[67] G.R. ANSTIS, P. CHANTIKUL, B.R. LAWN, D.B. MARSHALL, A Critical Evaluation of Indentation Techniques for Measuring Fracture Toughness: I, Direct Crack Measurements, Journal of the American Ceramic Society. 64 (1981) 533–538. https://doi.org/10.1111/j.1151-2916.1981.tb10320.x.

[68] J. Chen, Indentation-based methods to assess fracture toughness for thin coatings, J. Phys. D: Appl. Phys. 45 (2012) 203001. https://doi.org/10.1088/0022-3727/45/20/203001.
[69] R.F. Cook, G.M. Pharr, Direct Observation and Analysis of Indentation Cracking in Glasses and Ceramics, Journal of the American Ceramic Society. 73 (1990) 787–817. https://doi.org/10.1111/j.1151-2916.1990.tb05119.x.
[70] K. Fu, L. Chang, B. Zheng, Y. Tang, Y. Yin, Analysis on cracking in hard thin films on a soft substrate under Berkovich indentation, Vacuum. 112 (2015) 29–32. https://doi.org/10.1016/j.vacuum.2014.11.013.
[71] A. Karimi, Y. Wang, T. Cselle, M. Morstein, Fracture mechanisms in nanoscale layered hard thin films, Thin Solid Films. 420–421 (2002) 275–280. https://doi.org/10.1016/S0040-6090(02)00944-6.
[72] B.C. Mohanty, H.R. Choi, Y.M. Choi, Y.S. Cho, Thickness-dependent fracture behaviour of flexible ZnO : Al thin films, J. Phys. D: Appl. Phys. 44 (2011) 025401. https://doi.org/10.1088/0022-3727/44/2/025401.
[73] K. Zeng, D. Rowcliffe, Experimental Measurement of Residual Stress Field around Sharp Indentation in Glass, J American Ceramic Society. 77 (1994) 524–530. https://doi.org/10.1111/j.1151-2916.1994.tb07025.x.
[74] T.-Y. Zhang, L.-Q. Chen, R. Fu, Measurements of residual stresses in thin films deposited on silicon wafers by indentation fracture, Acta Materialia. 47 (1999) 3869–3878. https://doi.org/10.1016/S1359-6454(99)00248-7.
[75] A. Tiwari, ed., Nanomechanical Analysis of High Performance Materials, Springer Netherlands, Dordrecht, 2014. https://doi.org/10.1007/978-94-007-6919-9.
[76] J. Chen, S.J. Bull, Indentation fracture and toughness assessment for thin optical coatings on glass, J. Phys. D: Appl. Phys. 40 (2007) 5401–5417. https://doi.org/10.1088/0022-3727/40/18/S01.
[77] Y. Xiang, T. Li, Z. Suo, J.J. Vlassak, High ductility of a metal film adherent on a polymer substrate, Appl. Phys. Lett. 87 (2005) 161910. https://doi.org/10.1063/1.2108110.
[78] J.L. Bputh, Cracking of Thin Bonded Films in Residual Tension 19.
[79] B. Ingham, M.F. Toney, 1 - X-ray diffraction for characterizing metallic films, in: K. Barmak, K. Coffey (Eds.), Metallic Films for Electronic, Optical and Magnetic Applications, Woodhead Publishing, 2014: pp. 3–38. https://doi.org/10.1533/9780857096296.1.3.
[80] J.I. Langford, A.J.C. Wilson, Scherrer after sixty years: A survey and some new results in the determination of crystallite size, Journal of Applied Crystallography. 11 (1978) 102–113. https://doi.org/10.1107/S0021889878012844.
[81] K.C.A. Smith, C.W. Oatley, The scanning electron microscope and its fields of application, British Journal of Applied Physics. 6 (1955) 391–399. https://doi.org/10.1088/0508-3443/6/11/304.
[82] B.J. Inkson, 2 - Scanning electron microscopy (SEM) and transmission electron microscopy (TEM) for materials characterization, in: G. Hübschen, I. Altpeter, R. Tschuncky, H.-G. Herrmann (Eds.), Materials Characterization

Using Nondestructive Evaluation (NDE) Methods, Woodhead Publishing, 2016: pp. 17–43. https://doi.org/10.1016/B978-0-08-100040-3.00002-X.
[83] C.A. Volkert, A.M. Minor, Focused Ion Beam Microscopy and Micromachining, MRS Bulletin. 32 (2007) 389–399. https://doi.org/10.1557/mrs2007.62.
[84] X. Li, B. Bhushan, A review of nanoindentation continuous stiffness measurement technique and its applications, Materials Characterization. 48 (2002) 11–36. https://doi.org/10.1016/S1044-5803(02)00192-4.
[85] B.R. LAWN, A.G. EVANS, D.B. MARSHALL, Elastic/Plastic Indentation Damage in Ceramics: The Median/Radial Crack System, Journal of the American Ceramic Society. 63 (1980) 574–581. https://doi.org/10.1111/j.1151-2916.1980.tb10768.x.
[86] J. Chen, S.J. Bull, Assessment of the toughness of thin coatings using nanoindentation under displacement control, Thin Solid Films. 494 (2006) 1–7. https://doi.org/10.1016/j.tsf.2005.08.176.
[87] Y.-T. Cheng, Z. Li, C.-M. Cheng, Scaling relationships for indentation measurements, Philosophical Magazine A. 82 (2002) 1821–1829. https://doi.org/10.1080/01418610208235693.
[88] K. Liu, M. Ostadhassan, B. Bubach, Applications of nano-indentation methods to estimate nanoscale mechanical properties of shale reservoir rocks, Journal of Natural Gas Science and Engineering. 35 (2016) 1310–1319. https://doi.org/10.1016/j.jngse.2016.09.068.
[89] Y. Li, Fracture Toughness Assesment of shales by Nanoindentation, (2015). https://doi.org/10.7275/JZYM-1G18.
[90] W.C. Oliver, G.M. Pharr, Measurement of hardness and elastic modulus by instrumented indentation: Advances in understanding and refinements to methodology, J. Mater. Res. 19 (2004) 3–20. https://doi.org/10.1557/jmr.2004.19.1.3.
[91] L.B. Freund, S. Suresh, Thin film materials : stress, defect formation, and surface evolution, (2003). http://public.eblib.com/choice/publicfullrecord.aspx?p=255181.
[92] Z.T. Wang, K.Y. Zeng, Y. Li, The correlation between glass formation and hardness of the amorphous phase, Scripta Materialia. 65 (2011) 747–750. https://doi.org/10.1016/j.scriptamat.2011.06.043.
[93] M. Abboud, S. Özerinç, Size-independent strength of amorphous–HCP crystalline metallic nanolayers, Journal of Materials Research. 34 (2019) 2275–2284. https://doi.org/10.1557/jmr.2019.74.
[94] M. Ghidelli, S. Gravier, J.-J. Blandin, P. Djemia, F. Mompiou, G. Abadias, J.-P. Raskin, T. Pardoen, Extrinsic mechanical size effects in thin ZrNi metallic glass films, Acta Materialia. 90 (2015) 232–241. https://doi.org/10.1016/j.actamat.2015.02.038.
[95] M. Abboud, A. Motallebzadeh, Ö. Duygulu, R. Maaß, S. Özerinç, Microstructure and nanomechanical behavior of sputtered CuNb thin films, Intermetallics. 136 (2021) 107249. https://doi.org/10.1016/j.intermet.2021.107249.

[96] R.L. Zong, S.P. Wen, F. Zeng, Y. Gao, F. Pan, Nanoindentation studies of Cu–W alloy films prepared by magnetron sputtering, Journal of Alloys and Compounds. 464 (2008) 544–549. https://doi.org/10.1016/j.jallcom.2007.10.033.
[97] W. Qin, L. Fu, T. Xie, J. Zhu, W. Yang, D. Li, L. Zhou, Abnormal hardness behavior of Cu-Ta films prepared by magnetron sputtering, Journal of Alloys and Compounds. 708 (2017) 1033–1037. https://doi.org/10.1016/j.jallcom.2017.03.106.
[98] A. Rauf, Y. Fang, H. Zhang, G. Peng, T. Feng, Thickness effects on microstructure, mechanical and soft magnetic properties of sputtered Fe Zr thin film metallic glass, Journal of Non-Crystalline Solids. 521 (2019) 119500. https://doi.org/10.1016/j.jnoncrysol.2019.119500.
[99] H. Yan, R.N. Santoso, Y. Jiang, M.H. Liang, Z. Chen, Effect of oxygen concentration on the thermal stability of magnetron sputtered amorphous Ta–Ni thin films, Thin Solid Films. 520 (2012) 2356–2361. https://doi.org/10.1016/j.tsf.2011.11.002.
[100] G. Abadias, J.J. Colin, D. Tingaud, Ph. Djemia, L. Belliard, C. Tromas, Elastic properties of α- and β-tantalum thin films, Thin Solid Films. 688 (2019) 137403. https://doi.org/10.1016/j.tsf.2019.06.053.
[101] S. Korkmaz, İ.A. Kariper, Glass formation, production and superior properties of Zr-based thin film metallic glasses (TFMGs): A status review, Journal of Non-Crystalline Solids. 527 (2020) 119753. https://doi.org/10.1016/j.jnoncrysol.2019.119753.
[102] H.-H. Huang, Y.-S. Sun, C.-P. Wu, C.-F. Liu, P.K. Liaw, W. Kai, Corrosion resistance and biocompatibility of Ni-free Zr-based bulk metallic glass for biomedical applications, Intermetallics. 30 (2012) 139–143. https://doi.org/10.1016/j.intermet.2012.03.015.
[103] Y.L. Zhou, M. Niinomi, T. Akahori, H. Fukui, H. Toda, Corrosion resistance and biocompatibility of Ti–Ta alloys for biomedical applications, Materials Science and Engineering: A. 398 (2005) 28–36. https://doi.org/10.1016/j.msea.2005.03.032.
[104] R. Saha, J.A. Barnard, Effect of structure on the mechanical properties of Ta and Ta(N) thin films prepared by reactive DC magnetron sputtering, Journal of Crystal Growth. 174 (1997) 495–500. https://doi.org/10.1016/S0022-0248(96)01148-7.
[105] M. Zhang, Y.F. Zhang, P.D. Rack, M.K. Miller, T.G. Nieh, Nanocrystalline tetragonal tantalum thin films, Scripta Materialia. 57 (2007) 1032–1035. https://doi.org/10.1016/j.scriptamat.2007.07.041.
[106] L.Y. Chen, Z.D. Fu, G.Q. Zhang, X.P. Hao, Q.K. Jiang, X.D. Wang, Q.P. Cao, H. Franz, Y.G. Liu, H.S. Xie, S.L. Zhang, B.Y. Wang, Y.W. Zeng, J.Z. Jiang, New Class of Plastic Bulk Metallic Glass, Phys. Rev. Lett. 100 (2008) 075501. https://doi.org/10.1103/PhysRevLett.100.075501.
[107] Q. He, Y.-Q. Cheng, E. Ma, J. Xu, Locating bulk metallic glasses with high fracture toughness: Chemical effects and composition optimization, Acta Materialia. 59 (2011) 202–215. https://doi.org/10.1016/j.actamat.2010.09.025.

[108] J. Schroers, W.L. Johnson, Ductile Bulk Metallic Glass, Phys. Rev. Lett. 93 (2004) 255506. https://doi.org/10.1103/PhysRevLett.93.255506.
[109] Y.Q. Cheng, A.J. Cao, E. Ma, Correlation between the elastic modulus and the intrinsic plastic behavior of metallic glasses: The roles of atomic configuration and alloy composition, Acta Materialia. 57 (2009) 3253–3267. https://doi.org/10.1016/j.actamat.2009.03.027.
[110] L. Zhang, Y.-Q. Cheng, A.-J. Cao, J. Xu, E. Ma, Bulk metallic glasses with large plasticity: Composition design from the structural perspective, Acta Materialia. 57 (2009) 1154–1164. https://doi.org/10.1016/j.actamat.2008.11.002.
[111] M. Jafary-Zadeh, R. Tavakoli, J.J. Koh, Z.H. Aitken, Y.-W. Zhang, Effect of chemical composition and affinity on the short- and medium-range order structures and mechanical properties of Zr-Ni-Al metallic glass, Journal of Non-Crystalline Solids. 456 (2017) 68–75. https://doi.org/10.1016/j.jnoncrysol.2016.10.042.
[112] H. Skliarova, O. Azzolini, R.R. Johnson, V. Palmieri, Co-sputtered amorphous Nb–Ta, Nb–Zr and Ta–Zr coatings for corrosion protection of cyclotron targets for [18F] production, Journal of Alloys and Compounds. 639 (2015) 488–495. https://doi.org/10.1016/j.jallcom.2015.03.181.
[113] D.R. Economy, M.J. Cordill, E.A. Payzant, M.S. Kennedy, Residual stress within nanoscale metallic multilayer systems during thermal cycling, Materials Science and Engineering: A. 648 (2015) 289–298. https://doi.org/10.1016/j.msea.2015.09.082.
[114] S. Shiri, C. Zhang, A. Odeshi, Q. Yang, Growth and characterization of tantalum multilayer thin films on CoCrMo alloy for orthopedic implant applications, Thin Solid Films. 645 (2018) 405–408. https://doi.org/10.1016/j.tsf.2017.11.017.
[115] H.S. Chou, J.C. Huang, L.W. Chang, Mechanical properties of ZrCuTi thin film metallic glass with high content of immiscible tantalum, Surface and Coatings Technology. 205 (2010) 587–590. https://doi.org/10.1016/j.surfcoat.2010.07.042.
[116] C. Yuan, R. Fu, F. Zhang, X. Zhang, F. Liu, Microstructure evolution and mechanical properties of nanocrystalline zirconium processed by surface circulation rolling treatment, Materials Science and Engineering: A. 565 (2013) 27–32. https://doi.org/10.1016/j.msea.2012.11.092.
[117] K. Benouareth, Study of the interaction between a zirconium thin film and an EN C100 steel substrate: Temperature effect, (2016) 6.
[118] I. Souli, G.C. Gruber, V.L. Terziyska, J. Zechner, C. Mitterer, Thermal stability of immiscible sputter-deposited Cu-Mo thin films, Journal of Alloys and Compounds. 783 (2019) 208–218. https://doi.org/10.1016/j.jallcom.2018.12.250.
[119] S. Achache, F. Sanchette, Effect of Tantalum Addition on Properties of Cu–Zr–Based Thin Film Metallic Glasses (TFMGs), Coatings. 10 (2020) 515. https://doi.org/10.3390/coatings10060515.

[120] A.C. Fischer-Cripps, Nanoindentation, 2nd ed., Springer-Verlag, New York, 2004. //www.springer.com/la/book/9780387220451 (accessed August 31, 2018).
[121] D. Tabor, The Hardness of Metals, OUP Oxford, 2000.
[122] A. Misra, J.P. Hirth, R.G. Hoagland, Length-scale-dependent deformation mechanisms in incoherent metallic multilayered composites, Acta Materialia. 53 (2005) 4817–4824.
[123] B.E. Schuster, Q. Wei, T.C. Hufnagel, K.T. Ramesh, Size-independent strength and deformation mode in compression of a Pd-based metallic glass, Acta Materialia. 56 (2008) 5091–5100. https://doi.org/10.1016/j.actamat.2008.06.028.
[124] S.Y. Kuan, H.S. Chou, M.C. Liu, X.H. Du, J.C. Huang, Micromechanical response for the amorphous/amorphous nanolaminates, Intermetallics. 18 (2010) 2453–2457. https://doi.org/10.1016/j.intermet.2010.09.001.
[125] Z.C. Cordero, B.E. Knight, C.A. Schuh, Six decades of the Hall–Petch effect – a survey of grain-size strengthening studies on pure metals, International Materials Reviews. 61 (2016) 495–512. https://doi.org/10.1080/09506608.2016.1191808.
[126] Zhang et al. - 2005 - Toughness measurement of thin films a critical re.pdf, (n.d.).
[127] M.R. Taha, E. Soliman, M. Sheyka, A. Reinhardt, M. Al-Haik, Fracture toughness of hydrated cement paste using nanoindentation, (2010) 8.
[128] X.K. Xi, D.Q. Zhao, M.X. Pan, W.H. Wang, Y. Wu, J.J. Lewandowski, Fracture of Brittle Metallic Glasses: Brittleness or Plasticity, Phys. Rev. Lett. 94 (2005) 125510. https://doi.org/10.1103/PhysRevLett.94.125510.
[129] R.O. Ritchie, The conflicts between strength and toughness, Nature Materials. 10 (2011) 817–822. https://doi.org/10.1038/nmat3115.
[130] D.C. Hofmann, J.-Y. Suh, A. Wiest, G. Duan, M.-L. Lind, M.D. Demetriou, W.L. Johnson, Designing metallic glass matrix composites with high toughness and tensile ductility, Nature. 451 (2008) 1085–1089. https://doi.org/10.1038/nature06598.
[131] Y.H. Liu, D. Wang, K. Nakajima, W. Zhang, A. Hirata, T. Nishi, A. Inoue, M.W. Chen, Characterization of Nanoscale Mechanical Heterogeneity in a Metallic Glass by Dynamic Force Microscopy, Phys. Rev. Lett. 106 (2011) 125504. https://doi.org/10.1103/PhysRevLett.106.125504.
[132] Y. Wang, M. Li, J. Xu, Toughen and harden metallic glass through designing statistical heterogeneity, Scripta Materialia. 113 (2016) 10–13. https://doi.org/10.1016/j.scriptamat.2015.09.038.
[133] K. Kosiba, D. Şopu, S. Scudino, L. Zhang, J. Bednarcik, S. Pauly, Modulating heterogeneity and plasticity in bulk metallic glasses: Role of interfaces on shear banding, International Journal of Plasticity. 119 (2019) 156–170. https://doi.org/10.1016/j.ijplas.2019.03.007.
[134] Y. Dong, S. Liu, J. Biskupek, Q. Cao, X. Wang, J.-Z. Jiang, R. Wunderlich, H.-J. Fecht, Improved Tensile Ductility by Severe Plastic Deformation for

Nano-Structured Metallic Glass, Materials. 12 (2019) 1611. https://doi.org/10.3390/ma12101611.
[135] H.Y. Song, P. Yin, M.R. An, Y.L. Li, Design strategy for high plasticity and strength in metallic glasses: A molecular dynamics simulation study, Physica E: Low-Dimensional Systems and Nanostructures. 108 (2019) 27–33. https://doi.org/10.1016/j.physe.2018.12.010.
[136] N.A. Mara, D. Bhattacharyya, P.O. Dickerson, R.G. Hoagland, A. Misra, Ultrahigh Strength and Ductility of Cu-Nb Nanolayered Composites, MSF. 633–634 (2009) 647–653. https://doi.org/10.4028/www.scientific.net/MSF.633-634.647.
[137] Y.Q. Wang, J.Y. Zhang, X.Q. Liang, K. Wu, G. Liu, J. Sun, Size- and constituent-dependent deformation mechanisms and strain rate sensitivity in nanolaminated crystalline Cu/amorphous Cu–Zr films, Acta Materialia. 95 (2015) 132–144. https://doi.org/10.1016/j.actamat.2015.05.007.
[138] A.L. Greer, A. Castellero, S.V. Madge, I.T. Walker, J.R. Wilde, Nanoindentation studies of shear banding in fully amorphous and partially devitrified metallic alloys, Materials Science and Engineering: A. 375–377 (2004) 1182–1185. https://doi.org/10.1016/j.msea.2003.10.032.
[139] T.C. Hufnagel, C.A. Schuh, M.L. Falk, Deformation of metallic glasses: Recent developments in theory, simulations, and experiments, Acta Materialia. 109 (2016) 375–393. https://doi.org/10.1016/j.actamat.2016.01.049.
[140] F.T.N. Vüllers, R. Spolenak, From solid solutions to fully phase separated interpenetrating networks in sputter deposited “immiscible” W–Cu thin films, Acta Materialia. 99 (2015) 213–227. https://doi.org/10.1016/j.actamat.2015.07.050.
[141] A. Bachmaier, M. Pfaff, M. Stolpe, H. Aboulfadl, C. Motz, Phase separation of a supersaturated nanocrystalline Cu–Co alloy and its influence on thermal stability, Acta Materialia. 96 (2015) 269–283. https://doi.org/10.1016/j.actamat.2015.05.053.
[142] K.A. Darling, M.A. Tschopp, R.K. Guduru, W.H. Yin, Q. Wei, L.J. Kecskes, Microstructure and mechanical properties of bulk nanostructured Cu–Ta alloys consolidated by equal channel angular extrusion, Acta Materialia. 76 (2014) 168–185. https://doi.org/10.1016/j.actamat.2014.04.074.
[143] E. Ma, Alloys created between immiscible elements, Progress in Materials Science. 50 (2005) 413–509. https://doi.org/10.1016/j.pmatsci.2004.07.001.
[144] F. Zeng, M. Ding, B. Zhao, F. Pan, Amorphous alloy film formed in an immiscible Cu–Ta system by ion beam assisted deposition, Materials Letters. 53 (2002) 40–43. https://doi.org/10.1016/S0167-577X(01)00450-5.
[145] U. Mizutani, C.H. Lee, Mechanical Alloying in Cu–V and Cu–Ta Systems Characterized by Positive Heat of Mixing (Overview), Materials Transactions, JIM. 36 (1995) 210–217. https://doi.org/10.2320/matertrans1989.36.210.

[146] F. Zeng, Y. Gao, L. Li, D.M. Li, F. Pan, Elastic modulus and hardness of Cu–Ta amorphous films, Journal of Alloys and Compounds. 389 (2005) 75–79. https://doi.org/10.1016/j.jallcom.2004.06.077.